GRADUATE SCHOOL OF URBAN INNOVATION

YOKOHAMA NATIONAL UNIVERSITY

Unstructured mesh tsunami simulation using FVCOM considering the fine structure of land use

by

Retno Utami Agung Wiyono

A dissertation submitted in partial fulfillment of the requirements for the Doctoral Degree of Engineering

Academic Advisor:

Assoc. Prof. Takayuki Suzuki

Prof. Jun Sasaki

March, 2015

ABSTRACT

Tsunami hazard maps have essential roles in effective evacuation as part of a tsunami early warning system. In order to simulate tsunami inundation, it is necessary to perform inundation modeling with acceptable results, yet efficient computational costs.

Among existing methods for inundation modeling are: (1) resolving inundation mesh system method; (2) uniform bottom friction; (3) spatial variation of bottom friction; and (4) spatial variation of bottom friction considering the fine structure of land use. Method 1 is accurate to model buildings, but computational cost is high while method 2 and 3 have lower computational costs but constructed area may not be modeled well. Method 4 had been applied to for structured grid model only.

In this study, new approach of spatial variation of bottom friction considering the fine structure of land use in unstructured grid model is proposed by resolving concrete buildings but not resolving wooden houses at inundation area. While wooden houses heights are not included, roughness parameters of wooden houses are included to model friction function. The proposed method is adopted to tsunami simulation system using FVCOM.

The proposed tsunami simulation system is validated to analytical case of wave model under simplified beach model. The analytical solutions are well reproduced by FVCOM simulation. The tsunami simulation system is also validated to the physical experiment results of influence of macro-roughness on tsunami run up. The inundation depth of experimental results are well reproduced by FVCOM.

Using the experimental case of tsunami inundation modeling in constructed environments, the proposed tsunami simulation is validated and sensitivity tests in term of grid size and friction factors are performed. General trends of inundation depth and cross shore velocity are reproduced well by numerical simulations. It is found that optimum grid size for simulation using the proposed simulation system is two times of the wooden houses size which is 0.3 m. Simulation using the proposed simulation system is 61.5% faster than the simulation by resolving all buildings with 0.15 m grid size.

The simulation system has also been applied to the 2011 Tohoku Tsunami case to elucidate the mechanism of the 2011 Tohoku Tsunami properties in ports in Tokyo Bay including the mechanism responsible for the unexpectedly high amplification of the tsunami that was observed in some ports. The effectiveness of floodgates in preventing inundation was shown. The importance of bathymetry data resolution can be clarified from the

simulations.

The simulation system is applied to simulate tsunamis in Kamakura, Kanagawa, Japan. A concept of an integrated minimum time was introduced and was applied to coastal area of Kamakura. Maps for the integrated minimum time were created supposing the threshold value of the inundation depth to be 0.5 m and considering seven expected earthquake and tsunamis (Meiou, Keichou, Genroku Kanto, Kannawa-Kouzu Matsuda, Minami Kanto, Kanagawa-ken Seibu, and Bousou Peninsula). The effectiveness of countermeasures to maximize expected minimum evacuation time, including the implementation of elevated road, water gate in a river mouth, and elevated river wall are considered. Among these countermeasures, the elevated road case is found to be the most effective for maximizing the expected minimum evacuation time and reducing the inundation area as well as lowering the maximum velocities due to its large magnitude of the scale.

The simulation system is also applied to simulate Keicho Tsunami in Yokohama. Three simulations are compared: resolved mesh case with original (FVCOM) friction function, unresolved mesh case with original (FVCOM) friction function, and unresolved mesh case with modified friction function. Maximum inundation depth area compared among three simulations. Resolved mesh case shows the smallest area of maximum inundation depth because buildings are resolved. Unresolved mesh case with modified bottom friction shows larger area of maximum inundation depth because buildings are not resolved and modified friction function is used. Unresolved mesh case with original bottom friction shows the largest area of maximum inundation depth because buildings are not resolved and original friction function is used.

ACKNOWLEDGEMENTS

All praise is due to almighty Allah, the one and only Lord of earth and heavens, who gave me strength and ability to accomplish this work.

I would like to thank my academic advisor Professor Jun Sasaki for his encouragements, guidance, and discussions during my study period in Yokohama National University (YNU) and The University of Tokyo (UTokyo). After Professor Jun Sasaki moved to UTokyo, Associate Professor Takayuki Suzuki became my academic supervisor. I would like to express my gratitude for his kind support, help, and suggestions to improve my work. I would like to acknowledge Professor Yoshiyuki Nakamura for his kind suggestions especially in lab seminars. I would also take this opportunity to acknowledge the remaining committee members of the examination, Professor Tatsuya Tsubaki, Professor Hiroshi Katsuchi, and Associate Professor Kimitoshi Hayano for their valuable suggestions.

It is also a pleasure to express my gratitude to Professor Daniel Cox and Associate Professor Tomoaki Nakamura for their support in providing experimental laboratory and numerical simulation results. I would also gratefully acknowledge Dr. Abdul Muhari for the supports given in understanding on Equivalent Roughness Model.

It is a valuable experience to study three years in YNU and half year in UTokyo. Thus, I would like to convey my sincere thanks to our lab secretary Ms. Akiko Nakao and Ms. Eiko Murozono for their numerous supports. My special thanks to my lab mates in YNU especially Dr. Chamila Niroshinie and Ms. Mangala Amunugama who always give me help and motivation, Mr. Yamamoto Shuji for his help in coding, and other lab members who gave me enjoyable environment to study. I would like to also appreciate my lab mates in UTokyo who gave me a lot of motivation during my critical last six month.

I present my special thanks to my beloved husband, Mr. Abdur Rohman for his kind encouragement, endless support, help and motivation all the time; my lovely son for giving me smile always; our parents and family in Indonesia for their prayers.

I would like to acknowledge the Japanese Ministry of Education, Culture, Sports, Science, and Technology for granting me Monbukagakusho scholarship and Yokohama Kogyokai for providing me scholarship for the last year of my study period.

Moreover other than the mentioned above, there are many people who helped numerous ways and pray for me. All of them are highly appreciated.

TABLE OF CONTENTS

LIST OF FIGURES

LIST OF TABLES

LIST OF SYMBOLS

x, y, and *z*	East, north, and vertical axes in the Cartesian coordinate system
u, v, and *w*	*x, y,* and *z* velocity components
ρ	Density
P_a	Air pressure at the sea surface
P_H	Hydrostatic pressure
q	*N*on-hydrostatic pressure
f	Coriolis parameter
g	*G*ravitational acceleration
T	Temperature
S	*S*alinity
K_m	*V*ertical eddy viscosity coefficient
K_h	Thermal vertical eddy diffusion coefficient
F_u, F_v, F_T, and F_S	Horizontal momentum, thermal, and salt diffusion terms
H	*B*ottom depth (relative to z=0)
ζ	Height of the free surface (relative to z=0)
$D = H + \zeta$	Total water column depth
$p = p_a + p_H + q$	Total pressure
τ_{sx}, τ_{sy}	*x* and *y* components of surface wind
Q_b	Groundwater volume flux at the bottom
Ω	Area of the groundwater source
τ_{bx}, τ_{by}	*x* and *y* components of bottom stresses
C	Roughness coefficient
Δ_{t_E}	Time step of the external mode
ΔL	Computational length scale
U	Magnitude of the horizontal velocity
Δ_{t_I}	Time step of the internal mode
C_I	Maximum phase speed of internal gravity waves

1. INTRODUCTION

1.1 Background

In the last ten years, two huge tsunamis occurred causing a high number of casualties . The 2004 Indian Ocean Tsunami, was followed by the 2011 Tohoku Earthquake Tsunami, which caused by a 9.0 magnitude earthquake. The 2011 Tohoku Earthquake tsunami occurred at 14:46 JST on March 11. Although Japan has prepared much to protect each part of the country, the damage still occurred in many places especially the places near the epicenter area. In the northern part of Tohoku which is known as Sanriku region, the tsunami inundated over 400 km^2 of land (Mori et al., 2012). Realizing the urgency of making further preparedness to overcome tsunami, a deeper understanding of tsunamis is indispensable.

In order to estimate the inundation area, it is necessary to conduct tsunami simulation to understand how the tsunami behavior around the focusing area. Between numerical and physical simulations, numerical simulations are more economic compared to physical simulations and in term of the required working space and facilities, operating cost and technical staff (Kamphius 2000).

There are various software packages that can be used to model tsunami. However, from economic point of view, free model is preferable. FVCOM (Chen et al., 2006) is one of the free hydrodynamics model that utilize unstructured grid model. FVCOM 2.6.1 is firstly applied for tsunami case by Sasaki et al., 2011.

Unstructured grid models become popular as they are easier to be used in parallel computation and preferable for tsunami simulation since the spatial scale of inundation area is much smaller than that of the major tsunami propagation area. Moreover, unstructured grid simulations are efficient because several time nesting simulations are not necessary to be conducted. In order to take the advantages of using unstructured grid simulation, FVCOM is utilized as a tool for a present study.

To conduct an efficient tsunami inundation modeling, it is necessary to model the inundation area using a proper method. Inundation simulation using a very fine grid and resolving all buildings in inundation area will create accurate results yet causing high cost of computational time. A method to avoid resolving all buildings in inundation area is by utilizing bottom roughness coefficient as a representative of buildings. This study aims to

propose a new method to combine the first method to resolve concrete buildings in inundation area and to substitute wooden houses with bottom roughness coefficient in inundation modeling.

As different friction terms will cause different simulated tsunami heights (MacInnes et al., 2013), it is necessary to estimate appropriate bottom roughness coefficients in inundation area. Equivalent Roughness Model (ERM) is a method to use spatial variation of bottom roughness coefficient that are function of land use and of the percentage of building occupancy on each grid cell (Muhari et al., 2011). This method was initiated by Goto & Shuto (1983) who include effects of solid buildings or reflections from sea walls in tsunami inundation numerical computations. Kotani et al. (1998) proposed global approach to include the effects of building density at specific areas to numerical simulations based on land use. Local approach to compute effects of houses in numerical computation was proposed by Aburaya and Imamura (2002). Muhari et al. (2011) further examined the method in small grid size. Finally Imai et al. (2013) considered a new approach of roughness coefficient calculation based on building condition in densely populated region for small grid bottom friction. They applied the method to the structured mesh simulation.

Up to now, unstructured grid tsunami models adopt several methods of modeling bottom roughness coefficient. TELEMAC-2D, DELFIN, UNTRIM, and Fluidity/ICOM are capable to model uniform roughness coefficient, while DELFT3D-Flow, ADCIRC, MIKE21 Flow, SLIM, H2OCEAN, FVCOM, SELFE, TsunAWI are capable to model spatial variation of bottom roughness. In addition, DELFT3D-Flow has ability to calculate bottom roughness based on point classes, line classes, area classes and special classes including vegetation and hedges.

However there are no unstructured tsunami models consider bottom roughness coefficient based on building condition in densely populated region. This study aims to propose a new method to consider spatial variation of bottom roughness coefficient variation that are function of land use and of the percentage of building occupancy on each grid cell in constructed environment.

1.2 Objectives

Objective of this study is firstly to compare two methods in resolving inundation area on tsunami numerical simulations: resolving constructed area and not resolving constructed

area with modification of friction factor. Further, objective of the present study is to combine above methods in resolving inundation area on tsunami numerical simulations.

Finally, this study aims to propose tsunami simulation system using FVCOM considering the fine structure of land use. Spatial variation of bottom roughness coefficient that are function of land use and of the percentage of building occupancy on each grid cell in constructed environment is considered. The enhanced unstructured mesh tsunami model consists of the main code, additional bottom friction code, pre-processing and post-processing tools.

Furthermore, this study aims to firstly verify FVCOM on an analytical case, physical experimental case: "influence of macro-roughness on tsunami run up" and later to verify the proposed model to a physical experimental case: "tsunami inundation modeling in constructed environments".

Applications of FVCOM to real cases are also conducted including numerical assessment of the 2011 Tohoku Tsunami in Tokyo Bay with the effectiveness of floodgates, analysis on the effects of the tsunami countermeasures focusing on the tsunami arrival time in Kamakura and Keicho Tsunami simulation in Yokohama. The simulation results are further discussed.

1.3 Organization of the dissertation

This dissertation is organized into seven chapters. The content of each chapter are given below:

Chapter 1 provides backgrounds of conducting this research and objectives of the present study.

Chapter 2 includes the review of the existing unstructured mesh tsunami simulation models along with the brief summary on the bottom roughness model that is available in each model.

Chapter 3 describes the numerical method which is utilized in this study including the adopted tools and modified tools.

Chapter 4 describes FVCOM validation to the analytical case and physical experimental cases: "influence of macro-roughness on tsunami run up" and "tsunami inundation modeling in constructed environments".

Chapter 5 includes FVCOM application to real cases, including numerical assessment of the the 2011 Tohoku Tsunami in Tokyo Bay with the effectiveness of floodgates, analysis on the

effects of the tsunami countermeasures focusing on the tsunami arrival time in Kamakura, and Keicho Tsunami simulation in Yokohama.

Chapter 6 summaries the conclusions and recommendations from the present study.

2. LITERATURE REVIEW

After 2004 Indian Ocean Tsunami and 2011 Tohoku Tsunami, the importance of analyzing tsunami becomes very clear. In order to develop appropriate countermeasures, numerical simulation is an easiest yet efficient way to understand the phenomena while physical experiment needs more effort and time to conduct the same simulation.

Currently there are so many tsunami simulation and models available. Tsunami models can be classified into two large categories: structured grid models and unstructured grid tsunami models. As propagation area of tsunami is very large, application of structured grid model requires nesting method to cover large simulation domain. Numerical simulations need to be executed several times to obtain accurate simulation results in one local area.

Unstructured grid tsunami simulations has a clear advantage: coastline modeling will be more accurately modeled by unstructured mesh than by structured one as visualized in Figure 1. In addition, application of triangular grid system will allow one mesh system to simulate tsunami in large domain including propagation area and inundation area.

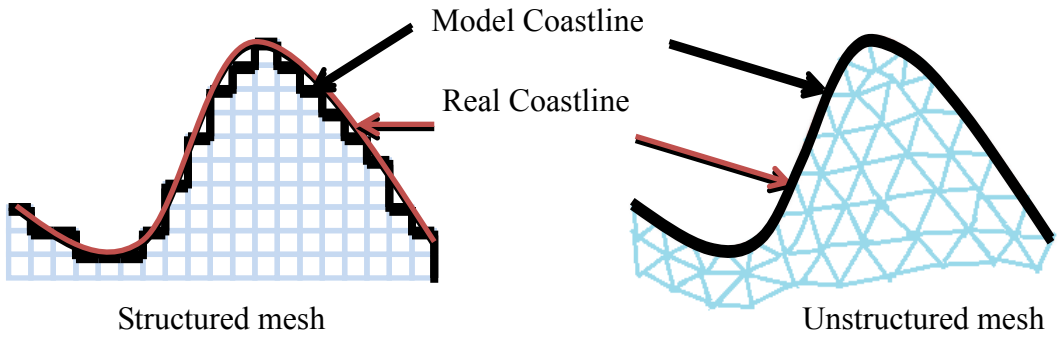

Figure 1 Comparison between structured and unstructured mesh

Currently there are many unstructured grid tsunami simulations. Unstructured grid tsunami models are summarized below.

1) DELFT3D-FLOW

DELFT3D-FLOW is an open source software 2D/3D that simulates fluid flow, waves, sediment transport, and morphology changes. DELFT3D-FLOW solves Navier Stokes equations for an incompressible fluid, under shallow water and Boussinesq assumptions

(Deltares 2014). Cartesian coordinates and Spherical coordinates are supported by DELFT-3D Flow. Bedform roughness predictors and vegetation models are able to be resolved in a 2D numerical model using the trachytope approach and in a 3D model by a combination of bed resistance formulations.

Trachytopes function allows one to specify the bed roughness and flow resistance on a sub-grid level by defining and using various land use or roughness/resistance classes. There are four classes as follow:

a. Area classes: These classes are basically the dominant roughness factor. The class is subdivided into three types: simple, alluvial and vegetation.
b. Line classes: These classes are applicable for linear trachytopes such as hedges or bridge piers.
c. Point classes: These classes are used to represent groups of individual trees or on a smaller scale plants.
d. Special classes: These classes can be implemented for flood protected area and composite trachytope class.

Delft3D-Flow has been compared with analytical results and laboratory observations from seven tsunami-like benchmark experiments and with field observations from the 26 December 2004 Indian Ocean Tsunami (Apotsos et al., 2011) and also applied to tsunami cases such as the 2011 Tohoku Tsunami (Sasaki et al., 2012).

2) ADCIRC (Advanced Three-Dimensional Circulation Model)

ADCIRC (Luettich et al., 1991) is a system of computer programs which solves the shallow-water equations in full nonlinear form. ADCIRC was developed by Department of the Army, US Army Corps of Engineers as a part of the Dredging Research Program to generate a database of harmonic constituents for tidal elevation and current around Gulf of Mexico coasts and to use global boundary conditions to compute storm surge hydrographs along the US coasts.

The program utilizes the finite element method with unstructured grid method. Typical ADCIRC applications have included tides modeling and wind driven circulation, analysis of hurricane storm surge and flooding, dredging feasibility and material disposal studies, transport studies, and near shore marine operations.

Roughness coefficient is computed using one of the following relationships: Darcy-Weisbach friction factor, Chezy friction coefficient, and Manning friction factor. The

nonlinear bottom friction coefficients are specified as spatially homogenous or non-homogeneous. If non-homogeneous case is chosen, the nonlinear bottom friction values are specified at each node.

ADCIRC was utilized to conduct numerical simulations of the 1993 Hokkaido Nansei-Oki tsunami and the 1964 Alaska tsunami (Myers and Baptista 2001) and also used for modeling tsunami inundation from a Cascadia subduction zone earthquake (Venturato, Arcas, and Kanoglu 2007).

3) MIKE21 Flow Model FM

MIKE 21 Flow Model FM (MIKE, 2011) was developed by Danish Hydraulic Institute (DHI) Water & Environment, Denmark as a module of MIKE 21, a professional engineering software package for the simulation of flows, waves, sediments and ecology in rivers, lakes, estuaries, bays, coastal areas and seas. The same names are used as the classic versions of MIKE21 and MIKE3 while an 'FM' is abbreviation of Flexible Mesh, allowing the model to calculate based on a finite volume method on an unstructured mesh.

Bed resistance can be specified in three different methods: no bed resistance, Chezy number, and Manning number. The format of the Chezy number and the Manning number can be constant (in domain) and varying in domain. MIKE21 FM was utilized to simulate the 2004 Indian Ocean Tsunami (Pedersen et al., 2005).

4) TELEMAC-2D

TELEMAC-2D is an unstructured grid 2D hydrodynamics freeware which solves the shallow water equations using the finite-element or finite-volume methods. The TELEMAC system was initially developed at the Laboratoire National d'Hydraulique, a department of research branch of Electricité de France (Hervouet 2000). However currently it is join efforts of several research groups in Europe. This software takes into account several phenomena such as propagation of long waves, bed friction, influence of Coriolis force and meteorological factors, turbulence, river flows, influence of horizontal temperature or salinity gradients on density, and Cartesian or spherical coordinates. This model together with other modules, SISYPHE (sediment transport and bed evolution model), DREDGESIM (dredging operations model in the river bed), MASCARET (1-dimensional free surface flow modeling), TOMAWAC (wave propagation model in coastal areas) and ARTEMIS

(numerical model of wave propagation towards the shore and agitation into harbors) are parts of the TELEMAC system.

Available roughness options are quadratic (Chezy, Strickel, Manning), Nikuradse or linear friction laws (EDF-DRD 2000). TELEMAC-2D was utilized to simulate the 1755 tsunami event for the UK and Irish coast (Wallingford et al., 2006) and tsunami propagation in the Sea of Marmara (Kilinc et al., 2009).

5) UNTRIM

UnTRIM (Casulli 1999) is an unstructured grid three-dimensional hydrodynamic model based on shallow water equations (Casulli and Walters 2000). The governing equations are discretized using a finite difference - finite volume algorithm, and the numerical method allows full wetting and drying of cells in the vertical and horizontal directions. UnTRIM model was utilized as a part of the Delta Risk Management Strategy (DRMS) project for hydrodynamic simulation in San Franciso Bay and the Sacramento-San Joaquin Delta.

UnTRIM model was utilized to model Sacramento-San Joaquin Delta using a single uniform roughness value over the entire domain (Macwilliams et al., 2008). However, they noted that if spatially-variable roughness can be justified for some areas, it can be used to improve model calibration. UnTRIM was also applied to simulate tsunami-wave in the North Sea (Lehfeldt et al., 2007).

6) SELFE (Semi-Implicit Eulerian-Lagrangian Finite Element)

SELFE, proposed by Zhang & Baptista (2008), is an unstructured grid, open-source, 3D baroclinic circulation modeling system. This model was designed for simulation across river-to-ocean scale, and it uses a semi-implicit finite-element Eulerian-Lagrangian algorithm to solve the Navier-Stokes equations.

SELFE was developed as an improvement model of ELCIRC. SELFE preserves the robustness and computational efficiency of ELCIRC, also eliminating grid orthogonally requirements and enabling flexibility in representing bathymetry and vertical structure of the water column (Zhang and Baptista 2008). SELFE incorporates wetting and drying of tidal flats, also has hydrostatic and non-hydrostatic options. Spatial variation of drag coefficient can be specified at every nodes of the simulation domain.

SELFE was utilized for Cascadia tsunami simulation (Priest et al., 2010). They simulated propagation and inundation utilizing post-earthquake topography. They utilized differences source geometry to understand the importance of accurate, geologically reasonable tsunami source characterization.

7) Fluidity/ICOM (The Imperial College Ocean Model)

Fluidity/ICOM (Ford et al., 2004) is an open source, multi-phase computational fluid dynamics codes developed by Applied Modeling and Computation Group (AMCG) at Imperial College, London. The code solves the Navier Stokes equation in one, two and three dimensions unstructured finite element meshes. It is also capable to be parallelized using MPI. In the Fluidity Manual, they discussed several simulation cases. For the case of tides in the Mediterranean Sea, the drag coefficient was set to 0.0025 (uniform) while frictional drag is based on a quadratic friction law.

This model was utilized for simulating 2004 Indian Ocean Tsunami (Mitchell et al., 2010). They estimated the drag coefficient using the logarithmic law of the wall. They also utilized the model to simulate the propagation of 1929 landslide generated 'Grand Banks Tsunami' across the North Atlantic.

8) TsunAWI

TsunAWI is simulation software developed by Tsunami Modeling Group of the Alfred Wegener Institute. TsunAWI was developed based on shallow water equation with unstructured mesh, finite element spatial discretization. This software is utilized for computations in the German-Indonesian Tsunami Early Warning System (GITEWS) and further for hazard assessment studies for local disaster management authorities in Indonesia (Behrens 2008). For most calculations, Manning bottom friction with a constant parameter is chosen. However, a value varying with the surface structure can also be calculated by TsunAWI.

Field benchmark was done with The Okushiri Tsunami 1993 as sample case and this software has been applied to Padang Tsunami (Wekerle et al., 2010), 2004 Indian Ocean Tsunami (Rakowsky et al., 2013), 2011 East Japan Tsunami (Behrens and LeVeque 2011) and also utilized to make inundation map in Bali (Behrens 2008).

9) VOLNA

VOLNA (Dutykh et al., 2011) is a tool for tsunami wave modeling which is able to handle generation, propagation and run-up of tsunami along the coast. The algorithm works on unstructured triangular meshes and the numerical treatment is able to compute wet/dry transition. There are no bottom friction modeling (and thus without any free parameter) utilized in tsunami modeling. VOLNA has been validated with analytical solutions and experimental data including tsunami in the Island of Okushiri, Japan (Dutykh et al., 2011) and to the 2011 Tohoku Tsunami (Dias et al., 2014).

10) SLIM (Second-generation Louvain-la-Neuve Ice-Ocean Model)

SLIM (de Brye et al., 2010) is an unstructured grid hydrodynamic model based on Finite Element Method (FEM) developed in Universite Catholique de Louvain (UCL) Louvain-la-Neuve, Belgium. SLIM consists of a 1D river model, a 2D depth averaged model and 3D barotropic/baroclinic model.

Spatial variation of Manning coefficient can be simulated by SLIM. SLIM was utilized to conduct numerical simulation in the Scheldt estuary and n=0.023 was chosen as the optimal value for the simulation (de Brye et al., 2010). Sassi et al. (2011) applied the same value for tidal case over distributaries channels in the Mahakam Delta. In the inner region, they varied the Manning coefficient from 0.017 to 0.029 and found that n=0.026 resulted in the best match with their measurements.

SLIM was also utilized for simulating 2011 East Japan Tsunami. The simulation showed how the wave develops as it propagates across the Pacific and interacts with the bathymetric features and islands.

11) DELFIN

DELFIN is a three dimensional unstructured grid hydrostatic finite volume/finite difference model developed by Ham (2006). DELFIN solves the shallow water equations, a well known simplification of the Navier-Stokes equations. The dimensionless drag coefficient may either be specified as a constant value (typically 0.0025 for a single layer, depth averaged simulation), or by using the logarithmic law of the wall.

DELFIN was applied to simulate tides in the North Sea. Although the modifications of the bottom friction parameters form the most important part of the tuning of the case, the option was still unavailable in DELFIN so they utilizes a single relatively low roughness

height of 1 cm for the entire domain. The model was also applied to 2004 Indian Ocean Tsunami (Ham 2006).

12) H2OCEAN

H2Ocean (Haiyang et al., 2010) is an unstructured grid, finite volume ocean model based on the 2-D shallow water equations. H2Ocean has been utilized to simulate the 2004 Indian Ocean Tsunami and the 2011 Tohoku Tsunami (Cui 2013). In the 2004 Indian Ocean Tsunami case, the Manning coefficient is set to 0.035, which is recommended in the study with TsunAWI (Harig et al., 2008) while in the 2011 Tohoku tsunami simulation, the Manning coefficient is set to 0.02 in the sea area and set to 0.05 in the land area.

13) FVCOM (Finite-Volume Community Ocean Model)

FVCOM (Chen et al., 2006) was developed by The University of Massachusetts-Dartmouth, Woods Hole Oceanographic Institution-WHOI joint efforts, which is an unstructured-grid, finite volume, 3-D primitive equation coastal ocean circulation model. The model consists of momentum, continuity, temperature, salinity and density equations. The horizontal grid comprises unstructured triangular cells and the irregular bottom is presented using generalized terrain-following coordinates.

Other than the constant value, the drag coefficient C_d may be calculated by either matching a logarithmic bottom layer to the model at a certain height above the bottom (the logarithmic law of the wall) or using GOTM formulation for bottom friction. In the latest version, a spatially varying bottom roughness field is applicable in FVCOM.

FVCOM has advantages for tsunami simulations as it has capability of wet and dry cell treatment and can run efficient parallel computing based on MPI. FVCOM was applied to the 2004 Indian Ocean Tsunami (Sasaki et al., 2011), the 1992 Flores Tsunami (Rojali et al., 2012), and the 2011 East Japan Tsunami (Chen et al., 2011, Wiyono et al., 2013, Chen et al., 2014).

Among the reviewed unstructured tsunami simulation model, VOLNA does not model bottom friction, TELEMAC-2D, DELFIN, UNTRIM, and Fluidity/ICOM are capable to model uniform roughness coefficient, while DELFT3D-Flow, ADCIRC, MIKE21 Flow, SLIM, H2OCEAN, FVCOM, SELFE, TsunAWI are capable to model spatial variation of bottom roughness. In addition, DELFT3D-Flow has ability to calculate bottom roughness

based on point classes, line classes, area classes and special classes including vegetation and hedges.

However no unstructured tsunami simulation model consider bottom roughness coefficient based on building condition in densely populated region. Thus, the objective of this study is to propose a method for tsunami inundation modeling considering spatial variation of bottom roughness coefficient variation in constructed environment.

3. NUMERICAL MODEL

Tsunami numerical modeling in this study is carried out with the method which is shown in Figure 2.

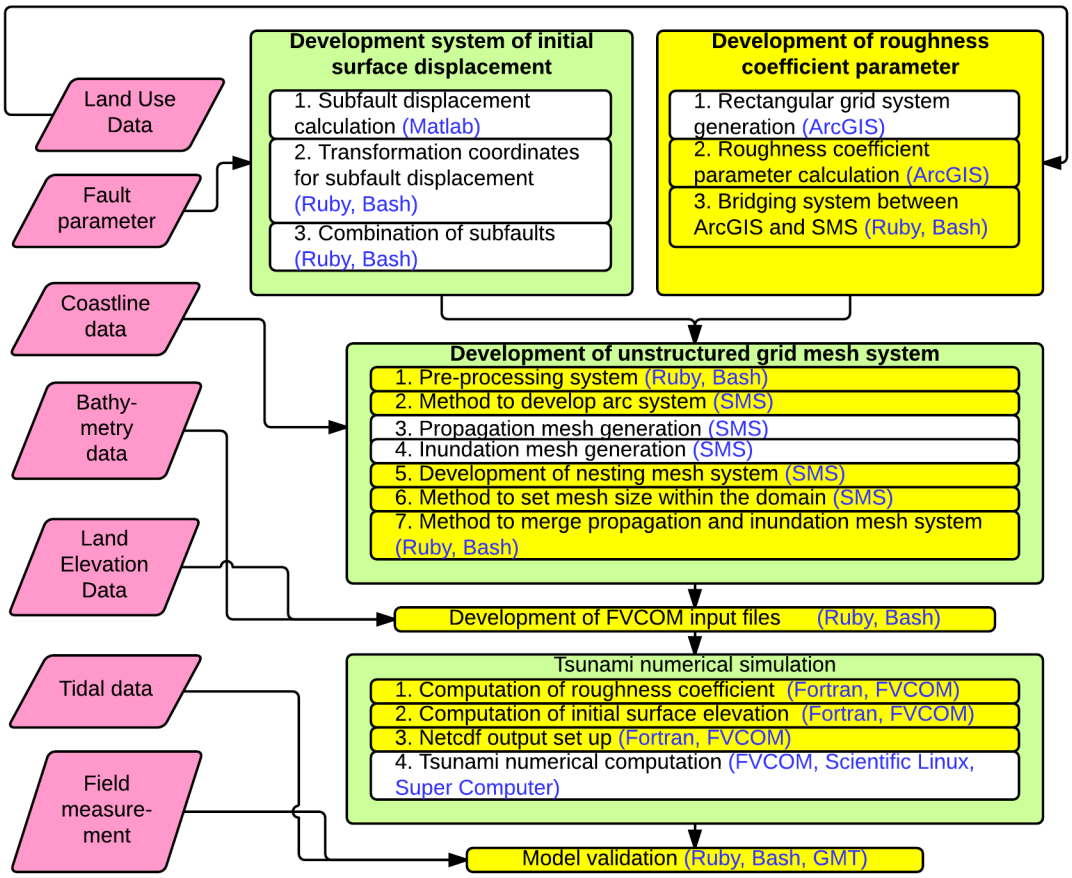

Figure 2 Numerical model flow chart

Firstly, fault parameter is utilized to develop initial surface displacement adopting Okada 1985. At the same stage roughness coefficient parameter is developed utilizing land use data. Secondly, coastline data is utilized to develop unstructured grid mesh system including propagation mesh system and inundation mesh system using SMS. After unstructured grid mesh system is finished, bathymetry and land elevation data are proceeded to develop FVCOM input files.

FVCOM input files are copied to Super Computer system to carry out tsunami numerical computation using FVCOM. After the simulation is finished, netcdf output files

are processed using Ruby and bash script including GMT to validate the simulation result. The tidal data and field measurement are necessary for model validation.

In this study there are several necessary tools to conduct tsunami simulation:

a. Surface-water modeling System (SMS, http://www.aquaveo.com/downloads)
   This software will be adopted to generated triangular mesh.
b. FVCOM (http://fvcom.smast.umassd.edu/FVCOM/index.html)
   Finite Volume Coastal Ocean Model is an unstructured and free coastal ocean circulation model. This model was developed by Chen et al.(2003). In this study FVCOM 2.6.1 and FVCOM 3.2 are utilized for tsunami simulation.
c. MATLAB (http://www.mathworks.com/products/matlab)
   This software is used to generate initial surface elevation.
d. Hidemaru editor (http://hide.maruo.co.jp/software/hidemaru.html)
   This text editor is used to open and edit the input and output files. This text editor has more ability to edit text than the usual notepad which is usually already installed in Windows.
e. Linux (e.g. Scientific Linux, https://www.scientificlinux.org/)
   Linux is used to execute the bash script or Ruby program in developing mesh and showing the results.
f. Vmware (http://www.vmware.com)
   Vmware is utilized as tool to open Linux inside Windows System.
g. PROJ (http://trac.osgeo.org/proj/)
   PROJ is projection tool, which is necessary to be installed in Linux.
h. Ruby and Dennou Ruby (http://www.ruby-lang.org/en/ and http://ruby.gfd-dennou.org/)
   Ruby is an open source language programming, which is useful in pre- and post-process of tsunami modeling.
i. Bash Script
   Bash script is used to send commands from Ruby to Linux system.

In this chapter, adopted tools (FVCOM and method of developing the fault model) and modified tools (development of roughness coefficient parameters, unstructured grid mesh system, FVCOM input files, numerical simulations and validation method) are discussed.

3.1. Adopted tools

In this sub chapter, adopted tools such as FVCOM and development system of initial surface elevation are discussed.

3.1.1. FVCOM

FVCOM was initially developed by a team effort led by C. Chen in 1999 at the University of Georgia with support from Georgia Sea Grant College Program. The first manuscript was published in 2003 (Chen et al., 2003). Chen moved to the School of Marine Science and Technology at the University of Massachusetts-Dartmouth and settled the Marine Ecosystem Dynamics Modeling Laboratory. The model development members was led by C. Chen and R. C. Beardsley (Woods Hole Oceanographic Institution) and together with H. Liu, T. Wang as members, they completed the original structure of FVCOM. Series of validation experiments were conducted. Conversion of FVCOM to Fortran 90/95 was carried out, the coding structure was modularized and the capability for parallel computation was added with team led by G. Cowles. The first FVCOM User Manual was published in 2004 (FVCOM v2.4) then the second one was published in 2006 (FVCOM v2.6) The latest code was origin of FVCOM v3.0 which is fully coupled ice-ocean-wave-sediment-ecosystem model system.

In present study, FVCOM 2.6.1 and FVCOM 3.2 are utilized for simulation. Although non-hydrostatic approximation is available in FVCOM 3.2, the current study has been using the hydrostatic approximation mode. Thus, it is not appropriate for a very small-scale convection or highly nonlinear internal gravity wave dynamics. If the very small-scale convection will be modeled, the non-hydrostatic approximation version of FVCOM should be used. However in this study, a very small scale and nonlinear terms are not necessary to modeled because we are discussing the propagation and inundation simulation in the medium scale (5 m grid scale). Thus, the non-hydrostatic version is not utilized in the current study.

In FVCOM3.2, the governing equations consist of momentum, continuity, temperature, salinity, and density equations as follow:

$$\frac{\partial u}{\partial t}+u\frac{\partial u}{\partial x}+v\frac{\partial u}{\partial y}+w\frac{\partial u}{\partial z}-fv=-\frac{1}{\rho_0}\frac{\partial\left(p_H+p_a\right)}{\partial x}-\frac{1}{\rho_0}\frac{\partial q}{\partial x}+\frac{\partial}{\partial z}\left(K_m\frac{\partial u}{\partial z}\right)+F_u \qquad (1)$$

$$\frac{\partial v}{\partial t}+u\frac{\partial v}{\partial x}+v\frac{\partial v}{\partial y}+w\frac{\partial v}{\partial z}-fu=-\frac{1}{\rho_0}\frac{\partial\left(p_H+p_a\right)}{\partial y}-\frac{1}{\rho_0}\frac{\partial q}{\partial y}+\frac{\partial}{\partial z}\left(K_m\frac{\partial v}{\partial z}\right)+F_v \qquad (2)$$

$$\frac{\partial w}{\partial t}+u\frac{\partial w}{\partial x}+v\frac{\partial w}{\partial y}+w\frac{\partial w}{\partial z}=-\frac{1}{\rho_0}\frac{\partial q}{\partial z}+\frac{\partial}{\partial z}\left(K_m\frac{\partial w}{\partial z}\right)+F_w \tag{3}$$

$$\frac{\partial u}{\partial x}+\frac{\partial v}{\partial y}+\frac{\partial w}{\partial z}=0 \tag{4}$$

$$\frac{\partial T}{\partial t}+u\frac{\partial T}{\partial x}+v\frac{\partial T}{\partial y}+w\frac{\partial T}{\partial z}=\frac{\partial}{\partial z}\left(K_h\frac{\partial T}{\partial z}\right)+F_T \tag{5}$$

$$\frac{\partial S}{\partial t}+u\frac{\partial S}{\partial x}+v\frac{\partial S}{\partial y}+w\frac{\partial S}{\partial z}=\frac{\partial}{\partial z}\left(K_h\frac{\partial S}{\partial z}\right)+F_S \tag{6}$$

$$\rho=\rho(T,S,p) \tag{7}$$

where *x, y,* and *z* represent the east, north, and vertical axes in the Cartesian coordinate system; *u, v,* and *w* represent the *x, y,* and *z* velocity components; ρ represents the density; P_a represents the air pressure at the sea surface; P_H represents the hydrostatic pressure; *q* represents the non-hydrostatic pressure; *f* represents the Coriolis parameter; *g* represents the gravitational acceleration; *T* represents the temperature; *S* represents the salinity; K_m represents the vertical eddy viscosity coefficient; and K_h represents the thermal vertical eddy diffusion coefficient. F_u, F_v, F_T, and F_S are the horizontal momentum, thermal, and salt diffusion terms. The total water column depth is $D = H + \zeta$, where *H* represents the bottom depth (relative to z=0) and ζ is the height of the free surface (relative to z=0). $p = p_a + p_H + q$ represents the total pressure, where the hydrostatic pressure p_H satisfies

$$\frac{\partial p_H}{\partial z}=-\rho g \Rightarrow p_H=\rho_0 g\zeta+g\int_{-z}^{0}\rho dz' \tag{8}$$

The surface and bottom boundary conditions for *u, v* and *w* are calculated as follow:

$$K_m\left(\frac{\partial u}{\partial z},\frac{\partial v}{\partial z}\right)=\frac{1}{\rho_0}\left(\tau_{sx},\tau_{sy}\right),\ w=\frac{\partial\zeta}{\partial t}+u\frac{\partial\zeta}{\partial x}+v\frac{\partial\zeta}{\partial y}+\frac{E-P}{\rho},\quad at\ z=\zeta(x,y,t) \tag{9}$$

$$K_m\left(\frac{\partial u}{\partial z},\frac{\partial v}{\partial z}\right)=\frac{1}{\rho_0}\left(\tau_{bx},\tau_{by}\right),\ w=-u\frac{\partial H}{\partial x}-v\frac{\partial H}{\partial y}+\frac{Q_b}{\Omega},\quad at\ z=-H(x,y) \tag{10}$$

where $\left(\tau_{sx},\tau_{sy}\right)$ are the *x* and *y* components of surface wind, Q_b is the groundwater volume flux at the bottom, Ω is the area of the groundwater source and the *x* and *y* components of bottom stresses are

$$\left(\tau_{bx},\tau_{by}\right)=C_d\sqrt{u^2+v^2}\,(u,v) \tag{11}$$

The roughness coefficient C_d is determined using the law of the wall, by matching a logarithmic bottom layer to the model at a height z_{ab} above the bottom as follow

$$C_d = \max\left(k^2 / \left(\ln \frac{z_{ab}}{z_0} \right)^2, C_{\min} \right) \tag{12}$$

where k is the Von Karman constant (0.4), z_0 is the bottom roughness parameter in meters, z_{ab} is height above the bottom in meters, and C_{min} is the minimum value of drag coefficient.

To obtain a smooth representation of irregular bottom topography, the σ-coordinate transformation is used in the vertical direction of FVCOM. The σ-coordinate transformation is defined as:

$$\sigma = \frac{z-\zeta}{H+\zeta} = \frac{z-\zeta}{D} \tag{13}$$

where σ varies from -1 at the bottom to 0 at the surface.

FVCOM was originally coded for local Cartesian coordinate system. It is suitable for regional modeling but not for basin- or global-scale applications. Further a spherical-coordinate version of FVCOM is built to make FVCOM flexible for either regional or global applications.

In the present study the 2-D (vertically integrated) module is activated. The 2-D (vertically integrated) momentum and continuity equations in Cartesian coordinate system are written as

$$\frac{\partial \zeta}{\partial t} + \frac{\partial (\overline{u} D)}{\partial x} + \frac{\partial (\overline{v} D)}{\partial y} = 0 \tag{14}$$

$$\begin{aligned} &\frac{\partial \overline{u} D}{\partial t} + \frac{\partial \overline{u}^2 D}{\partial x} + \frac{\partial \overline{u}\overline{v} D}{\partial y} - f\overline{v} D - D\overline{F}_u - G_x - \frac{\tau_{sx} - \tau_{bx}}{\rho_0} \\ &= -gD\frac{\partial \zeta}{\partial x} - \frac{D}{\rho_0}\frac{\partial P_a}{\partial x} - \frac{g}{\rho_0}\int_{-1}^{0}\left\{ J\left[\int_r^0 J\left(\frac{\partial \rho}{\partial x} + \frac{\partial \rho}{\partial r'}\frac{\partial r'}{\partial x} \right) dr' \right] \right\} dr' \\ &- \frac{1}{\rho_0}\int_{-1}^{0}\left(\frac{\partial qJ}{\partial x} + \frac{\partial qA_1}{\partial r} \right) dr' \end{aligned} \tag{15}$$

$$\begin{aligned} &\frac{\partial \overline{v} D}{\partial t} + \frac{\partial \overline{u}\overline{v} D}{\partial x} + \frac{\partial \overline{v}^2 D}{\partial y} - f\overline{u} D - D\overline{F}_v - G_y - \frac{\tau_{sy} - \tau_{by}}{\rho_0} \\ &= -gD\frac{\partial \zeta}{\partial y} - \frac{D}{\rho_0}\frac{\partial P_a}{\partial y} - \frac{g}{\rho_0}\int_{-1}^{0}\left\{ J\left[\int_r^0 J\left(\frac{\partial \rho}{\partial x} + \frac{\partial \rho}{\partial r'}\frac{\partial r'}{\partial y} \right) dr' \right] \right\} dr' \\ &- \frac{1}{\rho_0}\int_{-1}^{0}\left(\frac{\partial qJ}{\partial y} + \frac{\partial qA_2}{\partial r} \right) dr' \end{aligned} \tag{16}$$

where $J = \partial z / \partial r$, A_1 and A_2 are coordinate transformation coefficients defined as $A_1 = J\partial r / \partial x$ and $A_2 = J\partial r / \partial y$.

where G_x and G_y are expressed as

$$G_x = \frac{\partial \overline{u}^2 D}{\partial x} + \frac{\partial \overline{u}\overline{v} D}{\partial y} - D\widetilde{F}_x - \left[\frac{\partial \overline{u^2} D}{\partial x} + \frac{\partial \overline{uv} D}{\partial y} - D\overline{F}_x \right] \tag{17}$$

$$G_y = \frac{\partial \overline{u}\overline{v} D}{\partial x} + \frac{\partial \overline{v}^2 D}{\partial y} - D\widetilde{F}_y - \left[\frac{\partial \overline{uv} D}{\partial x} + \frac{\partial \overline{v^2} D}{\partial y} - D\overline{F}_y \right] \tag{18}$$

and

$$D\widetilde{F}_x \approx \frac{\partial}{\partial x}\left[2\overline{A}_m H \frac{\partial \overline{u}}{\partial x} \right] + \frac{\partial}{\partial y}\left[\overline{A}_m H \left(\frac{\partial \overline{u}}{\partial y} + \frac{\partial \overline{v}}{\partial x} \right) \right] \tag{19}$$

$$D\widetilde{F}_y \approx \frac{\partial}{\partial x}\left[\overline{A}_m H \left(\frac{\partial \overline{u}}{\partial y} + \frac{\partial \overline{v}}{\partial x} \right) \right] + \frac{\partial}{\partial y}\left[2\overline{A}_m H \frac{\partial \overline{v}}{\partial y} \right] \tag{20}$$

$$D\overline{F}_x \approx \frac{\partial}{\partial x} \overline{2A_m H \frac{\partial u}{\partial x}} + \frac{\partial}{\partial y} \overline{A_m H \left(\frac{\partial u}{\partial y} + \frac{\partial v}{\partial x} \right)} \tag{21}$$

$$D\overline{F}_y \approx \frac{\partial}{\partial x} \overline{A_m H \left(\frac{\partial u}{\partial y} + \frac{\partial v}{\partial x} \right)} + \frac{\partial}{\partial y} \overline{2A_m H \frac{\partial v}{\partial y}} \tag{22}$$

where A_m and A_h are the horizontal eddy and thermal diffusion coefficients, respectively. The overbar represented the vertical integration.

3.1.2. Development system of initial surface displacement

Initial surface displacement is initial condition of tsunami numerical simulation which is expressed by spatial variation of water surface elevation. Initial surface displacement was developed from earthquake in the fault located in the sea bed. In order to develop initial surface displacement, there are several necessary steps as follow:

a. Subfault displacement calculation

   Subfault displacement calculation is performed adopting Okada (1985). The equations are discussed in this sub chapter. As input files, following fault parameters are necessary: sub fault geometry (depth, strike, dip, length, width) and dislocation components (rake and slip). Beauducel (2009) developed Matlab script to compute solution of Okada (1985) for the surface deformation due to tensile faults in an elastic half-space. Sasaki (2011) added Matlab scripts to put subfault parameters and make subfault figures. Subfault figures are necessary to make sure that the input fault parameters are correctly defined.

b. Transformation coordinates for subfault displacement

After calculating the subfault displacement in the original coordinate, the subfault displacement is transformed to UTM coordinate using Ruby and Bash scripts by Sasaki (2011).

c. Combination of subfaults

All subfaults are combined to develop one complete initial surface displacement using Ruby and bash scripts by Sasaki (2011).

Fault parameters (see Figure 3) are utilized to obtain initial surface elevation for tsunami simulation. In this sub chapter, the initial surface elevation calculations described by Okada (1985) are summarized.

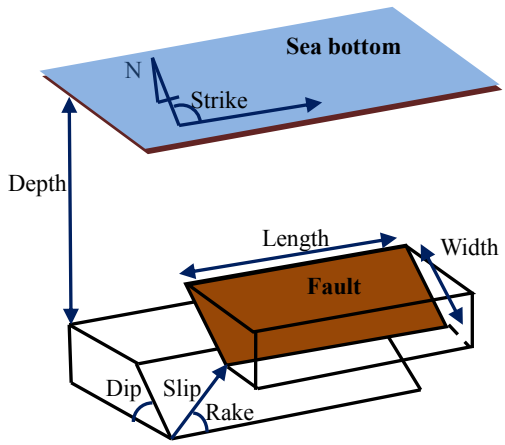

Figure 3 Fault plane.

Beauducel (2009) computed solution of Okada (1985) for displacements, tilts and strains due to fault dislocation. He developed Matlab script to calculate analytical solution for the surface deformation due to tensile faults in an elastic half-space. The necessary input data for calculation are the rectangular fault geometry (length, width, depth, strike, dip) and dislocation components (rake, slip and open).

Okada (1985) checked and review the closed analytical expression which are already published then he added an unknown solution for the displacements, strains, and tilts. He showed analytical expression of the surface displacements, strains, and tilts due to inclined shear and tensile faults in a half-space for both point and finite rectangular sources. In this study the finite rectangular sources analytical expressions are utilized to calculate the initial surface elevation of tsunami. Expressions developed by Okada (1985) are summarized in this section.

The Cartesian coordinate system was taken for calculation. Strike direction of the fault is parallel to the x axis. A finite rectangular fault with length L and width W, the deformation field was derived by taking $x - \xi'$, $y - \eta' \cos\delta$ and $d - \eta' \sin\delta$ in place of x, y, and d in the equations obtained in the point source formula.

The Chinnery's notation || was used to express the substitution

$$f(\xi,\eta)\| = f(x,p) - f(x,p-W) - f(x-L,p) + f(x-L,p-W) \tag{23}$$

In order to calculate initial surface displacement, the following equations are calculated.

For strike-slip

$$\begin{cases} u_x = -\dfrac{U_1}{2\pi}\left[\dfrac{\xi q}{R(R+\eta)} + \tan^{-1}\dfrac{\xi\eta}{qR} + I_1\sin\delta\right]\Bigg\| \\ u_y = -\dfrac{U_1}{2\pi}\left[\dfrac{\tilde{y}q}{R(R+\eta)} + \dfrac{q\cos\delta}{R+\eta} + I_2\sin\delta\right]\Bigg\| \\ u_z = -\dfrac{U_1}{2\pi}\left[\dfrac{\tilde{d}q}{R(R+\eta)} + \dfrac{q\cos\delta}{R+\eta} + I_4\sin\delta\right]\Bigg\| \end{cases} \tag{24}$$

For dip-slip

$$\begin{cases} u_x = -\dfrac{U_2}{2\pi}\left[\dfrac{q}{R} - I_3\sin\delta\cos\delta\right]\Bigg\| \\ u_y = -\dfrac{U_2}{2\pi}\left[\dfrac{\tilde{y}q}{R(R+\xi)} + \cos\delta\tan^{-1}\dfrac{\xi\eta}{qR} - I_1\sin\delta\cos\delta\right]\Bigg\| \\ u_z = -\dfrac{U_2}{2\pi}\left[\dfrac{\tilde{d}q}{R(R+\xi)} + \sin\delta\tan^{-1}\dfrac{\xi\eta}{qR} - I_5\sin\delta\cos\delta\right]\Bigg\| \end{cases} \tag{25}$$

For tensile fault

$$\begin{cases} u_x = \dfrac{U_3}{2\pi}\left[\dfrac{q^2}{R(R+\eta)} - I_3\sin^2\delta\right]\Bigg\| \\ u_y = \dfrac{U_3}{2\pi}\left[\dfrac{-\tilde{d}q}{R(R+\xi)} - \sin\delta\left\{\dfrac{\xi q}{R(R+\eta)} - \tan^{-1}\dfrac{\xi\eta}{qR}\right\} - I_1\sin^2\delta\right]\Bigg\| \\ u_z = \dfrac{U_3}{2\pi}\left[\dfrac{\tilde{y}q}{R(R+\xi)} + \cos\delta\left\{\dfrac{\xi q}{R(R+\eta)} - \tan^{-1}\dfrac{\xi\eta}{qR}\right\} - I_5\sin^2\delta\right]\Bigg\| \end{cases} \tag{26}$$

Where

$$
\begin{cases}
I_1 = \dfrac{\mu}{\lambda+\mu}\left[\dfrac{-1}{\cos\delta}\dfrac{\varepsilon}{R+d}\right] - \dfrac{\sin\delta}{\cos\delta} I_5 \\
I_2 = \dfrac{\mu}{\lambda+\mu}\left[-\ln(R+\eta)\right] - I_3 \\
I_3 = \dfrac{\mu}{\lambda+\mu}\left[\dfrac{1}{\cos\delta}\dfrac{\tilde{y}}{R+\tilde{d}} - \ln(R+\eta)\right] + \dfrac{\sin\delta}{\cos\delta} I_4 \\
I_4 = \dfrac{\mu}{\lambda+\mu}\dfrac{1}{\cos\delta}\left[\ln\left(R+\tilde{d}\right) - \sin\delta\ln(R+\eta)\right] \\
I_5 = \dfrac{\mu}{\lambda+\mu}\dfrac{2}{\cos\delta}\tan^{-1}\dfrac{\eta(X+q\cos\delta)+X(R+X)\sin\delta}{\xi(R+X)\cos\delta}
\end{cases}
\tag{27}
$$

and if cos δ=0

$$
\begin{cases}
I_1 = -\dfrac{\mu}{2(\lambda+\mu)}\dfrac{\xi q}{(R+d)^2} \\
I_3 = \dfrac{\mu}{2(\lambda+\mu)}\left[\dfrac{\eta}{R+\tilde{d}} + \dfrac{\tilde{y}q}{\left(R+\tilde{d}\right)^2} - \ln(R+\eta)\right] \\
I_4 = -\dfrac{\mu}{\lambda+\mu}\dfrac{q}{R+\tilde{d}} \\
I_5 = -\dfrac{\mu}{\lambda+\mu}\dfrac{\xi\sin\delta}{R+\tilde{d}}
\end{cases}
\tag{28}
$$

$$
\begin{cases}
p = y\cos\delta + d\sin\delta \\
q = y\sin\delta - d\cos\delta \\
\tilde{y} = \eta\cos\delta + q\sin\delta \\
\tilde{d} = \eta\sin\delta - q\cos\delta \\
R^2 = \xi^2 + \eta^2 + q^2 = \xi^2 + \tilde{y}^2 + \tilde{d}^2 \\
X^2 = \xi^2 + q^2
\end{cases}
\tag{29}
$$

When cos δ = 0, we must be careful that there are two cases of sin δ = +1 and -1.

Using the formulas developed by Okada (1985) initial surface elevation of one subfault model is calculated. The calculated initial surface elevation is transformed to the spherical coordinate to match the coordinate on tsunami simulation.

If fault model contains several subfaults, after calculating initial surface elevation of each subfault, initial surface elevation of subfaults are combined to develop initial surface elevation of complete fault model. The initial surface elevation is used as input file on tsunami simulation.

3.2. Modified tools

In this sub chapter, modified tools are discussed.

3.2.1. Development of roughness coefficient parameter

In this study roughness coefficient based on land use and building condition in densely populated region is utilized. Imai et al. (2013) considered a new approach of roughness coefficient calculation for small grid as follow

$$C = \sqrt{\frac{100-\theta}{100} n_0^{\,2} + \frac{\theta}{100}\frac{C_D}{2gk} D^{4/3}} \tag{30}$$

where n_0 is Manning's roughness coefficient, θ is the building occupancy ratio in the computational grid, C_D is drag coefficient (C_D=3.0 according to Simamora et al. (2007)), k is the horizontal scale of houses, and d is the modeled flow depth. The above equation is applied in FVCOM codes to calculate roughness coefficient.

In order to compute building occupancy ratio and horizontal scale of houses in the inundation area, the necessary steps are:

a. Reading polygon data of building on ArcGIS/QGIS (See Figure 4a)
b. Rectangular grid system generation (See Figure 4b)

   ArcGIS or QGIS can be used to generate rectangular grid system. The size of rectangle is set to be same as the triangular mesh size for inundation area.
c. Interpolating wooden houses data to grid cells (See Figure 4c)

   In order to interpolate houses data to grid cells, one has to know which polygons are wooden houses (which will be replaced by roughness parameters data) and which polygons are concrete buildings (which should be resolved). Wooden houses data are interpolated to grid cells while concrete polygons are deleted in ArcGIS/QGIS.
d. Roughness coefficient parameter calculation (See Figure 4d)

   Using the land use data of focusing area, roughness coefficient parameters are calculated on ArcGIS/QGIS as follow:

   1) horizontal scale of houses are calculated by taking square root of houses area on each rectangular mesh
   2) building occupancy ratio is calculated by taking the percentage of houses area on each rectangular mesh

After calculation is finished, the center location of parameter are determined for each rectangular grid. The data is ready to be exported to unstructured grid mesh to generate FVCOM input files.

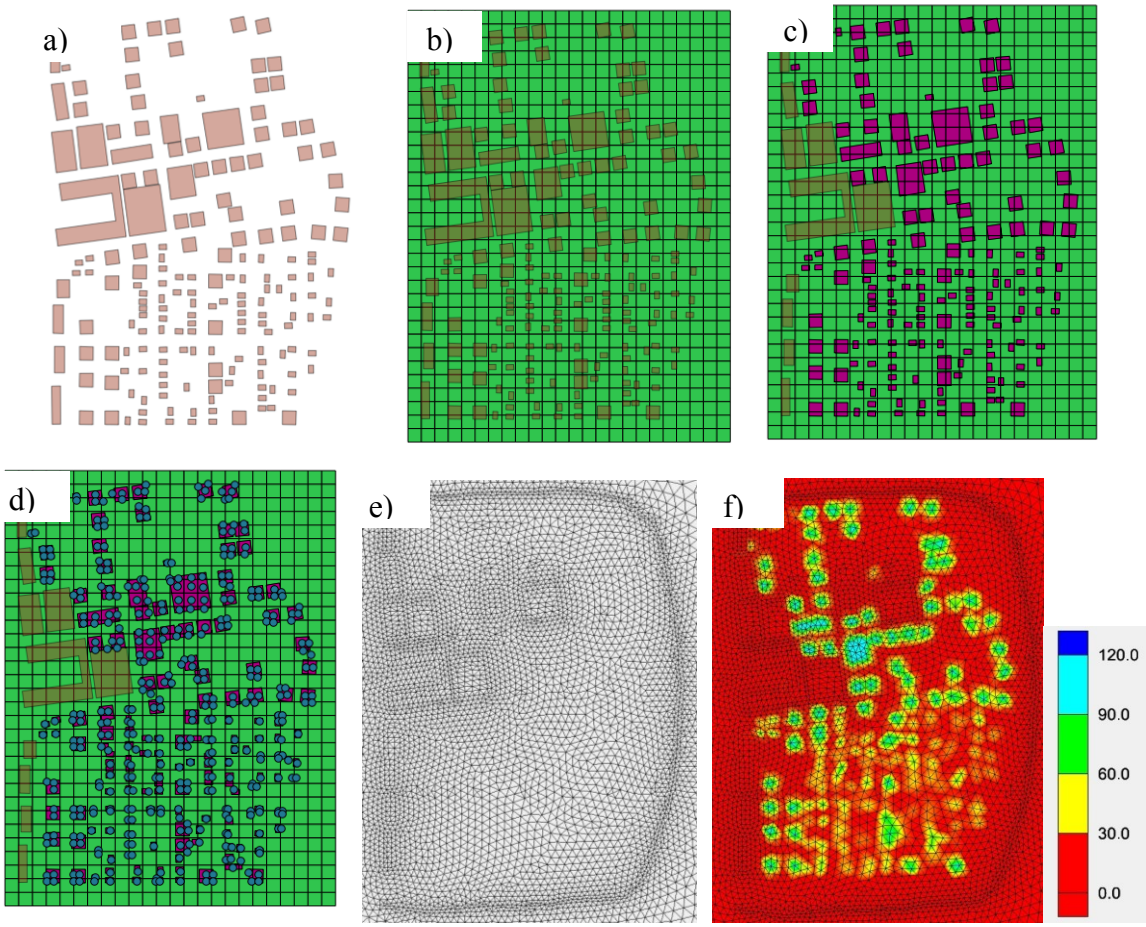

Figure 4 Development of roughness coefficient parameter: a) Reading polygon data of building; b) Creating rectangular mesh system; c) Interpolating wooden houses to grid cells; d) Calculation of roughness coefficient parameters; e) Unstructured grid mesh ; f) Building occupancy ratio on unstructured grid mesh.

e. Bridging system between ArcGIS/QGIS output and SMS

After roughness coefficient parameters are calculated on ArcGIS, the value of parameters are available in the cells where houses are existed. However, in order to export the values to SMS, it is necessary to put zero values in other cells where houses are not existed. Thus, Ruby and Bash scripts are written as bridging scripts between ArcGIS output and SMS input files. Using those scripts, roughness parameters are interpolated to unstructured grid mesh system using SMS. Figure 4e shows unstructured

grid mesh while Figure 4f shows building occupancy ratio data after being interpolated to the unstructured grid mesh.

3.2.2. Development of unstructured grid mesh system

One advantage of using FVCOM is its ability to simulate an unstructured mesh system. By using the unstructured grid mesh system, large size of elements in propagation area and small size of elements in inundation area are able to be simulate together. However, the quality of each mesh should be kept in order to make the simulation stable.

Several steps to develop an unstructured grid mesh system are:

- Pre-processing system
- Method to develop arc mesh system
- Development of nesting mesh system
- Method to set mesh size within the domain
- Unstructured grid mesh generation
- Method to resolve building in inundation area

Each step is discussed below.

1. Pre-processing system

Coastline data and bathymetry data are necessary to develop FVCOM input files. In order to prepare coastline data and bathymetry data, the raw data should be processed in the following steps:

- Converting the spherical coordinates data to Cartesian coordinates data

  Unstructured mesh system in SMS is prepared in Cartesian coordinate. Thus, coastline and bathymetry data are necessary to be projected to Cartesian coordinate before it is used. *Proj* is utilized inside bash script to convert the coordinate system to Cartesian coordinate.

- Converting the raw coastline data format to cst format

  Raw coastline data format consists of nodes of each line, while each lines are separated by certain symbol. The format is necessary to be changed so that the coastline data can be read by SMS. Additional data such as total number of lines, number of nodes in one line and indicator value of line (0 for open and 1 for closed coastline) are necessary in the cst format. Ruby and bash script are utilized to change the format.

2. Method to develop arc mesh system

Surface-water Modeling System (SMS) is a graphical user interface tool that is utilized to make the unstructured mesh system. It is necessary to use an effective way to develop an unstructured grid mesh system. Several necessary steps to develop arc mesh system are discussed below.

- Creating an initial open boundary

  Open boundary has important role in numerical simulation. The smooth open boundary leads to more stable simulation than the steep open boundary. If the open boundary condition and sponge layer are not utilized, open boundary has to be placed in a proper place so that wave reflection will not interfere with incoming wave.

- Connecting all line segments into one arc

  Coastlines usually consist of many segments. It is necessary to connect all line segments into one arc in order to make arc mesh system. However, usually errors arise in the connection process because there are overlapped or unconnected segments. The usual treatment is by zooming in every segments and checking whether there are overlapped or unconnected segments, correcting them, and move to another segment to be corrected. Disadvantage of this method is time consuming. Moreover, sometimes error of segments could not be detected. In order to avoid the above problem, it is necessary to make sure that in one arc there is only one point exists for closed coastline or two points for opened coastline. If the requirement is satisfied, it is easier to connect all segments into one arc. The steps are as follow:

  - Putting appropriate spacing for all coastlines including open boundary coastlines
  - Converting all points in the simulation domain and convert them to vertices.
  - Making sure that in one arc there is only one point for closed coastline or two points for opened coastline.
  - Checking only coastlines that does not follow the above requirement and correct the coastlines. If all errors are corrected, the arc is ready for the next step for mesh building.

3. Nesting mesh system

In tsunami simulation, the global mesh system covering tsunami propagation area is indispensable. However, using global mesh system alone is not enough. There are areas where detailed mesh system is required:

a. Fault model area

   It is necessary to built detailed mesh system in fault area to reproduce well the initial surface elevation in the source location.

b. Coastline and inundation area

   It is necessary to develop detailed mesh system in coastline and inundation area to reproduce well run up wave in inundation area

SMS as a tool to develop unstructured grid mesh system may be crashed if one build very large mesh system at once. In order to avoid the failure, a nesting mesh system method is utilized to build whole mesh system. A global mesh system is firstly developed. The global mesh system is considered as a basis to make several local meshes.

In order to make whole mesh system, the following steps are introduced:

a. Generating a global mesh system
b. Preparing global nodes (nodestring) to connect the global mesh to the local meshes
c. Deleting the existing triangular meshes in the local area
d. Generating local meshes for local areas (fault model area, coastline and inundation area)
e. Preparing nodestring to connect the local meshes to the global mesh
f. Connecting the local meshes to the global mesh

4. Method to keep the mesh size

To develop a reliable simulation, mesh size is one of the key option. By knowing the mesh size variation on a simulation, one may be possible to judge how accurate the simulation reproduce real condition. As for tsunami simulation, there are two areas where the mesh size has to be controlled.

The first is fault model area. Fault model or source area is the place where the fault is located. The movement of fault in the sea bed will produce the initial surface elevation. The second is run up area. Run up is the location in inundation area where the maximum height is reached by tsunami.

The method to keep the mesh size is introduced below:

a. Developing coastline to define simulation domain

b. Distributing vertices in the coastline following the necessary mesh size in the area
c. Preparing imaginary coastline around the real coastline by making circle or circle-like lines in the area where the same mesh size is necessary. Straight or steep angle lines should be avoid so error will not arise.
d. Distributing vertices in the imaginary coastlines to set the appropriate mesh size. It is necessary to make sure that vertices are developed properly so there are no abrupt change in the vertices size.
e. Building polygon and triangular mesh system for whole domain.

5. Unstructured mesh generation

In this study mesh generation is conducted using Surface-water modeling system (SMS). In FVCOM User Manual (Chen et al., 2013), unstructured mesh generation method is discussed. In this study, unstructured mesh generation method is slightly modified in order to prepare large mesh system for tsunami simulation.

Mesh system contains triangular elements with different mesh size. Large mesh sizes are located in open boundary in the ocean while small mesh sizes are located in source area, coastal and inundation area. In order to propose an easy way to construct unstructured grid mesh system, mesh generation processes are divided into four section:

1) Propagation area mesh system
2) Source area mesh system
3) Local propagation area mesh system
4) Inundation area mesh system

Relationship between four mesh systems are shown in Figure 5.

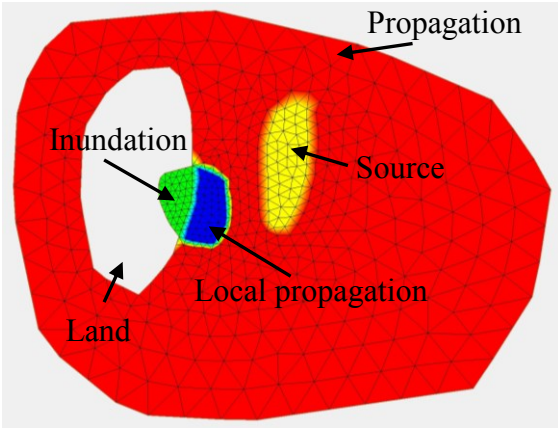

Figure 5 Relationship between four mesh systems

Area with triangular system are simulation domain while area without triangular mesh is land which is not included in tsunami simulation domain. Each mesh system is connected each other by nodestring (global nodes). Generation process of each mesh system is conducted in separated SMS files and finally local meshes are connected to make a whole unstructured mesh system.

Main mesh system is propagation area mesh system (red). It is the first mesh system that one has to generate. Boundary of propagation area is coastline and open boundary in the ocean. After propagation area mesh system is finished, source area or local propagation area together with inundation area can be generated simultaneously. In this example boundary of source area mesh system is propagation area mesh system. However, it depends on fault location in each tsunami. Boundary of local propagation and inundation area mesh system is propagation area and land.

Basically, process of mesh generation are identical. The difference between local meshes are mesh size and boundary. Generally, mesh system is constructed by the following steps:

a. Coastlines development

   Coastlines including boundary are necessary to be developed using the available data set before developing the mesh system. After coastlines are created, coastlines are necessary to be refined following the required grid size. In the open boundary area, large value grid size e.g. 50 km is acceptable. However in the fault model area, where the initial surface elevation is placed, smaller grid size is necessary (e. g. 1 km). As for coastline of the focusing area, 5 m grid size is necessary to make sure that wave inundation can be resolved well.

b. Mesh building

   There are four mesh systems which are necessary to be built which are discussed in this sub chapter: propagation area, source area, local propagation area, and inundation area mesh system.

c. Mesh quality control

   Mesh quality control is necessary to be set in order to build a high quality mesh system so that a stable simulation can be achieved. After mesh quality control is set, one must make sure that all cells in the mesh system fulfill the requirement. If it is not, the cell must be corrected until no error signs are observed in the mesh system.

d. Mesh checking

Mesh checking is another checking system in SMS to make sure that unconnected nodes are not exist inside the mesh system. If unconnected nodes exist, one should delete them or connect them to the mesh system.

After mesh system is finished, bathymetry data and initial surface elevation data are interpolated to the mesh system to make FVCOM input files. Although basic method to generate each mesh system is same, there are differences between each mesh system generation method. The differences between each mesh system generation method are discussed as follow.

1) Propagation area mesh generation

Propagation area is location where wave propagates from the fault model area (source area) to the coastline. There are several important things regarding propagation area mesh generation as follow:

a. Propagation area needs to include fault area.
b. Propagation area needs to include the coastline of focusing area
c. If open boundary condition is not utilized, one should make sure that the wave reflection does not disturb the focusing area.

In this study, propagation area mesh sizes range from 50 km in ocean area and gradually change to smaller size until about 1 km in source area. Source area is a part of propagation area located in fault area where initial surface elevation is defined. It is necessary to generate source area mesh generation in separated process so initial surface elevation can be resolved better using smaller grid size than other propagation area.

2) Source area mesh generation

The difference between propagation area mesh generation and source area mesh generation is the boundary. In this study, boundary of source area is propagation area because source area is located inside propagation area.

Source area is the location where earthquake occurred. The benefit of generating source area mesh generation dependent from propagation area mesh generation is to reduce possibility of SMS model to be crashed and to ease mesh generation process.

Because source area is the origin of tsunami, it is necessary to resolve the area well. As for the 2011 Tohoku Tsunami case, 1 km grid size is adopted in this study to resolve the source area. Source area grid size can be decided based on desired accuracy of each case.

3) Local propagation area mesh generation

Local propagation area is a part of propagation area which is located close to inundation area. This mesh system may be generated together with inundation area because the size is quite small compared to propagation or source area mesh system. Boundary of local propagation area is propagation area and coastline of inundation area (see Figure 5). The largest mesh size is located at nodestring (close to propagation area mesh system) and the smallest mesh size is located in coastline. In this study, mesh size in coastline is 5 m.

4) Inundation mesh generation

Inundation area is the land area that is considered to be inundated by tsunami. Before deciding inundation area, it is necessary to have rough estimation about the inundation area location and size. It is recommended to develop inundation area mesh system larger than the estimated one so if the simulation results are wider than the assumed area, the same mesh system still can be used.

In order to reproduce acceptable results of inundation modeling, small grid size (i.e. 5 m) is necessary. However, if the inundation area is too large and the focusing area is located in one specific area in the inundation area, it is necessary to put different mesh sizes in inundation area. Large mesh sizes are located not in focusing area while small mesh sizes are located in the focusing area. Using this method, the number of elements and nodes in the mesh system could be reduced.

6. Method to resolve building in inundation area

Typical procedure to resolve buildings are to apply one of the two methods below:

1) Resolving all buildings and include building heights into simulation
2) Not resolving buildings and building heights are not included into calculation while bottom friction is calculated in building area.

This study proposed a new method as follow:

1) Resolving all concrete buildings and include concrete building heights into simulation
2) Not resolving wooden houses, while bottom friction is calculated in wooden houses area.

Detailed method are discussed in Chapter 4.3.

3.2.3. Development of FVCOM input files

In order to conduct tsunami simulation using FVCOM, there are several necessary input files. The input files for FVCOM 2.6.1 are:

1) Casename_bfw.dat: Bottom freshwater input values including number of sources, time, and discharge rate, etc. In this study, bottom freshwater value is zero. Thus, zero is simply written in the input file.
2) Casename_cor.dat: Latitudes of triangular nodes which are used to calculate the Coriolis parameter. This is a data array with three columns (*x*, *y, and Lat.*) where *x* and *y* are the location and *Lat.* is latitude of individual node point on each triangular mesh. Total rows of this array are equal to the total number of node points. Ruby and Bash scripts are developed to create this input file from SMS output file.
3) Casename_dep.dat: Water depth at all node points. This is a data array with three columns (*x*, *y, and d*) where *x* and *y* are the location and *d* is water depth of individual node points. Total rows of this array are equal to the total number of node points. The depth in FVCOM is specified at the node point. This input file is created using SMS.
4) Casename_elj_obc.dat: Tidal amplitudes at the open boundary (for the case with Julian time). In tsunami case tidal amplitudes are not considered therefore zero is simply written in the input file.
5) Casename_el_ini.dat: Initial field of surface elevation at nodes. The data is written in a one column file with a total number of rows equal to the total number of nodes. No specific format is required. The unit of the water elevation is meters. This input file is created using SMS.
6) Casename_grd.dat: The grid input file consists of two parts: 1) integral numbers identifying elements and nodes and (2) the x and y locations of individual nodes. Ruby and Bash scripts are developed to create this input file from SMS file (2dm file).
7) Casename_its.dat: Initial fields of the water temperature and salinity. In this study temperature and salinity are not considered so the default constant values are given for this input file.
8) Casename_jmpobc.dat: Identification number of open boundary nodes where a frictional geostrophic inflow correction is made. There is no open boundary in the present tsunami case and thus zero is simply written in the input file.

9) Casename_lag_ini.dat: The initial positions of particles to be tracked using Lagrangian tracking. In this study, there is no particle to be tracked and thus the default input file is used.
10) Casename_mc.dat: Meteorological forcing values: wind velocity, heat flux and precipitation/evaporation. This input file is used only for a spatially uniform meteorological forcing case. In this study, meteorological forcing is not considered and thus the default input file is utilized.
11) Casename_obc.dat: Forcing values at open boundary nodes. In this tsunami case no open boundary is considered, therefore zero is simply written after the header information in this file.
12) Casename_riv.dat: River discharge data including number of rivers, discharge volume, discharge temperature, and discharge salinity. In this tsunami case, no river is considered and thus the default input file is adopted.
13) Casename_spg.dat: Parameters for a sponge layer for damping at the open boundary. Because in this tsunami case no open boundary is considered, zero is simply written in this file.
14) Casename_uv_ini.dat: The initial field of currents at individual triangular centroids. In this tsunami case the initial currents are zero. Thus, zero values are put based on the number of nodes and sigma levels in the simulation.
15) Casename_run.dat: Set up parameters controlling the model run.
16) Casename_teta.dat: Roughness coefficient parameters including building occupancy ratio, horizontal scale of houses, and masks. This is a data array with four columns (building occupancy ratio, horizontal scale of houses, friction factor for unconstructed area, mask). Mask value is 1.0 for constructed area and 0.0 for other area. Total rows of this array are equal to the total number of node points. Roughness parameters can be obtained by processing polygon building data on ArcGIS/QGIS. By using Ruby and Bash scripts, parameters are transferred to SMS. SMS output file is utilized to develop this input file.

Input files for FVCOM 3.2 are different from those of FVCOM 2.6.1. Input files for FVCOM 3.2 are divided into two types:

1) ASCII format input files (casename_cor.dat, casename_dep.dat, casename_grd.dat, casename_obc.dat, casename_spg.dat, sigma.dat, casename_el_ini.dat).

Basically the ASCII format input files are the same as the format for FVCOM 2.6.1. The notable difference is additional note about node number and element number in the input files. Details are available in FVCOM User Manual (Chen et al., 2013).

2) NetCDF format input files (casename_julian_obc.nc, casename_brf.nc)

In this study casename_brf.nc is modified from the existing format discussed in FVCOM User Manual so that it is compatible to put friction parameters in node points. This input file consists of building occupancy ratio, horizontal scale of houses, friction factor for unconstructed area, and mask for every node points.

3.2.4. Tsunami numerical simulation

In tsunami numerical simulation, FVCOM is utilized as simulation tool. In order to apply roughness coefficient equation in tsunami simulation, FVCOM 2.6.1 and FVCOM 3.2 are modified as follow:

1) Computation of roughness coefficient

Roughness coefficient is applied on FVCOM 2.6.1. In subroutine user-defined of bottom roughness (brough_ud.F), roughness coefficient is calculated. Roughness coefficient calculation on FVCOM 2.6.1 is shown in Figure 6. Calculation of bottom roughness is called by the main program (us_fvcom.F). Bottom roughness calculation can be made for original equation, GOTM calculation, or user-defined calculation. If user-defined calculation is chosen, modified roughness coefficient will be calculated.

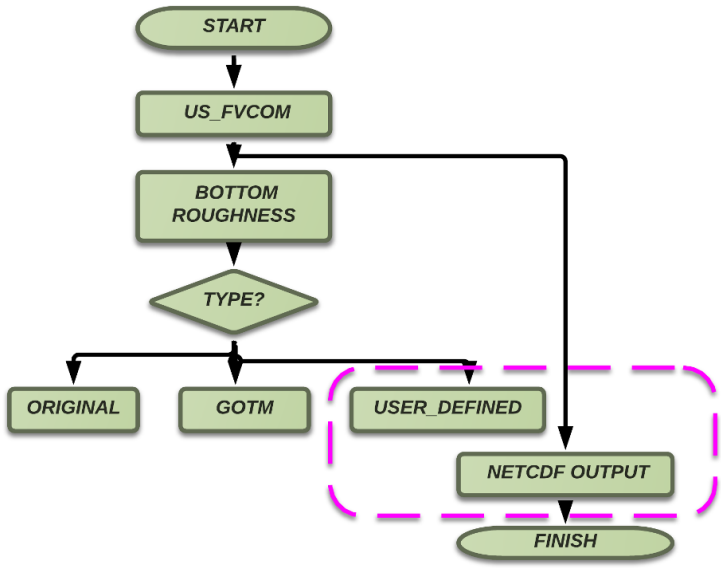

Figure 6 Flow chart of roughness coefficient calculation

On FVCOM 3.2, subroutine bottom roughness (brough.F) is modified to include calculation of roughness coefficient. In addition, several files are modified to enable the codes to read modified NetCDF input files.

2) Computation of initial surface elevation

Initial surface elevation is calculated in subroutine startup for FVCOM 2.6.1 and module mod_startup for FVCOM 3.2 to include spatial variation of initial surface elevation.

3) NetCDF output set up

NetCDF output is basically set up for surface elevation, x and y velocity, and other variables. However in order to produce other variables output which does not exist in the original NetCDF output module, further set up should be made to produce the necessary variables. The variables are:

- roughness coefficient
- maximum surface elevation
- maximum velocity

Modification is performed in module mod_ncdio. In addition, several modifications need to be made to include the calculation of maximum surface elevation and maximum velocity into the code.

Numerical simulation can be performed in Linux System or Super Computer. In the present study, Scientific Linux and Super Computer HA8000 from Kyushu University and The University of Tokyo are used to conduct the simulations.

3.2.5. Model validation method

Model validation is performed by making output figures as time series data or spatial variations at several time step in order to compare the results with the physical experiment results from the laboratory or surveyed data. Necessary software programs to extract the output and to make figures are listed below:

a. Ruby and Dennou Ruby (http://www.ruby-lang.org/en/ and http://ruby.gfd-dennou.org/)

Ruby is an open source language programming, which is useful in pre- and post-process of tsunami modeling.

b. GMT (http://gmt.soest.hawaii.edu/)

Generate Mapping Tool is used as output visualization tool of tsunami modeling.

c. Imagemagick (http://www.imagemagick.org/script/index.php)

Imagemagick is necessary to handle the "transparency" option on making output figures.

d. GNUPlot (http://www.gnuplot.info/)

GNUPlot is used to make timeseries figures.

e. Bash script

Bash script is used to send Ruby, GMT and Imagemagick command to Linux system.

4. MODEL VALIDATION

In order to confirm reliability of a model, validation is indispensable. Before performing simulation, an idealized test case is necessary to be modeled so that the simulated result can be compared with the idealized result. In this chapter validation to analytical and experimental cases are discussed.

4.1. Validation to analytical case

4.1.1. Introduction

Carrier and Greenspan (1958) investigated behavior of a wave as it climbs a sloping beach. The analysis was based on the non-linear shallow water theory. They obtained explicit solutions and it is shown that there are waves that climb a sloping beach without breaking. In this sub chapter, FVCOM are validated with the analytical solution.

Cross section of simple beach is shown in Figure 7 where η^* is water surface elevation, h^* is depth, and α is beach slope.

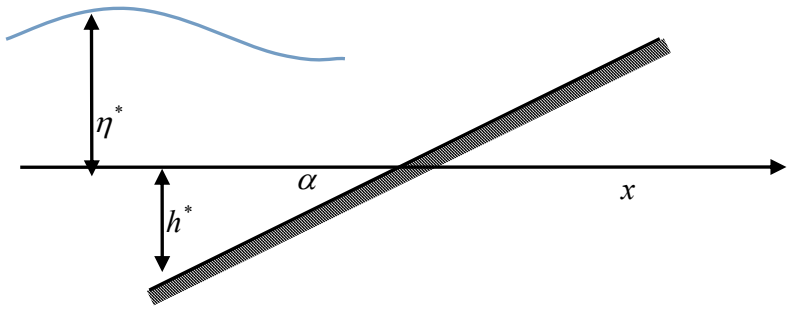

Figure 7 Simple beach sketch

4.1.2. Analytical Solution

The conservation equations of mass and momentum of the non-linear shallow-water theory are below

$$\left[v^*\left(\eta^* + h^*\right)\right]_{x^*} = -\eta^*_{t^*} \tag{31}$$

$$v^*_{t^*} + v^* v^*_{x^*} = -g\eta^*_{x^*} \tag{32}$$

where v^* is the horizontal velocity, η is water surface elevation, h^* is depth. The asterisks indicate dimensional quantities. The non-dimensional variables from above equations are below

$$v=\frac{v^*}{v_0},\quad \eta=\frac{\eta^*}{\alpha\, l_0},\quad x=\frac{x^*}{x_0},\quad t=\frac{t^*}{T},\quad T=\left(\frac{l_0}{\alpha g}\right)^{1/2},\quad v_0=\left(g l_0 \alpha\right)^{1/2} \tag{33}$$

Variable l_0 is characteristic length which can be specified for specific problem which is taken for study. The depth is uniform with $h^*=-\alpha x^*$.

After derivation of the equation, they introduced the 'potential' $\phi(\sigma,\alpha)$ so that

$$x=\frac{\phi_\lambda}{4}-\frac{\sigma^2}{16}-\frac{v^2}{2} \tag{34}$$

$$\eta=\frac{\phi_\lambda}{4}-\frac{v^2}{2} \tag{35}$$

$$t=\frac{\lambda}{2}-v \tag{36}$$

$$\left(\sigma\phi_\sigma\right)_\sigma-\sigma\phi_{\lambda\lambda}=0 \tag{37}$$

Then a particularly simple analytical solution of the equations is given by

$$\phi=AJ_0(\sigma)\cos\lambda \tag{38}$$

where J_0 is the notation for a Bessel function.

The analytical solution is utilized for generating the initial surface elevation. Initial surface elevation is applied at the initial step of simulation. The result of simulations are compared with analytical solution.

4.1.3. Analytical case modeling setup

An unstructured mesh system is developed to represent the case. The adopted case is two dimensional case and therefore the mesh system has to satisfy horizontal (x) and vertical (y) direction. For the z direction, it is necessary to take the number of grid which is representative to generate the wave.

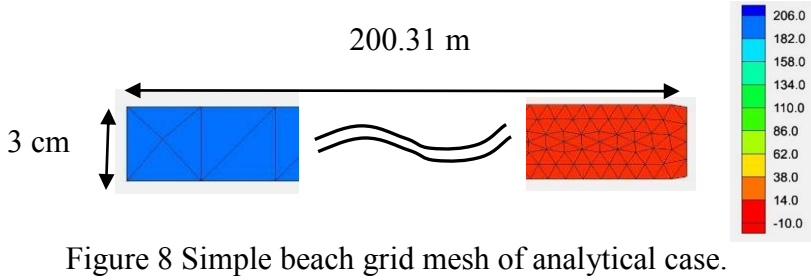

Figure 8 Simple beach grid mesh of analytical case.

Trial and error were conducted to determine computational domain length because many element in z direction may slow down the computational time. SMS (Surface-water Modeling System) 10.1 is utilized for generating the mesh in Figure 8.

The computational domain has 200.31 m length in x direction and 200.31 m for y direction, as the beach slope α is taken to be 1.0. For z direction, 3 cm length was taken to build efficient amount of element number. The mesh contains 14,049 nodes, 14,519 triangular elements with two nodes in offshore directions as open boundary. Model setup are tabulated in Table 1.

Table 1 Simulation setup of validation to analytical case

No	Setup	Number
1	l_0	1.0
2	g	9.8 m/s^2
3	α	1.0
4	$T=\left(\frac{l_0}{\alpha g}\right)^{1/2}$	0.319
5	Computational Length (x)	0.3 m ~ -200.01 m
6	Depth (y)	0.3 m ~ -200.01 m
7	Width (z)	3 cm
8	Grid Size	7 mm ~ 3 cm
9	Boundary Condition	Julian time, the sea level is specified at the open boundary with certain value every 0.063 s.

FVCOM simulation needs to satisfy criterion for numerical stability as follow

$$\Delta_{t_E} \le \frac{\Delta L}{U+\sqrt{gD}} \tag{39}$$

Where Δ_{t_E} is time step of the external mode, computational length scale ΔL is the shortest edge of an individual triangular grid element, U is magnitude of the horizontal velocity, and D is local depth. Time step of the internal mode is restricted by

$$\Delta_{t_I} \le \frac{\Delta L}{C_I} \tag{40}$$

Where C_I is maximum phase speed of internal gravity waves. Since C_I is usually smaller than $C_E = \sqrt{gD}$, Δ_{t_I} could be much larger than Δ_{t_E}. For normal applications, usually below requirement is recommended

$$I_{split} = \frac{\Delta_{t_I}}{\Delta_{t_E}} \le 10 \tag{41}$$

A larger I_{split} could be used in realistic applications, but should be fully tested to check the numerical stability and mass conservation before it is chosen.

In this study, numerical stability parameters are tabulated in Table 2.

Table 2 Numerical stability parameters of validation to analytical case

No	Parameter	Value
1	Δ_{t_E}	0.00016 s
2	ΔL	0.007 m
3	U	0.1 m/s
4	g	9.8 m/s^2
5	D	200 m
6	Δ_{t_I}	0.007 s
7	C_I	1 m/s
8	I_{split}	10

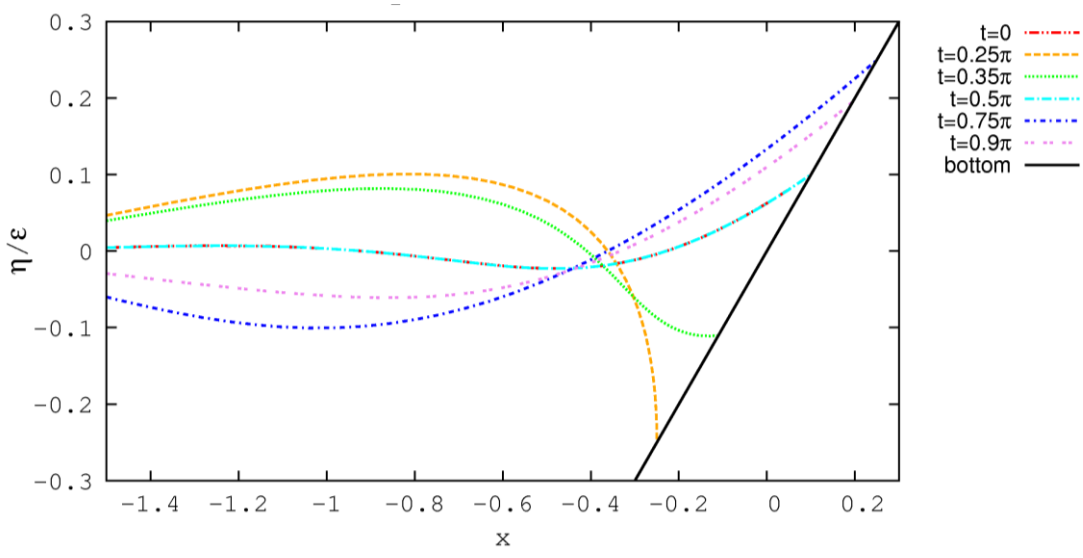

Figure 9 Analytical solutions at five time steps.

Analytical solution at five time steps are shown in Figure 9. The analytical solutions are calculated from Eq. 38.

There are two options to include generated wave into the simulations as follow:

1. Utilizing time series of surface elevations in the open boundary in the offshore side of mesh system)
2. Utilizing analytical solution at a specific time step and put the analytical solution as spatial variation of initial surface elevation

It is found that the first option affect stable results in the offshore side but unstable results are observed in the onshore side. When second option is applied, it is found that the initial wave is not stable. However, stable results in the onshore side can be obtained after several time steps. Thus, second option is utilized to generate wave for this study.

Analytical solutions at 0.25π are used as spatial variations of initial surface elevation for this simulation. Simulations were conducted utilizing single processor.

4.1.4. Analytical case results

Comparison between simulation results and analytical solutions are shown in Figure 10.

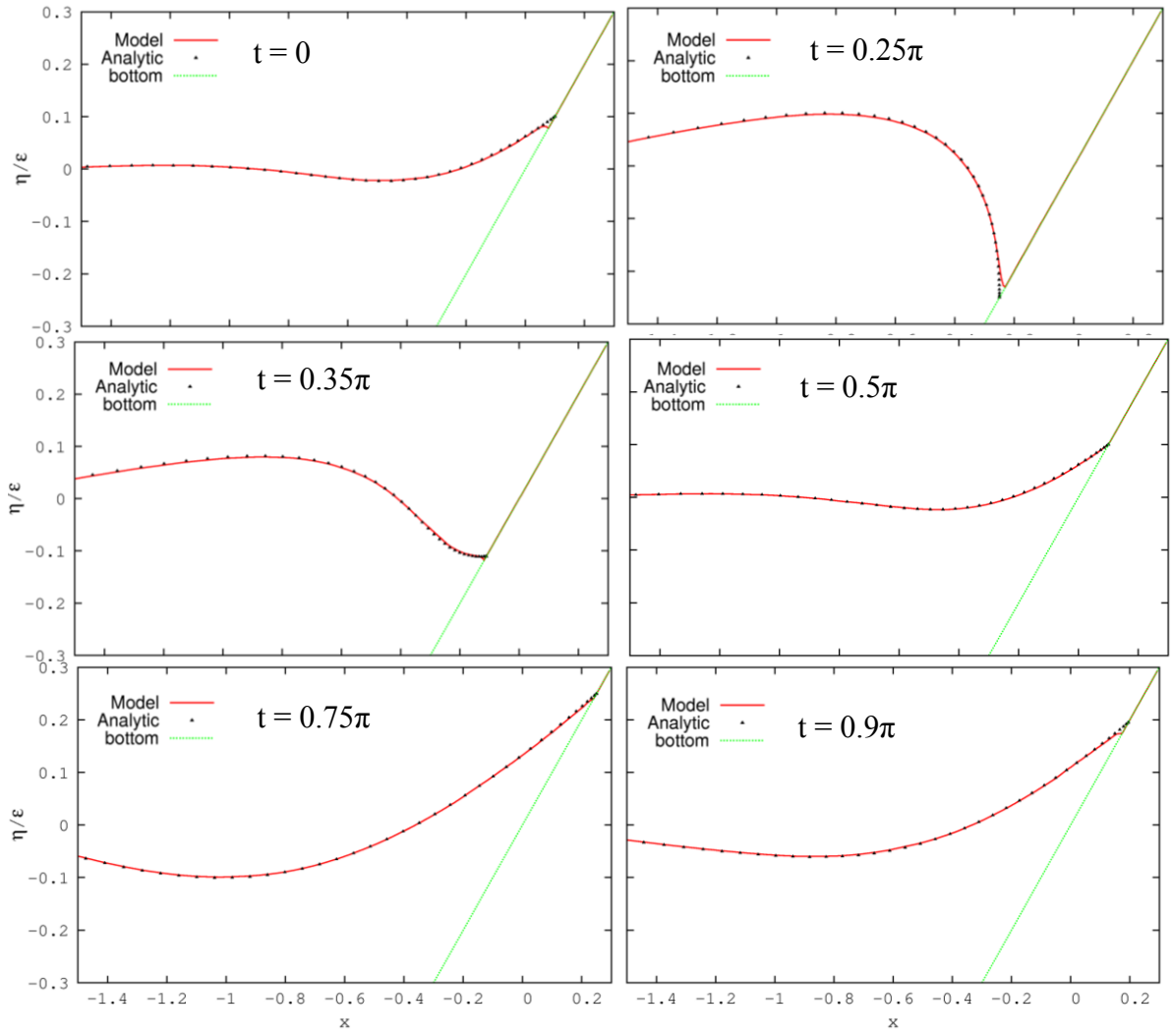

Figure 10 Comparison between simulation results and analytical solutions.

In above figures simulation results reproduced analytical solutions well. Surface elevation height and phase at 0, 0.25π, 0.35π, 0.5π, 0.75π and 0.9π are reproduced well by simulation results. In the coastline area, slight differences between analytical solutions and simulation results are observed. It may be caused by grid size in the coastline area which is quite large compared to the analytical solution and therefore could not finely resolved simulated surface elevation. Different phases are also observed between simulation results and analytical solutions. The probable cause of discrepancy is inexistence of velocity as boundary condition of simulation.

4.1.5. Sub Chapter Conclusions

Verification of wave model under simplified beach model in FVCOM has been discussed in this sub chapter. The analytical solutions by Carrier and Greenspan (1958) are reproduced by FVCOM simulation. Probable cause of the discrepancy is inexistence of velocity as boundary condition of simulation.

4.2. Validation to experimental case: influence of macro-roughness on tsunami run up

4.2.1. Introduction

In this chapter FVCOM verification are carried out using the laboratory experimental results that was conducted in the Tsunami Wave Basin (TWB) at the O. H. Hinsdale Wave Research Laboratory (HWRL) at Oregon State University. The experimental setup and results are discussed in master of Ocean Engineering thesis by Bridges, K. (2011) entitled "Influence of macro-roughness on tsunami runup and forces: large scale experiment at the NEES tsunami facility". Bathymetry setup and wave gauge locations are shown in Figure **11**.

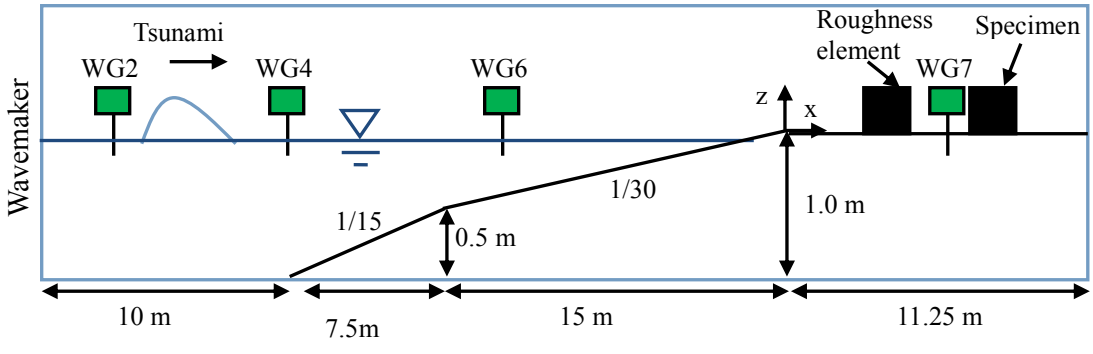

Figure 11 Bathymetry setup and wave gage locations

Wave gauges in run up area are located around the specimen as shown in Figure 12.

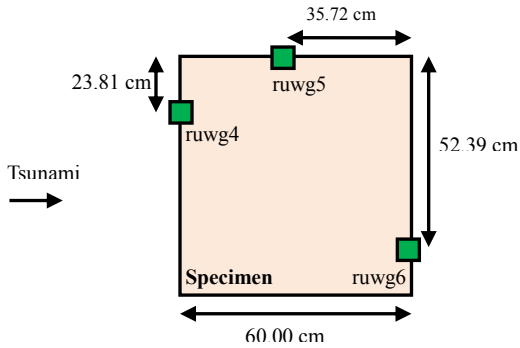

Figure 12 Run up wave gage locations at the specimen

4.2.2. Simulation set up

In this sub chapter FVCOM simulation set up to reproduce laboratory experimental results are discussed. An unstructured grid mesh system was constructed with grid size ranges from 5 cm around blocks and specimen to 10 cm in open boundary. The mesh system consists of 28,698 nodes and 56,265 triangular elements.

The mesh system comprises two parts: wave flume area in the left side and discharge area in the right side (see Figure 13). Between wave flume area and discharge area, elevated bed area was designed to reproduce wave damping in the laboratory. The discharge area was constructed to let the wave flow out from the calculation area and prevent the wave reflection to disturb the wave flume area.

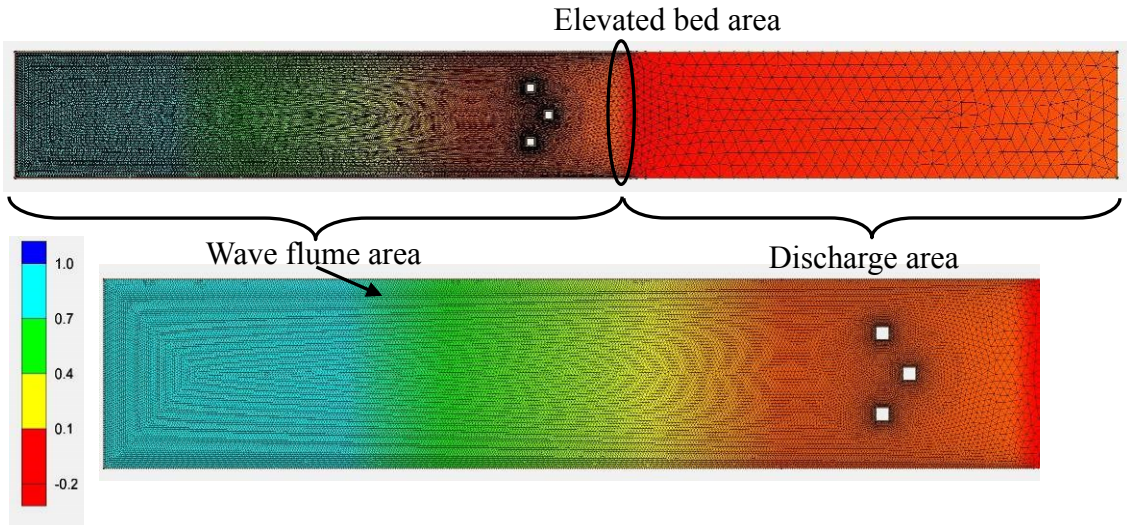

Figure 13 Unstructured grid mesh system of validation to experimental case

Bridges et al. (2011) conducted several trials with several variations of number of roughness elements and distance between specimen and roughness elements. In laboratory experiment, 60 cm x 60 cm x 60 cm blocks were used for specimen and roughness elements.

In this study, two roughness elements and one specimen were used with same dimension, 60 cm x 60 cm by cutting the triangular meshes inside the boxes. Thus, roughness elements and specimen are modeled as high wall and not blocks with 60 cm height. Although blocks are not modeled with 60 cm, this modeling method is acceptable because tsunami inundation is lower than blocks height.

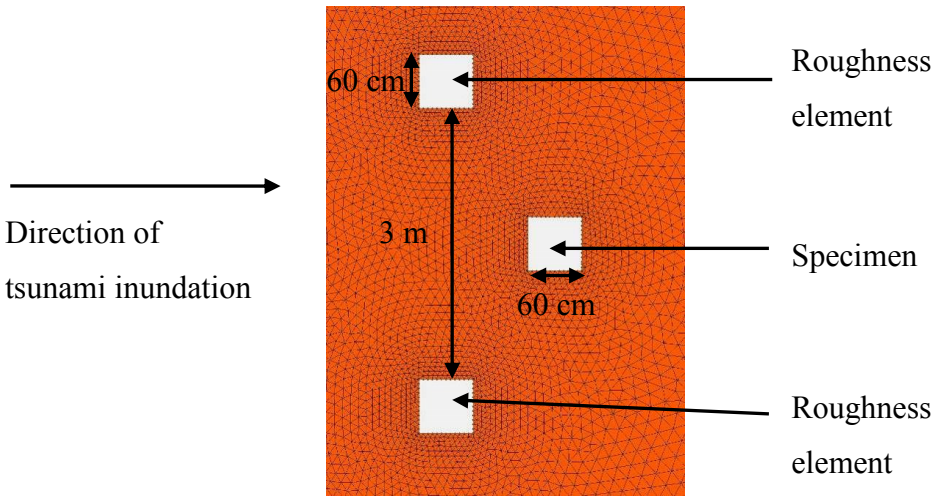

Figure 14 Mesh system around blocks and specimen

Important details about the simulation set up in this study are tabulated in Table 3.

Table 3 Simulation setup of validation to experimental case

No	Setup	Number
1	Total length (x)	74.2 m
2	Total width (y)	8.4 m
3	Total depth (z)	1.1 m (-0.195 ~ 0.905 m)
4	Grid size	5 ~ 10 cm
5	External Time Step (DTE)	0.0005 s
6	Isplit = DTI/DTE	10
7	Boundary condition	Surface elevation is specified at the open boundary (WG2) every 0.005 s

8	Initial elevation	Uniform (0.05 m)

In order to satisfy the Courant-Friedrich Levy (CFL) stability criterion (see Eq. 39-41), the utilized parameters are tabulated in Table 4.

Table 4 Numerical stability parameters of validation to experimental case

No	Parameter	Value
1	Δ_{t_E}	0.0005 s
2	ΔL	0.05 m
3	U	0.1 m/s
4	g	9.8 m/s^2
5	D	0.905 m
6	Δ_{t_I}	0.005 s
7	I_{split}	10

Simulations were conducted using FVCOM 2.6.1 on FX10, Super Computer of The University of Tokyo with 1 node in debug mode, with elapse time 30 min. A wet and dry treatment method was utilized and drag coefficient was determined from the logarithmic law of the wall posing the minimum value of 0.006.

4.2.3. Simulation results

Simulation results were taken in three wave gauges in offshore sides and three run up wave gauges. Simulation results in this study using FVCOM together with simulation results conducted by Nakamura et al. (2013) are shown in following figures.

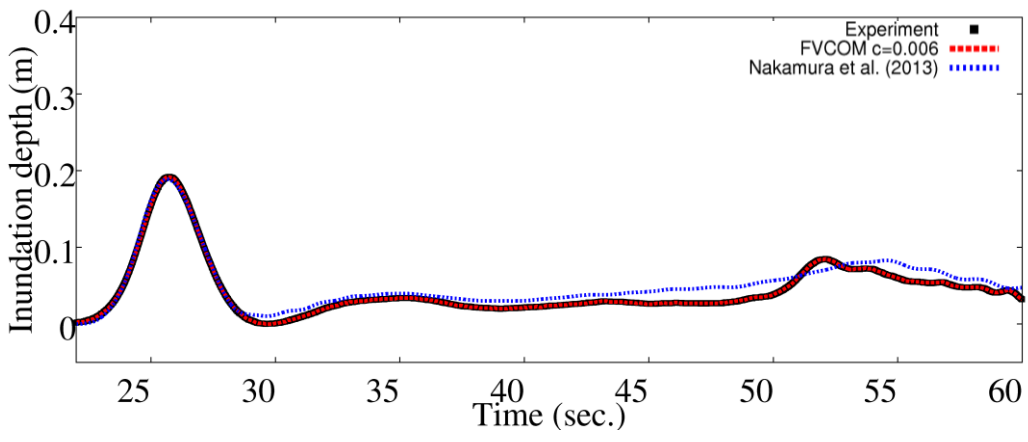

Figure 15 Simulation results at WG2

WG2 is the open boundary location of simulation. Surface elevation values are defined in this point every 0.005 s. Figure 15 shows that FVCOM simulation results reproduced experimental results at the open boundary location well. Small differences are shown by Nakamura et al. (2013) because the open boundary is not located at WG2 but in the wavemaker.

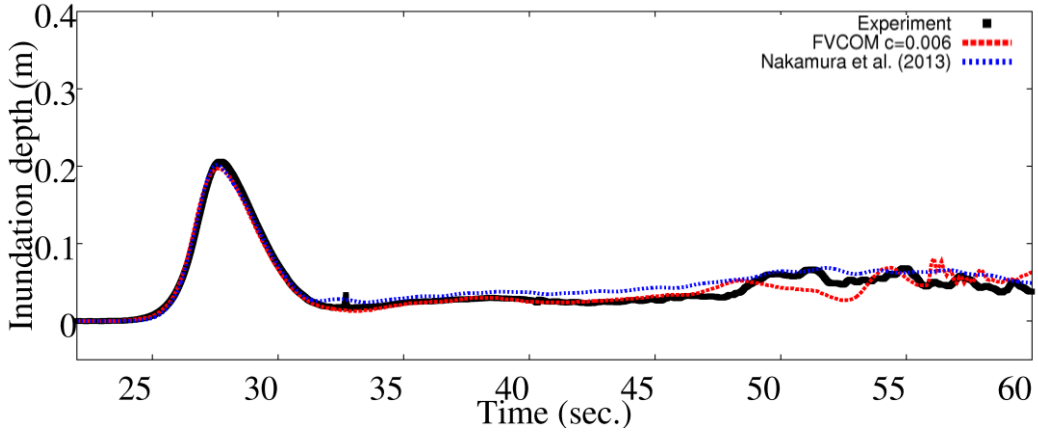

Figure 16 Simulation results at WG4

Figure 16 shows simulation results at WG4. Simulation results using FVCOM reproduced experimental trends well at WG4. At 57 s., wave reflection due to the existence of wave damping can be observed from FVCOM simulation results. Nakamura et al. (2013) also reproduced experimental results well at WG4.

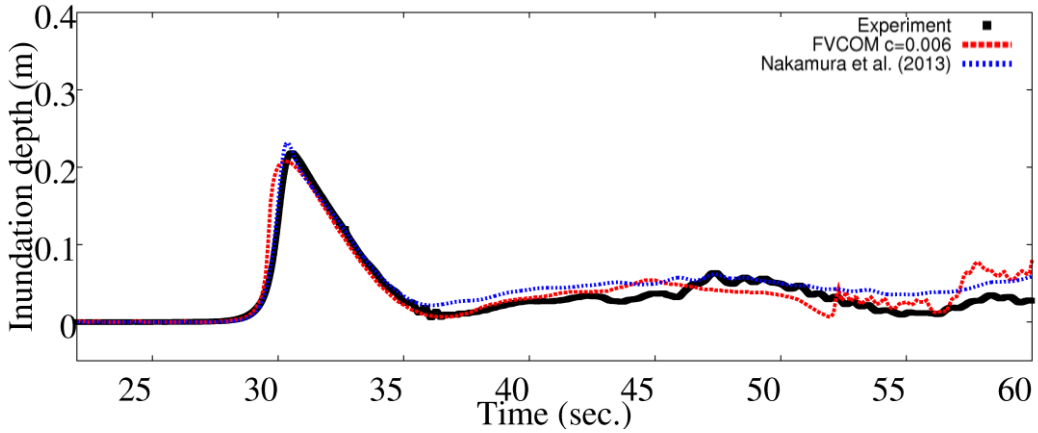

Figure 17 Simulation results at WG6

Figure 17 shows simulation results at WG6. WG6 is located in slope area. Experimental results are reproduced well by FVCOM simulation results although slight

underestimation are observed. Nakamura et al. (2013) slightly overestimated the simulation results at 31 s. At 58 s., wave reflection due to the existence of wave damping is shown by FVCOM simulation results.

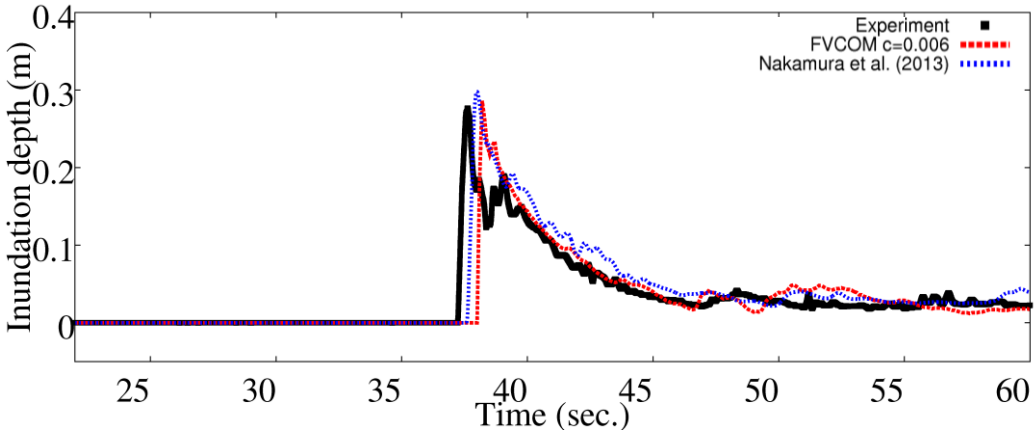

Figure 18 Simulation results at ruwg4

Figure 18 shows simulation results at ruwg4. Wave gauge ruwg4 is located at the front side of specimen. High waves at 38 s. are reproduced well by simulation results. There is slight phase difference between simulation results and experimental results. The delay may be caused by the different friction values between real condition and simulation setup. In this study, FVCOM simulation was conducted using averaged 2-D mode and therefore the turbulence could not be reproduced.

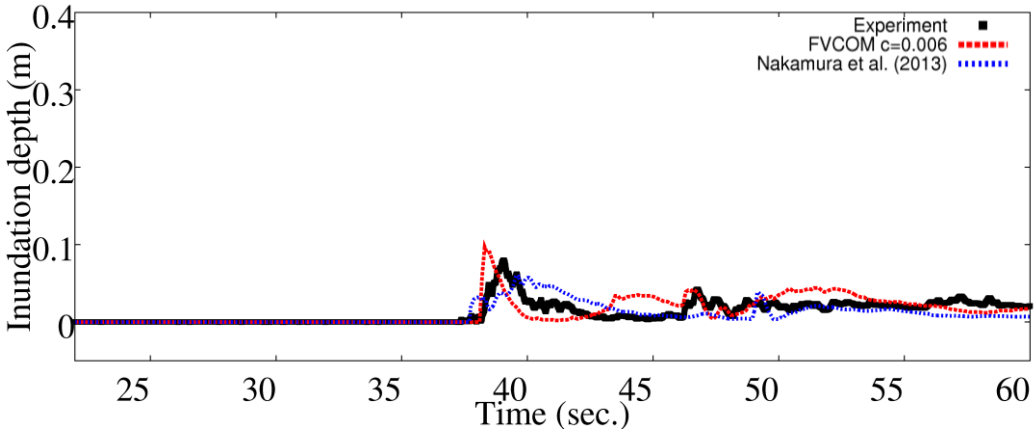

Figure 19 Simulation results at ruwg5

Figure 19 shows simulation results at ruwg5. Wave gauge ruwg5 is located at the right-hand side of the specimen. General trends of experimental results are reproduced by

FVCOM simulation results and Nakamura et al (2013). However, this study overestimates experimental results at 39-40 s. while Nakamura et al. (2013) underestimates experimental results at 39-40 s. The difference may be caused by the difference of friction factor and boundary conditions of both simulations.

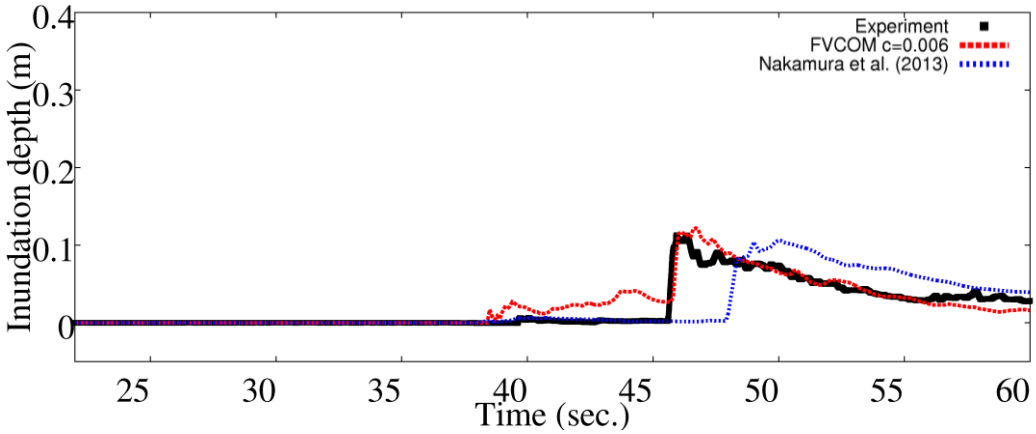

Figure 20 Simulation results at ruwg6

Figure 20 shows simulation results at ruwg6. Wave gage ruwg6 is located in the rear side of the specimen. FVCOM simulation results overestimate the experimental results at 39-46 s. while Nakamura et al. (2013) reproduce experimental results well. FVCOM reproduces phase and surface elevation well at 46-60 s while Nakamura et al. (2013) overestimates the experimental results. The surface elevation at 46-60 s. is reflection wave from the wave damping. This showed that the location and wave damping height was correctly set so the surface elevation and wave phase are reproduced well.

4.2.4. Sub Chapter Conclusions

This study shows that FVCOM is able to reproduce the physical experiment results in offshore wave gauges and run up wave gauges well. Both wave magnitude and general tendencies are well reproduced by FVCOM.

Slight phase difference between simulation results and experimental results are observed. The delay may be caused by the different friction values between real condition and simulation setup. In this study, and drag coefficient was determined from the logarithmic law of the wall posing the minimum value of 0.006.

Small wave reflections are detected at WG4 (t=56 s.) and WG6 (t=58 s.) due to existence of the wave damping. Although causing small reflections, the existence of wave damping affect the same phase of FVCOM simulation results at ruwg6.

4.3. Validation to experimental case: tsunami inundation modeling in constructed environments

4.3.1. Introduction

This sub chapter aims to validate the proposed model with the benchmark physical experimental results of Park et al. (2013). This physical experimental study is chosen because it provides results of tsunami inundation in an idealized representation of coastal area in Seaside, Oregon, where concrete buildings and wooden houses are included in the physical experiment. Physical experiment was conducted in the Tsunami Wave Basin (TWB) at the O. H. Hinsdale Wave Research Laboratory (HWRL) at Oregon State University. The experimental setup and results are discussed by Park et al. (2013) in their paper entitled "Tsunami inundation modeling in constructed environments: A physical and numerical comparison of free-surface elevation, velocity, and momentum flux".

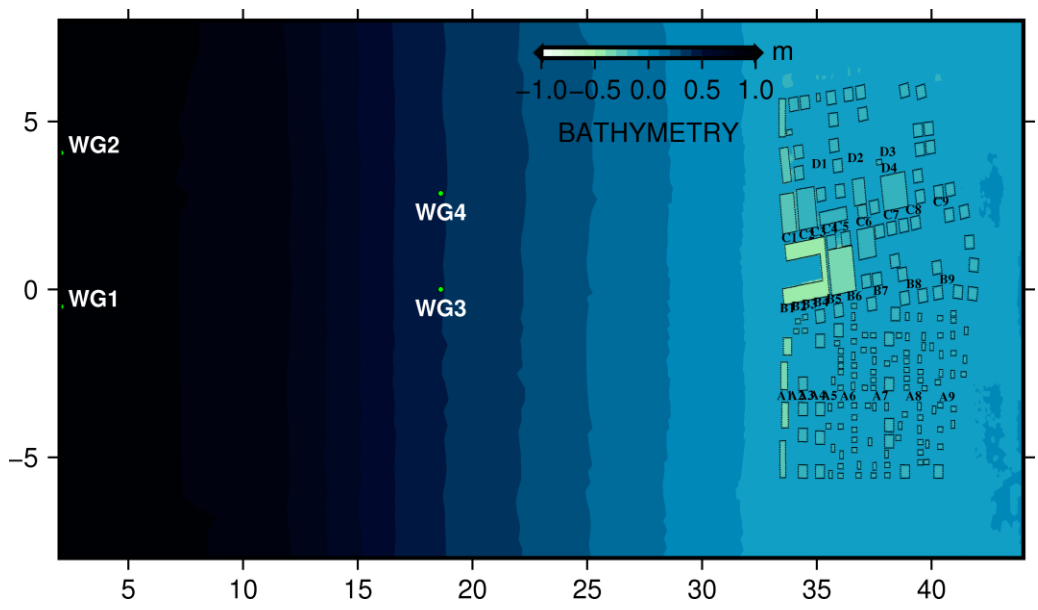

Figure 21 Bathymetry map and wave gage locations

Bathymetry map and wave gauge and wave gauge locations are shown in Figure 21. The physical model was an idealized representation of coastal area in Seaside with 1:50

undistorted scale.

Physical experiment was conducted in the rectangular basin with 48.8 m long, 26.5 m wide, and 2.1 m deep and four surface wire resistance wave gauges were fixed in the basin (WG1-WG4). In the inundation area in the right hand side, macro-roughness elements were installed as shown in Figure 22.

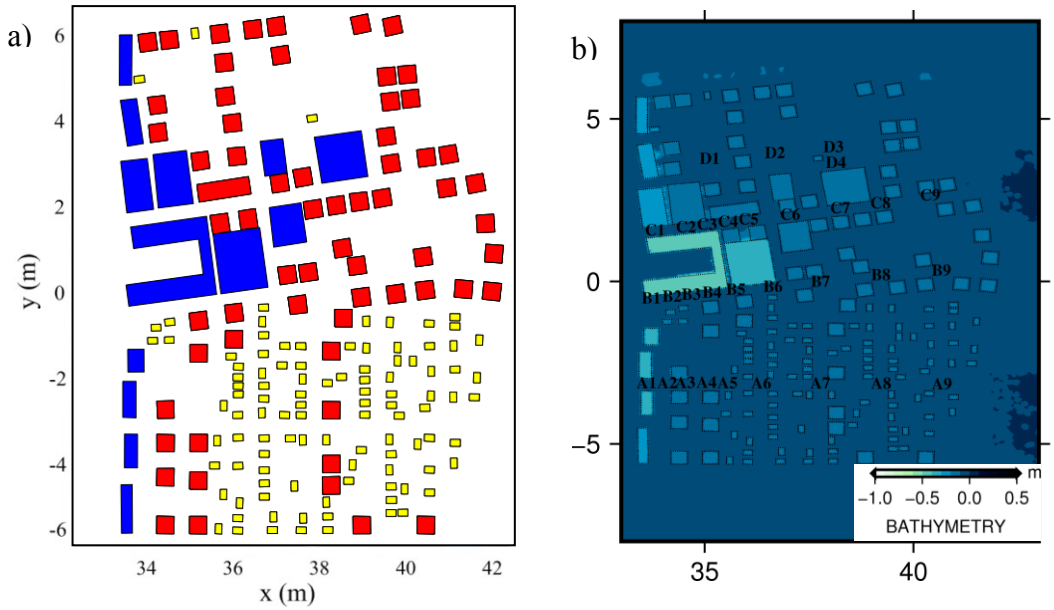

Figure 22 Plan view of: a) macro-roughness and b) measurement locations in inundation area

Colored-blocks represent buildings with following categorize:

- Blue : large hotels on the water front (considered as concrete buildings)
- Red : typical commercial buildings (considered as concrete buildings in this study)
- Yellow : residential houses (considered as wooden houses in this study)

There are 31 measurement locations divided into line A, B, C and D. Line A, B, and C are located on city streets while line D is located behind the buildings (see Figure 22b). Line A is parallel to the inundation flow direction while line B and C are inclined approximately 10º to the flow direction.

4.3.2. Simulation set up

In this sub chapter FVCOM simulation set up to reproduce laboratory experimental results: "tsunami inundation modeling in constructed environments" are discussed. Several

unstructured grid mesh systems were constructed to perform sensitivity analysis for different cases as shown in Table 5.

Table 5 Simulation types of tsunami inundation modeling in constructed environments

No	Mesh Type	Min. grid size	Elements	Nodes	BF condition	Computation Time (min.)
1	Resolved	0.05 m	106,979	53,576	Original	57
2	Resolved	0.15 m	27,159	13,666	Original	13
2	Concrete-resolved	0.15 m	15,033	7,604	Modified	7
3	Unresolved	0.15 m	20,985	10,579	Modified	11
4	Concrete-resolved	0.2 m	11,475	5,824	Modified	5
5	Unresolved	0.2 m	13,815	6,994	Modified	7
6	Concrete-resolved	0.3 m	8,181	4,174	Modified	5
7	Unresolved	0.3 m	8,339	4,256	Modified	5
8	Concrete-resolved	0.4 m	6,262	3,212	Modified	3
9	Unresolved	0.4 m	5,954	3,058	Modified	3

Bottom friction condition for resolved mesh (case 1) is original FVCOM calculation using the logarithmic law of the wall (Grant and Madsen, 1979) as follow:

$$C = \max\left(k^2 / \left(\ln \frac{Z_{ab}}{Z_0} \right)^2, C_{\min} \right) \tag{42}$$

where C is roughness coefficient, k is the Von Karman constant (0.4), z_0 is the bottom roughness parameter in meters, z_{ab} is height above the bottom in meters, and C_{min} is the minimum value of drag coefficient (C_{min}=0.001).

For other cases, modified bottom friction calculation is used. In non-constructed area, constant roughness coefficient is used (C=0.001) while in the constructed area, roughness coefficient calculation for small grid (Imai et al., 2013) is used.

$$C = \sqrt{\frac{100-\theta}{100} {n_0}^2 + \frac{\theta}{100} \frac{C_D}{2gk} D^{4/3}} \tag{43}$$

where n_0 is Manning's roughness coefficient, θ is the building occupancy ratio in the computational grid, k is the horizontal scale of houses, d is the modeled flow depth, and C_D is drag coefficient. Value of C_D was set to 3.0 according to Simamora et al. (2007).

A set of simulations was also executed for roughness coefficient *Cmin*=0.005. The simulations are carried out to test numerical sensitivity of minimum friction factors.

Table 5 show three mesh types: resolved mesh system, concrete-resolved mesh system, and unresolved mesh system. Figure 23, Figure 24 and Figure 25 are colored based on bathymetry and topography utilized in the simulation. Bathymetry and topography data are obtained from the lidar-surveyed data taken during the experiment in the laboratory (Park et al., 2013). Three types of mesh system are discussed below.

1) Resolved mesh system

Resolved mesh system (Figure 23) is constructed to build an idealized case of physical experiment case. Thus, all buildings including concrete buildings and wooden houses are resolved. Building heights are also included for all buildings.

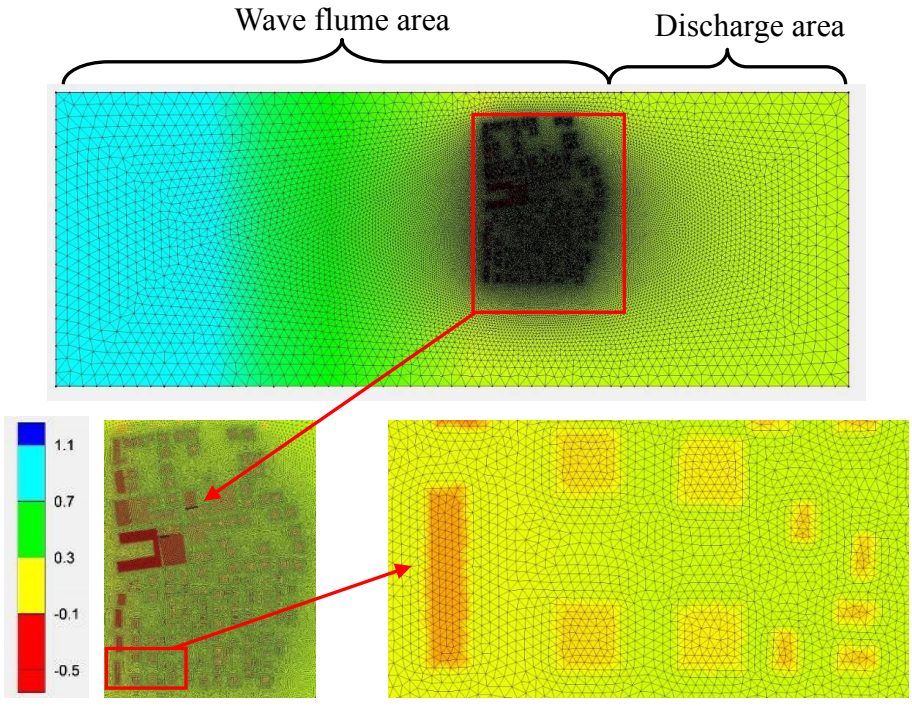

Figure 23 Resolved mesh system

2) Concrete-resolved mesh system

Concrete-resolved mesh system (Figure 24) is utilized to represent the proposed method of this study. Concrete buildings (large hotels on the front area) are resolved and concrete building heights are included. Other buildings (commercial buildings and

residential houses) are not resolved. Building heights are not included for these buildings, while roughness coefficient parameters are included to replace effects of buildings in the numerical simulations.

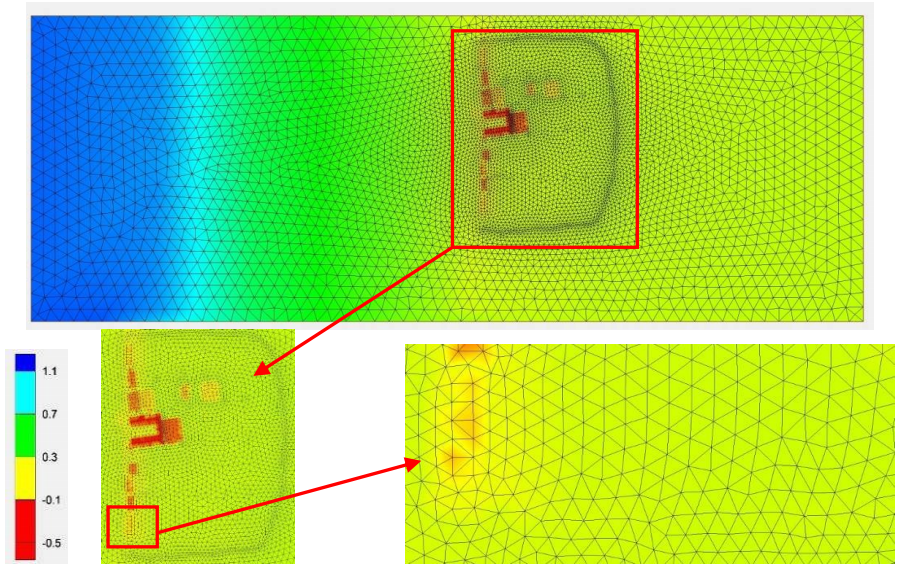

Figure 24 Concrete-resolved mesh system

3) Unresolved mesh system

Unresolved mesh system (Figure 25) is utilized to represent a typical method to apply roughness coefficient in constructed area. All buildings are not resolved. Building heights are also not included, while roughness coefficient parameters are included for all buildings.

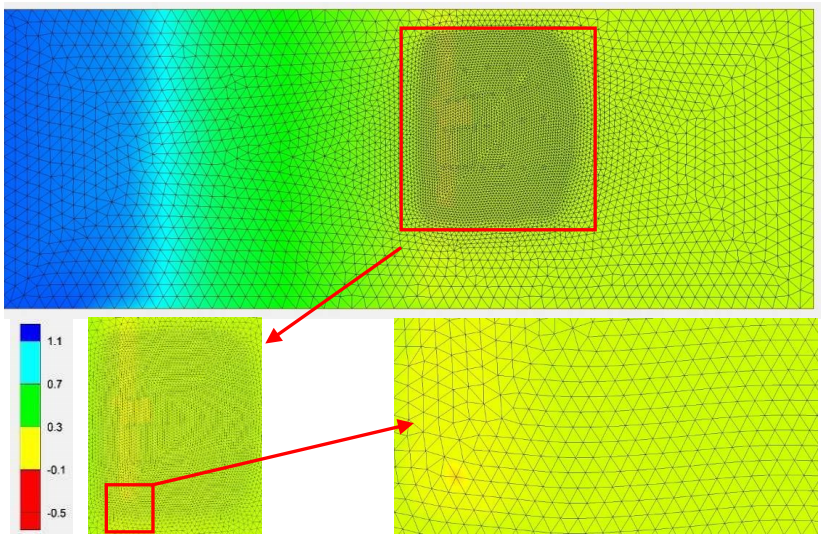

Figure 25 Unresolved mesh system

In order to satisfy the Courant-Friedrich Levy (CFL) stability criterion (see Eq. 39-

41), numerical stability parameters are set for simulations as shown in Table 6.

Table 6 Numerical stability parameter of tsunami inundation modeling in constructed environments

No	Parameter	Value
1	Δt_E	0.0005 s
2	ΔL	0.05 m
3	u	0.1 m/s
4	g	9.8 m/s^2
5	D	0.905 m
6	Δt_I	0.005 s
7	I_{split}	10

Important details about the simulation set up in this study are tabulated in table below.

Table 7 Simulation setup of tsunami inundation modeling in constructed environments

No	Setup	Number
1	Total length (x)	74.2 m
2	Total width (y)	8.4 m
3	Total depth (z)	1.1 m (-0.195 ~ 0.905 m)
4	Grid size	5 ~ 10 cm
5	External Time Step (DTE)	0.0005 s
6	Isplit = DTI/DTE	10
7	Boundary condition	Surface elevation is specified at the open boundary (WG2) every 0.02 s
8	Initial elevation	Uniform (0.05 m)

Simulations were conducted using FVCOM 2.6.1 on HA8000, Super Computer of Kyushu University with 1 node in debug mode, with elapse time 30 min. Simulation results are discussed for the following variables:

1) Inundation depth (H)

$$H = \eta - h \tag{44}$$

where η is surface elevation or inundation height, and h is ground elevation. Definition of inundation depth is shown in figure below.

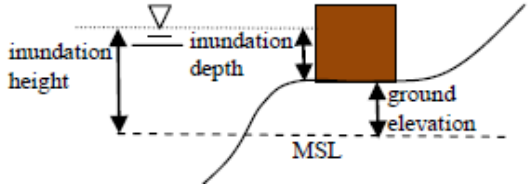

Figure 26 Definition of inundation depth

2) Maximum velocity (v_m)

$$v_m = \sqrt{u_a^{\,2} + v_a^{\,2}} \tag{45}$$

where v_a is vertically averaged y-velocity and u_a is vertically averaged x-velocity or cross shore velocity.

4.3.3. Spatial variation of surface elevation

Spatial variation of surface elevation for case 1 (resolved mesh) and case 2 (concrete-resolved mesh with 0.15 m grid size) are discussed in this sub chapter. Comparison of spatial variation of surface elevation for several time steps are shown below.

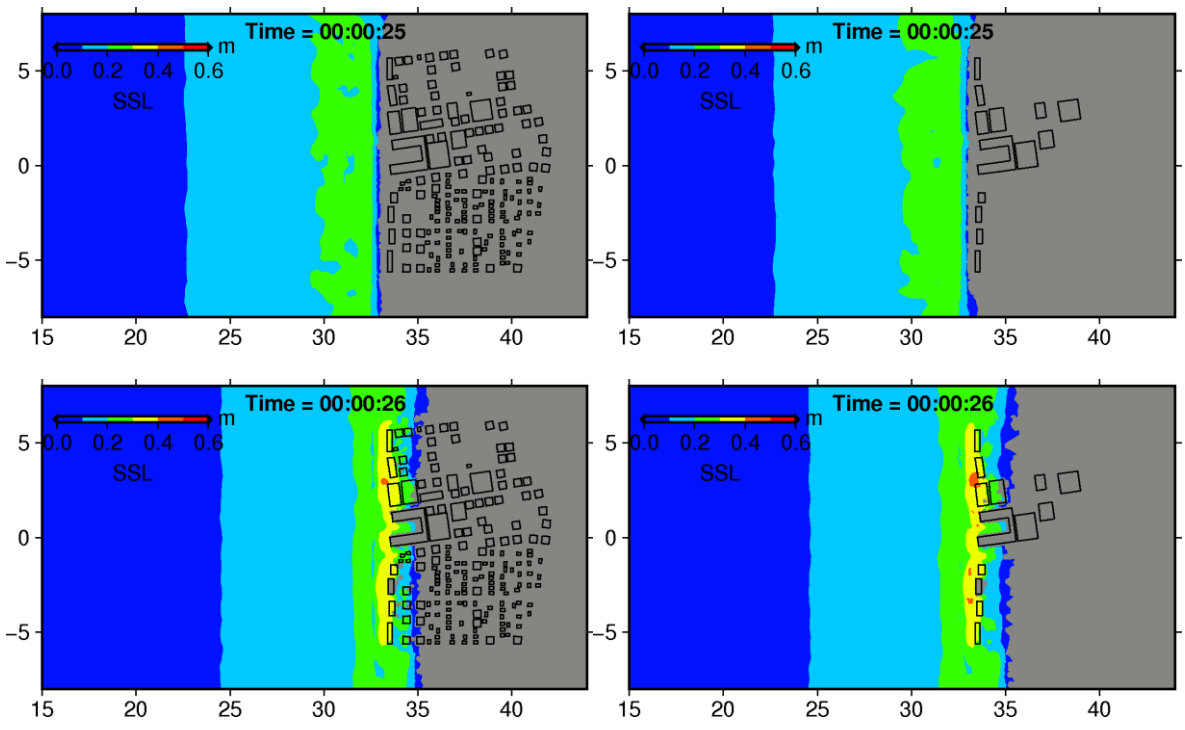

Figure 27 Spatial variation of surface elevation of resolved mesh system case (left) and concrete-resolved mesh system case (right) at 25-26 s.

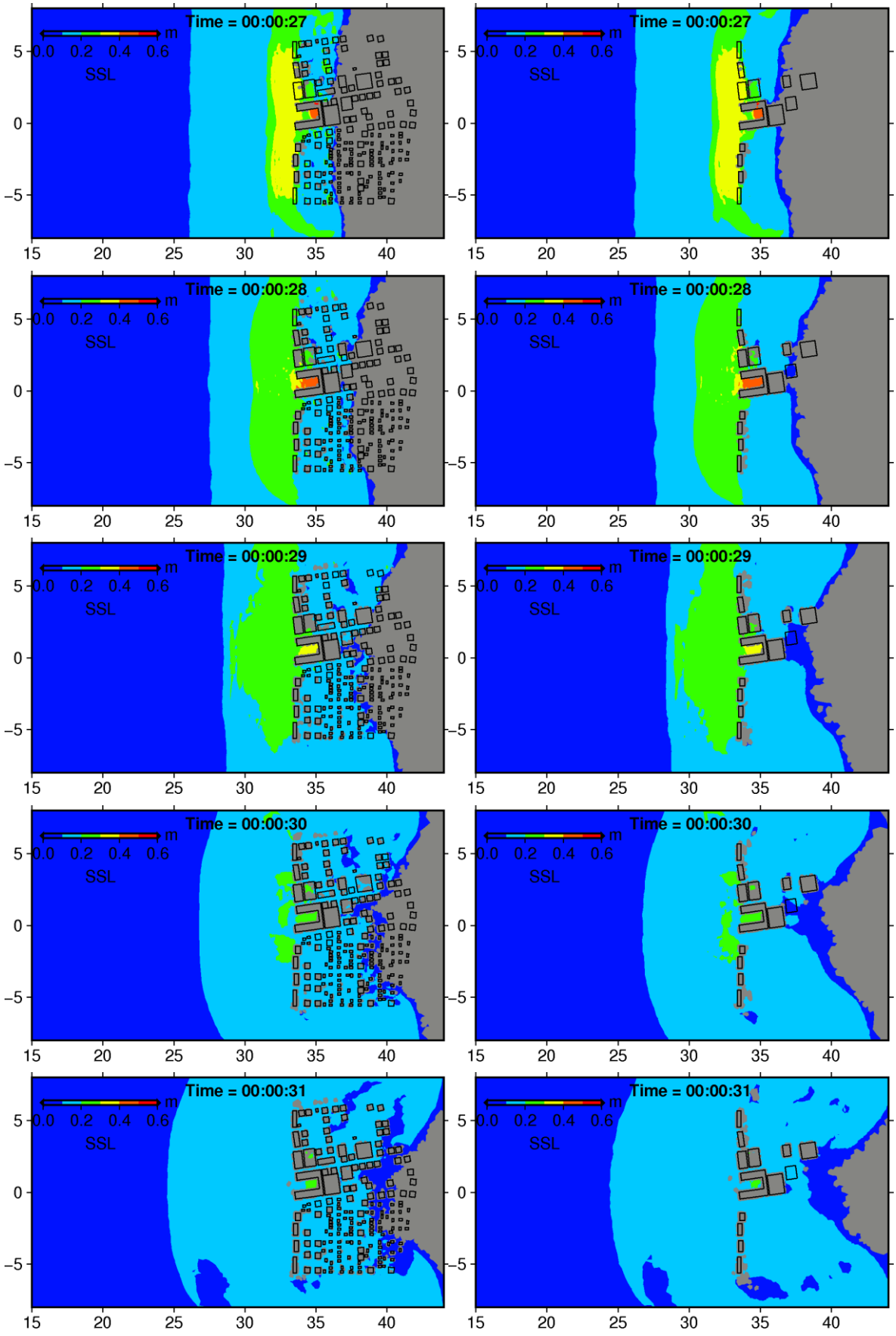

Figure 28 Spatial variation of surface elevation of resolved mesh case (left) and concrete-resolved mesh case (right) at 27-31 s.

Left figures show resolved mesh simulation results, which is considered as idealized simulation results while right figures show concrete-resolved mesh simulation results with the smallest grid size (0.15 m) which is considered as results of the proposed method. This comparison aims to see reproducibility of proposed method to idealized simulation results.

Figure 27 and Figure 28 show spatial variation of surface elevation at 25-31 s. The figures show that the initial wave started to enter inundation area with generally same behavior. After propagating from offshore side, at 26 s. wave reflection occurred due to existence of large hotels on the water front. Because these structures are resolved, wave reflection can be reproduced well by concrete-resolved mesh system. Same behavior of inundation are observed from two simulation results. However inundation pattern at wooden houses are different because the concrete-resolved mesh does not resolve those buildings but replace them with roughness coefficient.

4.3.4. Maximum surface elevation

Spatial variation of maximum surface elevation is discussed in this sub chapter.

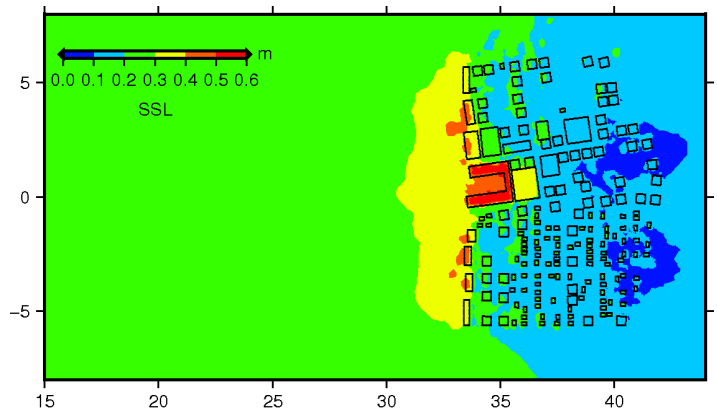

Figure 29 Maximum surface elevation for resolved mesh case.

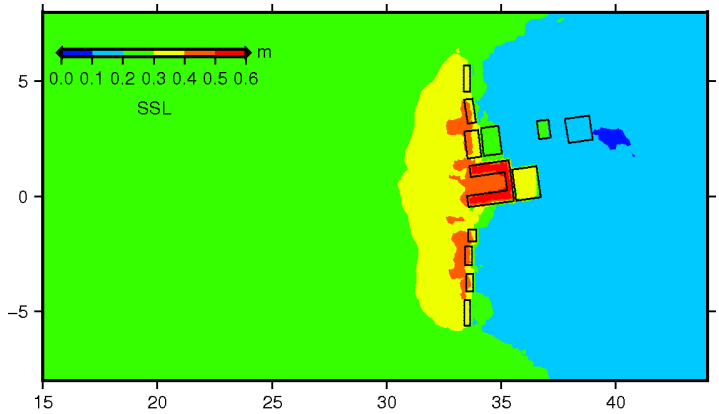

Figure 30 Maximum surface elevation for concrete-resolved mesh case.

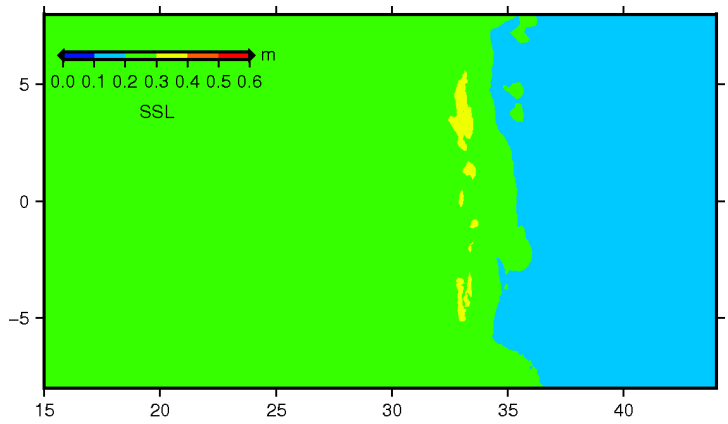

Figure 31 Maximum surface elevation for unresolved mesh case.

Figure 29-Figure 31 show maximum surface elevation results for case 1 (resolved mesh), case 2 (concrete-resolved mesh), and case 3 (unresolved mesh) simulations. Case 1 is considered as an idealized simulation of physical experiment as all buildings are resolved and building height data are given while case 2 is the proposed model and case 3 is typical method of roughness coefficient application. In the propagation area similar pattern of maximum surface elevation are observed in case 1, case 2, and case 3.

In the area close to the large hotels on the water front, higher maximum surface elevation than other area is observed in case 1. It is the effect of reflected wave from the large hotels. This condition is able to be reproduced by case 2 but could not be reproduced by case 3 because large hotels are not resolved in case 3.

In the inundation area, general magnitudes are similar for case 1, 2, and 3. However, low surface elevations around commercial buildings and wooden houses are observed at rear side of inundation area. This phenomena occurred due to existence of buildings at inundation area in case 1. The phenomena could not be reproduced by case 2 and 3 becaus.ommercial buildings and wooden houses are not resolved in case 2 and case 3.

4.3.5. Maximum velocity

Spatial variation of maximum velocity for case 1 (resolved mesh case with minimum grid size 0.05 m), case 2 (concrete-resolved mesh case with minimum grid size 0.15 m), and case 3 (unresolved mesh case with minimum grid size 0.15 m) are discussed in this s.tion.

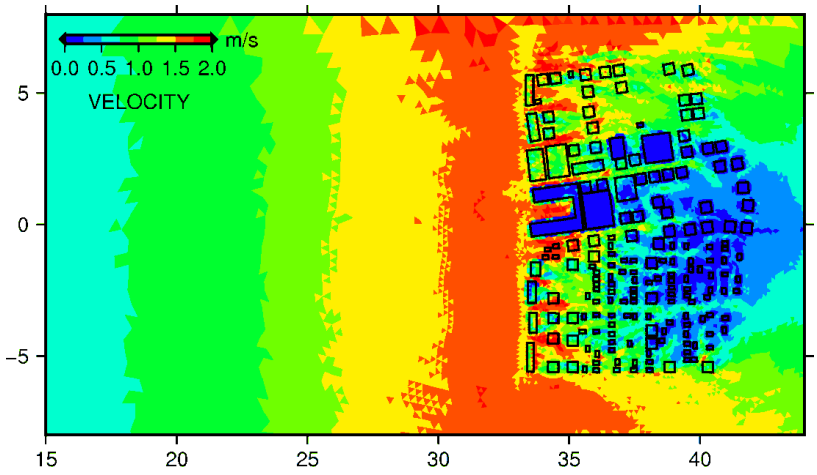

Figure 32 Maximum velocity for case 1, resolved mesh case.

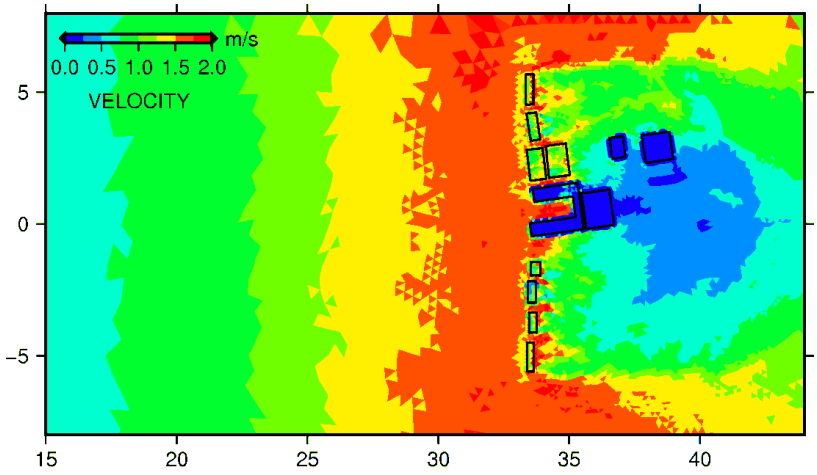

Figure 33 Maximum velocity for case 2, concrete-resolved mesh case.

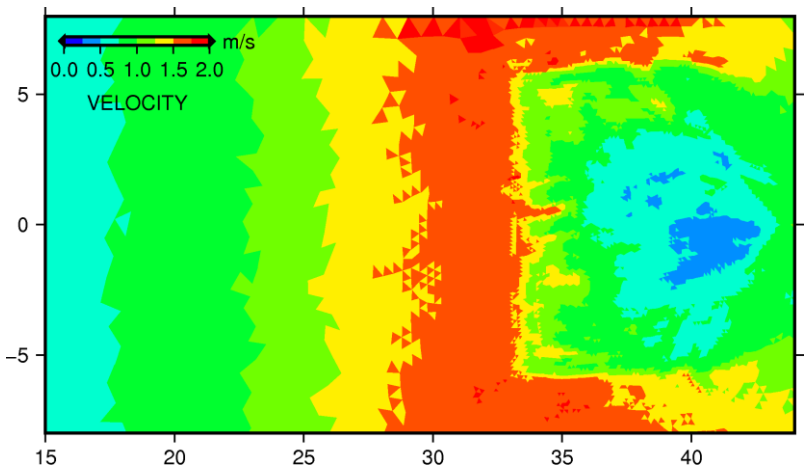

Figure 34 Maximum velocity for case 3, unresolved mesh case.

Figure 32-Figure 34 show maximum velocity for case 1 (resolved mesh), case 2 (concrete-resolved mesh), and case 3 (unresolved mesh). In the propagation area, maximum

velocity for case 1, case 2, and case 3 show relatively similar pattern. Local differences of maximum velocity pattern are observed. This phenomenon may be occurred due to the grid size differences. Case 1 which is considered as an idealized case ha 0.05 m minimum grid size while other two cases minimum grid size is 0.15 m.

In the inundation area, overall magnitude of maximum velocity are similar among all simulations. However, high velocity in the city street could not be reproduced well by case 2 and 3. Case 2 reproduced high velocity in the city street between hotels on the water front because those hotels are resolved in case 2. However, because all buildings are not resolved by case 3, high velocity in city streets could not be reproduce by case 3.

4.3.6. Comparison of inundation depth at wave gauges

Inundation depth at wave gauges for case 1 (resolved mesh case), case 2 (concrete-resolved mesh case) and case 3 (unresolved mesh case) are discussed in this sub chapter. In the first section, inundation depth at offshore wave gauges are discussed.

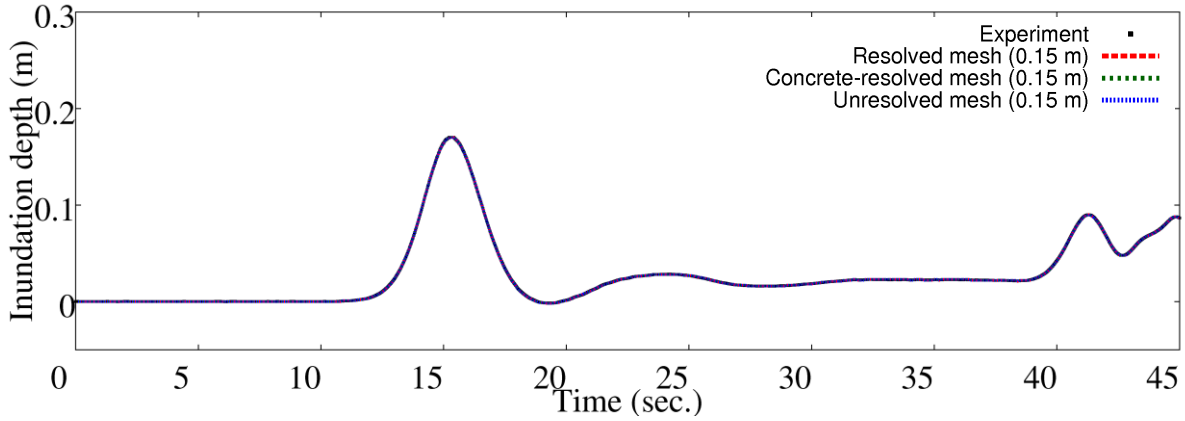

Figure 35 Inundation depth at WG1.

In this study, open boundary is located at WG1. Time series of experimental surface elevation is given at this point. Figure 35 shows that all simulations reproduced surface elevation at WG1 well. Initial wave is shown at 13-19 s. This wave was generated by wavemaker in the experimental case. At 40-45 s. reflected wave from inundation area is observed.

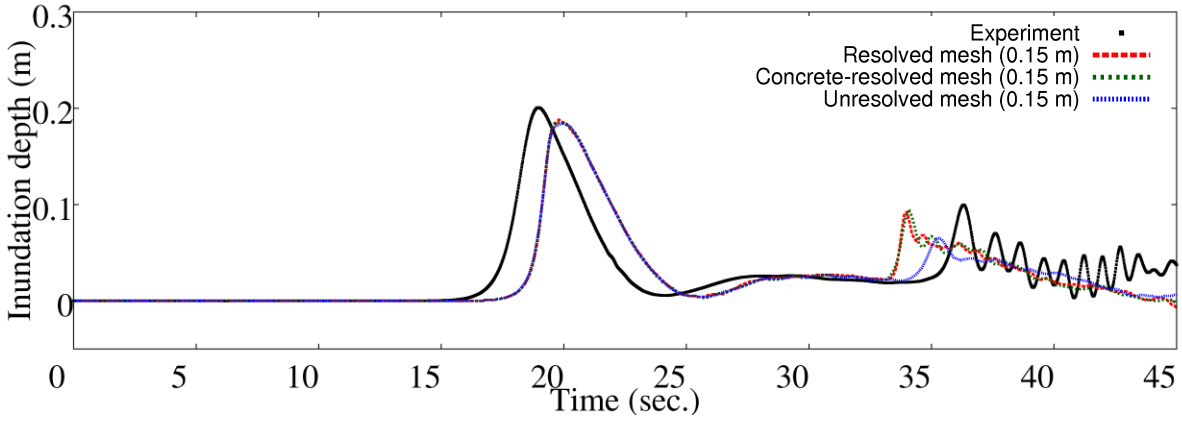

Figure 36 Inundation depth at WG3.

Figure 36 shows comparison of inundation depth at WG3. All simulation results show different phase to the experimental results. This behavior may be occurred due to absence of velocity as open boundary condition. Thus, simulated waves flow slower than the experimental results. At 35 s. about 0.1 m inundation depth is detected due to reflected wave from shoreline and buildings.

In this section, inundation depth at city streets are discussed. Measurement locations are divided into four lines: A, B, C and D. Line A is located on a street parallel to the inundation flow direction while line B and C are located on streets inclined to the flow direction.

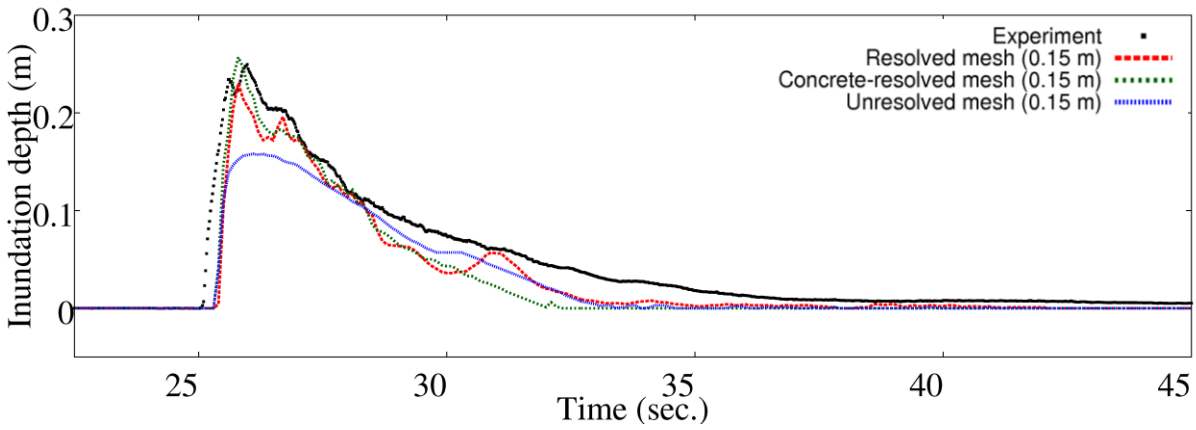

Figure 37 Inundation depth at A1.

Figure 37 shows inundation depth at A1 for case 1 (resolved mesh with 0.15 m grid size), case 2 (concrete-resolved mesh with 0.15 m grid size) and case 3 (unresolved mesh with 0.15 m grid size). Case 2 slightly overestimated the experimental results while case 1 and 3 underestimated the experimental results. Case 2 reproduced experimental results better than other simulations. The possible reason is the roughness coefficient values in case 2

which are set uniform to 0.001 while roughness coefficient in case 1 is based on the law of the wall. Thus, although the minimum value in case 1 is set to 0.001, the higher friction may be determined during the simulation based on the depth. Thus, inundation depth simulated by case 1 is lower than those simulated by case 2.

If inundation depth at point A1 (Figure 37) is compared to results at point B1 (Figure 38), and point C1 (Figure 39), it is observed that inundation depth at A1 is higher than those at point B1 and C1.The possible reason is differences in wave gauge locations. Point A1 is located on a city street parallel to the flow direction while point B1 and C1 are located on streets inclined to the flow direction.

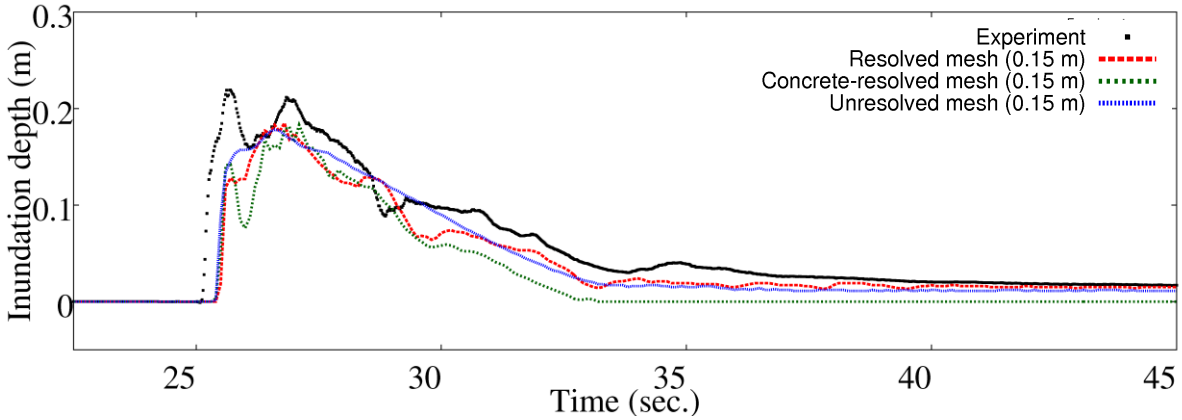

Figure 38 Inundation depth at B1.

Figure 38 shows comparison of inundation depth at B1. Different from A1, all simulation results at B1 underestimated experimental results. The possible reason is the location of B1 which is not parallel to the inundation direction. Thus, wave did not flow to the city street directly.

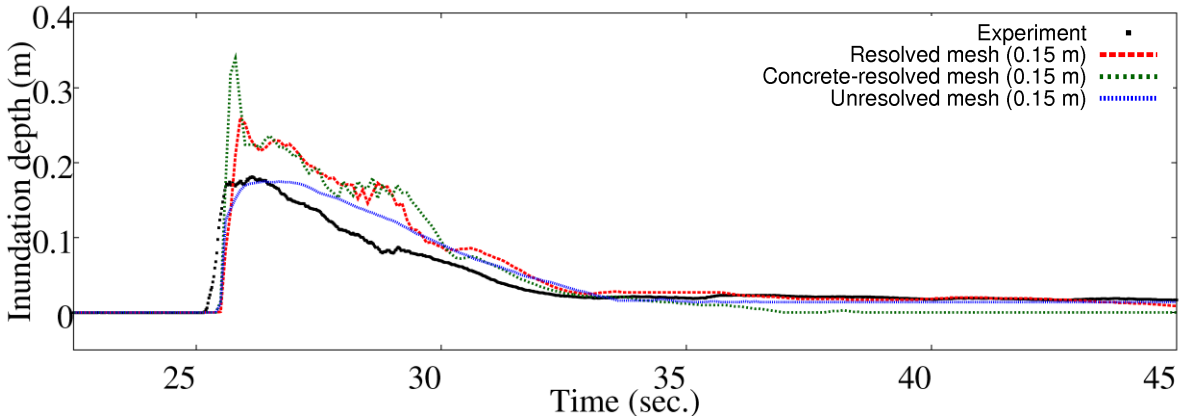

Figure 39 Inundation depth at C1.

Different from A1, simulation results overestimated experimental results at C1 (Figure 39). Overestimation may be occurred due to the interaction between initial waves with the reflected waves from buildings around C1 at numerical simulations. Case 3 (unresolved mesh case) shows about 0.18 m inundation depth at A1 and C1 due to lack of resolved buildings around the wave gauge. The initial wave does not reflected to any building. Thus, similar simulation results of case 3 are observed at A1 and C1.

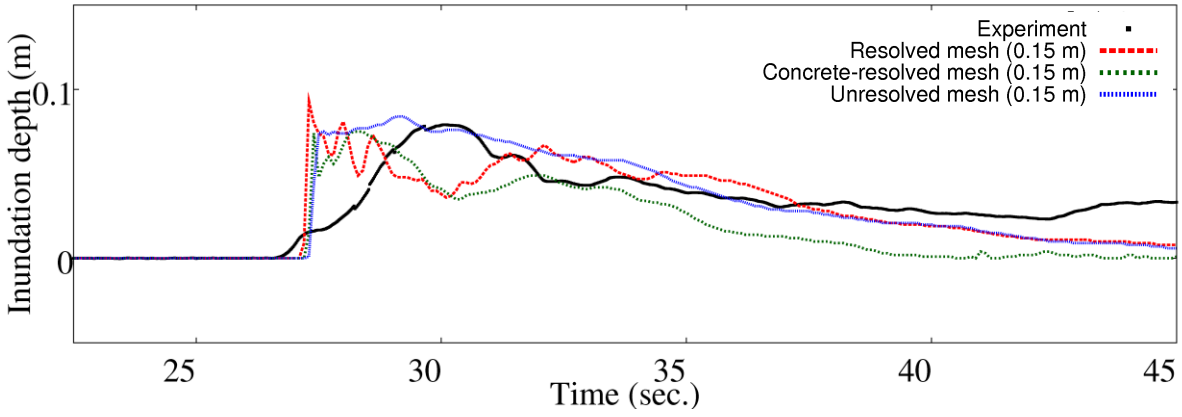

Figure 40 Inundation depth at D2.

Figure 40 shows inundation depth at D2. Wave gauge D2 is located behind the buildings and therefore effectiveness of roughness coefficient calculation can be observed from the results. Although buildings are not resolved, case 2 (concrete-resolved mesh case) and case 3 (unresolved mesh case) reproduced the experimental results quite well. However, different behavior between experiment and simulation results are observed at 27-30 s. Inundation depth of experimental results started to increase slowly while inundation depth of simulation results increased suddenly and decreased faster than that of experimental results. This behavior may be occurred due to the low friction factor of numerical simulations.

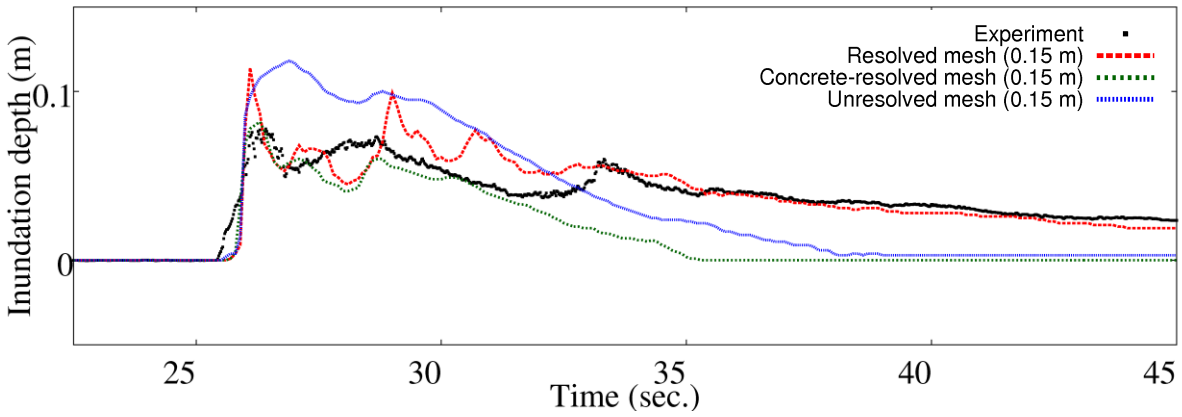

Figure 41 Inundation depth at A3.

Figure 41 shows inundation depth at A3. Case 2 (concrete-resolved mesh case) reproduces experimental results well while case 1 (resolved mesh case) and case 3 (unresolved mesh case) overestimated the experimental results. Overestimation by case 1 (resolved mesh case) may be occurred due to the wave reflection from surrounding buildings while overestimation by case 3 (unresolved mesh case) may be occurred due to the minimum friction coefficient when there is no building, where C=0.001).

Resolved mesh results show good agreement with experimental results because all buildings are resolved. However, concrete-resolved mesh results underestimated the experimental results after 33 s. and unresolved mesh results underestimated the experimental results after 32 s. The probable cause of underestimation is the wave interaction due to resolved buildings. When many buildings are resolved, wave height tends to decrease slowly and therefore resolved mesh results show the best agreement with the experimental results. However, when several buildings are not resolved, wave height tends to decrease rapidly. Thus, concrete-resolved mesh results underestimated the experimental results after 33 s. and unresolved mesh results underestimated the experimental results faster, after 32 s.

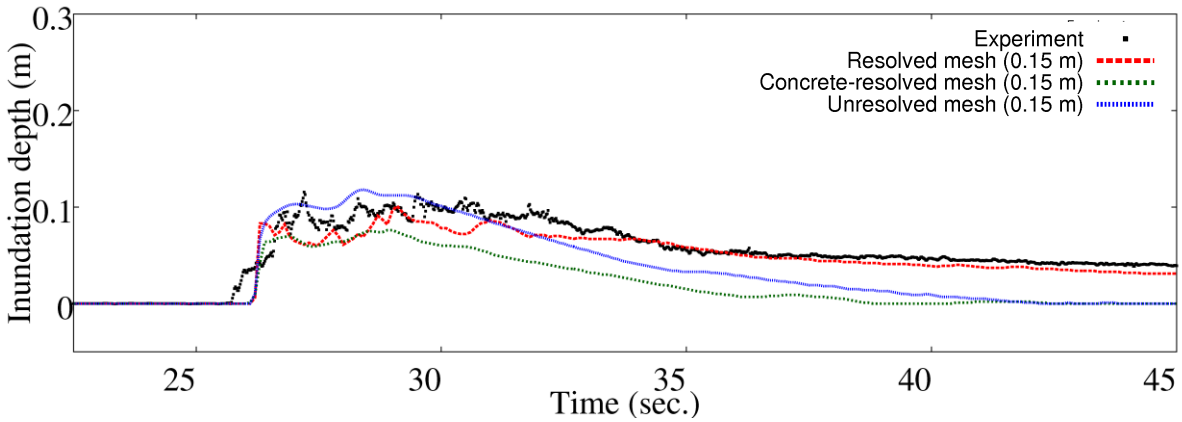

Figure 42 Inundation depth at A4.

Figure 42 shows inundation depth at A4. All simulations reproduced experimental results tendency well. Case 3 (unresolved mesh case) slightly overestimated the experimental results as minimum friction coefficient was set to 0.001 and no resolved buildings in the mesh system. The spike shaped wave are simulated by case 1 (resolved mesh case). The possible reason is the wave interaction with buildings.

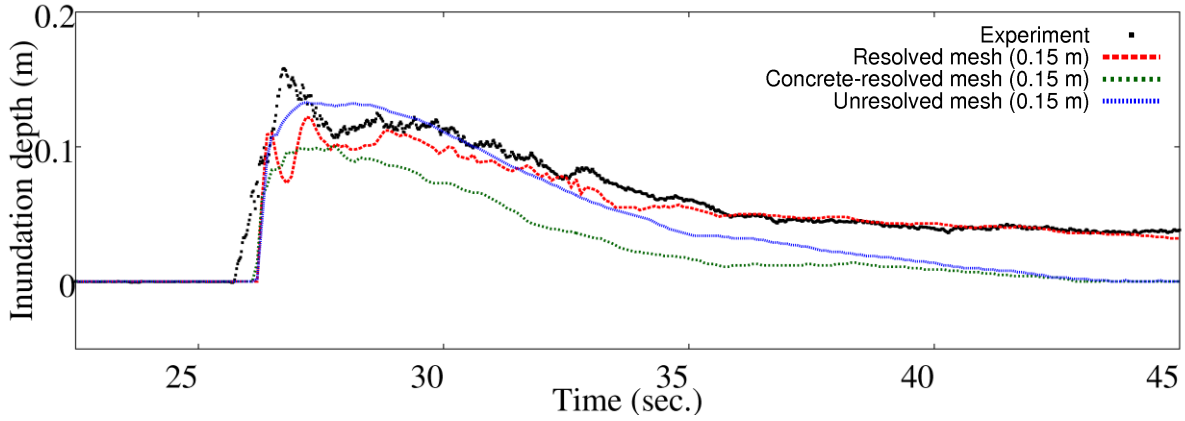

Figure 43 Inundation depth at B4.

Figure 43 shows inundation depth at B4. Case 1 (resolved mesh case) reproduced the experimental results well including the initial wave although there are phase differences between experimental and simulation results. Case 2 (concrete-resolved mesh case) underestimated the experimental results as the left side of area of wave gauge B4 is resolved but the right side area is not resolved.

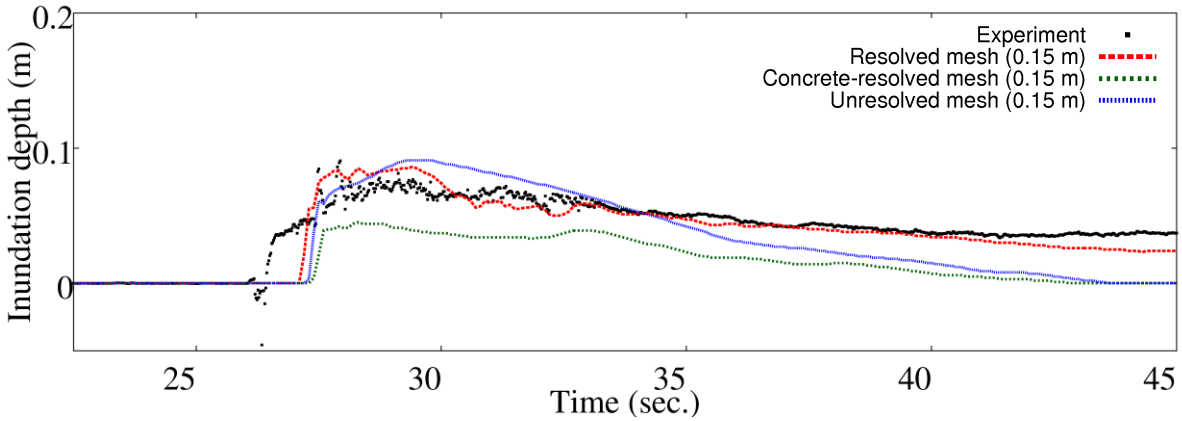

Figure 44 Inundation depth at B6.

Figure 44 shows inundation depth at B6. Case 1 (resolved mesh case) reproduced experimental results well while case 3 (unresolved mesh case) slightly overestimated the experimental results and case 2 (concrete-resolved mesh case) underestimated the experimental results. Case 2 underestimated inundation depth in most of wave gauges located in the rear side of inundation area. This phenomena may be occurred due to lack of resolved buildings in the rear side of inundation area of case 2. Case 3 overestimated the experimental results because the coming wave did not interact with any resolved buildings so the inundation depth kept high.

4.3.7. Comparison of cross shore velocity at wave gauges

Cross shore velocity at wave gauges are discussed in this section. As shown in Figure 32-Figure 34, maximum velocity of case 2 (concrete-resolved mesh case) and case 3 (unresolved mesh case) at city streets are lower than maximum velocity of case 1 due to absence of resolved buildings. Thus, underestimation of cross shore velocity of case 2 and case 3 at wave gauges can be understood.

In this sub chapter comparison of cross shore velocity at wave gauges are shown for case 1 (resolved mesh case with 0.05 m grid size), case 2 (concrete-resolved mesh case with 0.15 m grid size) and case 3 (unresolved mesh case with 0.15 m grid size). Grid size represents minimum inundation area grid size while propagation area grid size are set larger (up to 1 m). Different from those shown in previous sub chapter, in this sub chapter smaller grid size (0.05 m) is shown for case 1 (resolved mesh case) since cross shore velocity is resolved better by 0.05 m grid size than by larger grid size (0.15 m).

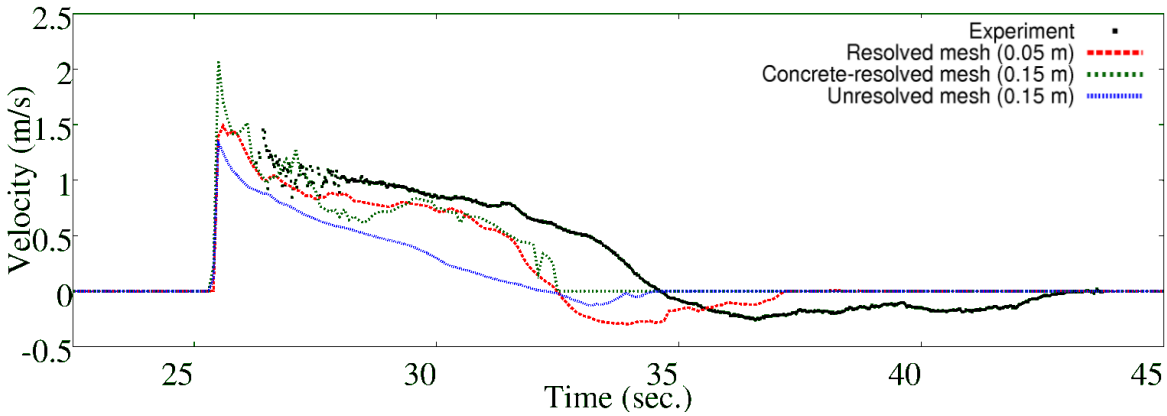

Figure 45 Cross shore velocity at A1.

Figure 45 shows cross shore velocity at A1. At 26-28 s., no experimental results are available. After 28 s., all cases underestimated the experimental results. Case 1 (resolved mesh case) underestimated the experimental results; however, general trends are reproduced well. Case 1 also reproduced the experimental velocity at 37-39 s. Case 2 (concrete-resolved mesh case) and case 3 (unresolved mesh case) reproduced general trend of experimental results. Underestimation by all cases may be caused by absence of velocity as open boundary condition in this study.

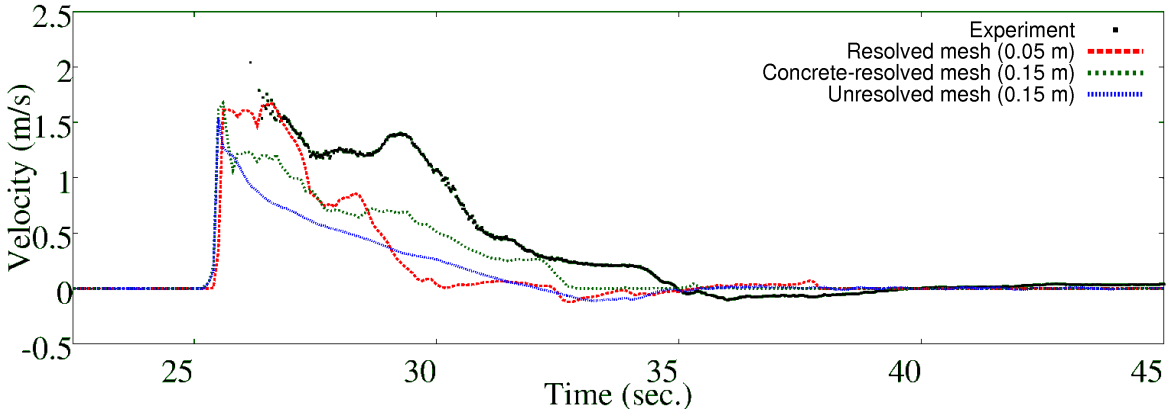

Figure 46 Cross shore velocity at B1.

Figure 46 shows cross shore velocity at B1. Case 1 (resolved mesh case) reproduced the experimental results well at 26-27 s.; however, all simulations underestimated the experimental results after 27 s. The possible reason is that location of line B is inclined, approximately 10°, from the primary inundation flow direction. Thus, wave does not inundated B1 directly but may be interacted with buildings around before inundated B1.

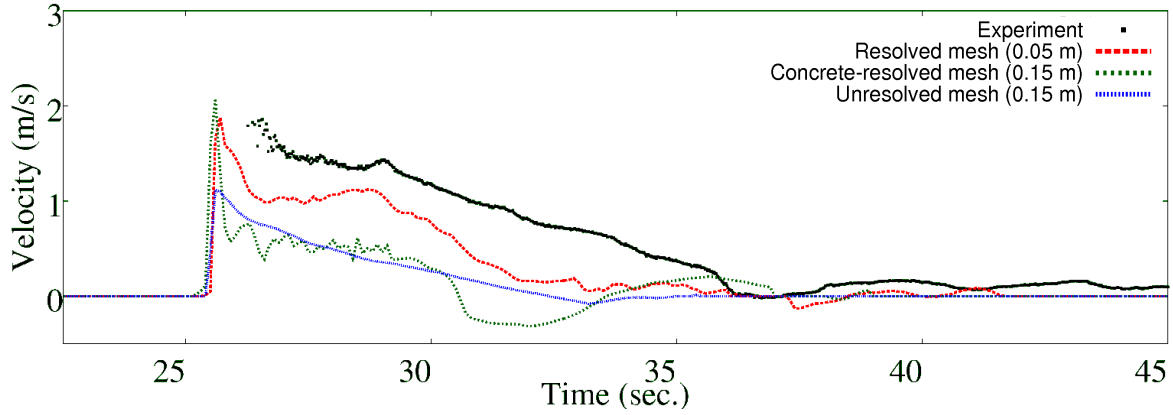

Figure 47 Cross shore velocity at C1.

Figure 47 shows cross shore velocity at C1. General tendencies of experimental results are reproduced by simulation results. However, all simulation results underestimated experimental results. This underestimation may be occurred due to absence of velocity as boundary condition. In addition, case 3 (unresolved mesh case) underestimated the experimental results because buildings are not resolved in case 3.

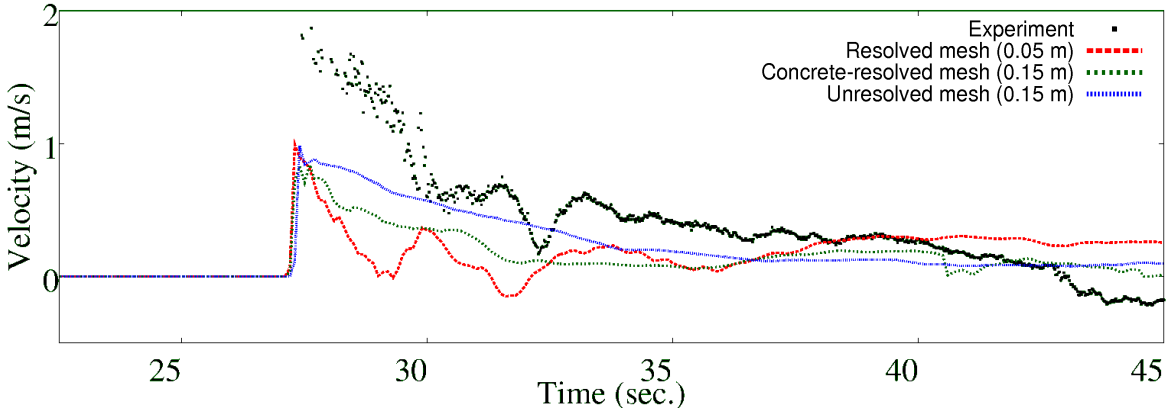

Figure 48 Cross shore velocity at D2.

Figure 48 shows cross shore velocity at D2. Between 27-38 s., all simulations underestimated the experimental results. The possible reason is that simulations could not reproduced waves between two buildings in front of D2. This phenomena may be occurred due to absence of velocity as boundary condition in numerical simulations.

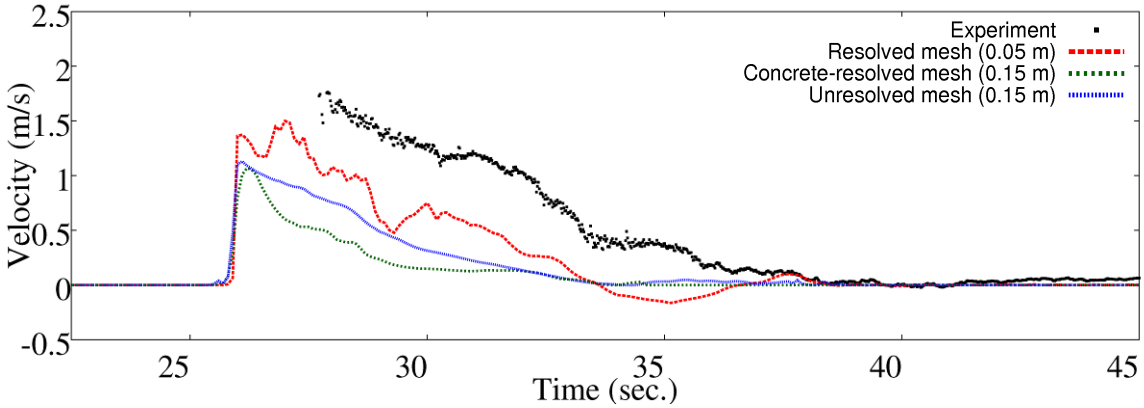

Figure 49 Cross shore velocity at A3.

Figure 49 shows cross shore velocity at A3. The same phenomena as other locations occurred at A3. All simulations underestimated the experimental results. However case 1 (resolved mesh case) reproduced the experimental results higher than other two simulations because all buildings are resolved by case 1. Thus high velocity between buildings are reproduced by case 1. Other two simulations could not reproduce high velocity between buildings because buildings around A3 were not resolved by case 2 (concrete-resolved mesh case) and case 3 (unresolved mesh case).

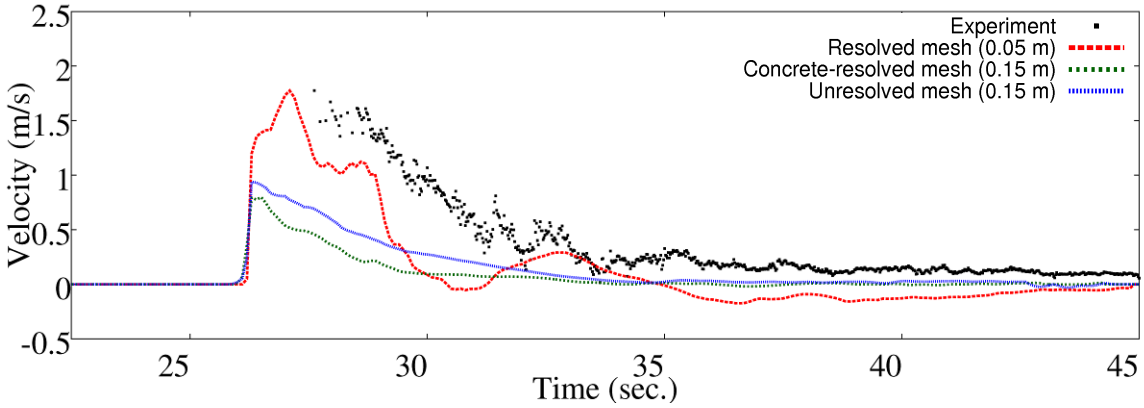

Figure 50 Cross shore velocity at A4.

Figure 50 shows cross shore velocity at A4. Case 1 (resolved mesh case) reproduced simulation results higher than other two simulations because all buildings are resolved. Buildings around A4 are not resolved in case 2 and 3; therefore, those simulations underestimated the experimental results. Case 2 (concrete-resolved mesh case) shows lower velocity than those of case 3 (unresolved mesh case) at 27-34 s. This behavior may be occurred due to existence of resolved concrete buildings in case 2 while no buildings are resolved in case 3.

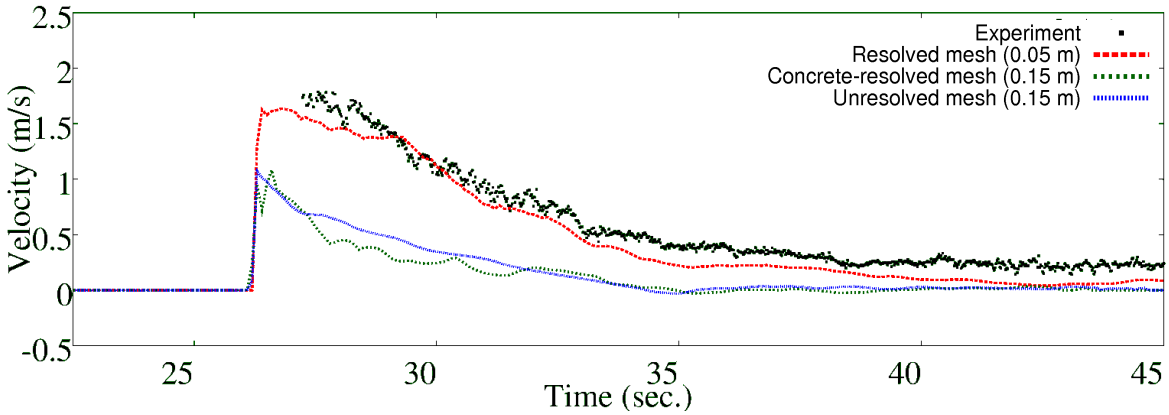

Figure 51 Cross shore velocity at B4.

Figure 51 shows cross shore velocity at B4. Case 2 (concrete-resolved mesh case) and case 3 (unresolved mesh case) underestimated the experimental results because buildings around A4 were not resolved. Case 1 (resolved mesh case) well reproduced cross shore velocity because all buildings are resolved. At B4, case 2 and case 3 show quite similar behavior while case 1 show different behavior from other two cases. This phenomena may be occurred due minimum grid size differences between case 1 (0.05 m) and other two cases (0.15 m).

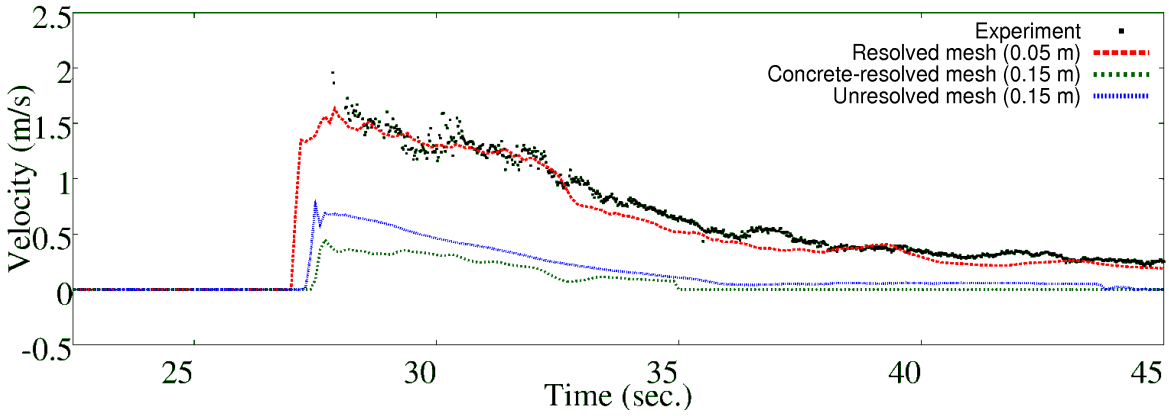

Figure 52 Cross shore velocity at B6.

Figure 52 shows cross shore velocity at B6. The same condition as cross shore velocity at B4 developed at B6. Case 1 (resolved mesh case) reproduced the experimental results well because all buildings are resolved while case 2 (concrete-resolved mesh case) and 3 (unresolved mesh case) underestimated the experimental results because buildings around B6 were not resolved in case 2 and 3. This phenomena may also be occurred due minimum grid size differences between case 1 (0.05 m) and other two cases (0.15 m).

4.3.8. Numerical sensitivity test of grid sizes

In this sub chapter, numerical sensitivity test of grid sizes are discussed. Two types of results are shown: inundation depth at wave gauges and maximum inundation depth at wave gauges along line B.

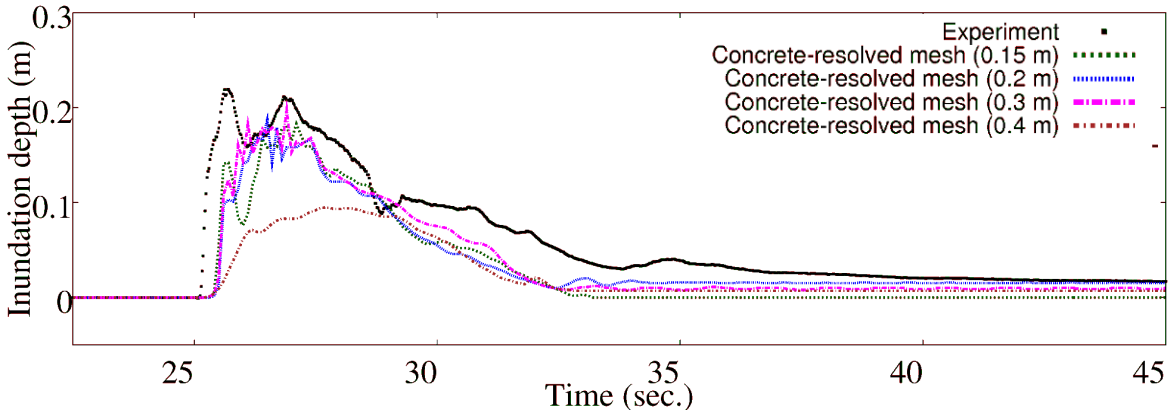

Figure 53 Inundation depth at B1 for concrete-resolved mesh simulation results.

Figure 53 shows comparison of inundation depth at B1 for concrete-resolved mesh simulation results. Results with grid size 0.15 m, 0.2 m, and 0.3 m show relatively similar trends and magnitudes, while result with 0.4 m grid size underestimated the experimental results more than other cases.

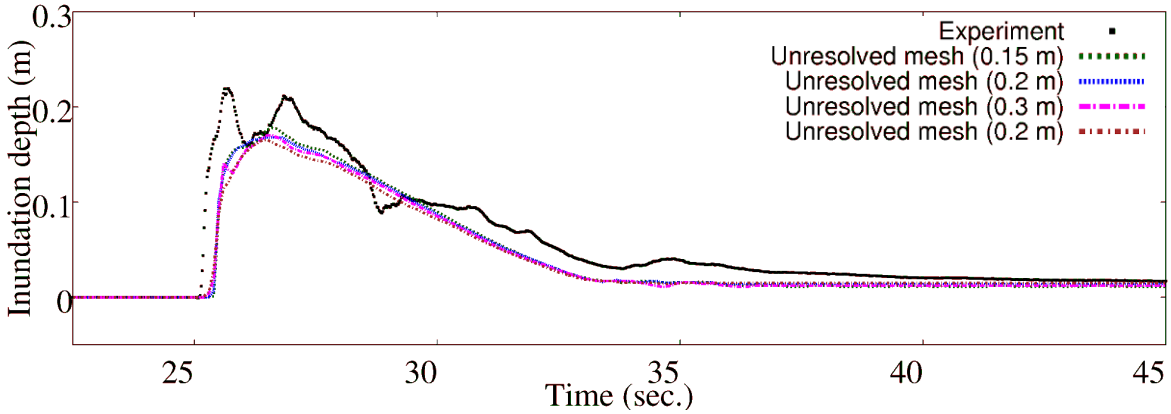

Figure 54 Inundation depth at B1 for unresolved mesh simulation results.

Figure 54 shows comparison of inundation depth at B1 for concrete-resolved mesh simulation results. All simulations show relatively same trends and magnitudes. The possible cause is that no buildings were resolved in those simulations. Thus no spike-shaped waves are observed in the simulation results and no significant differences between all simulations although minimum grid sizes are different each other.

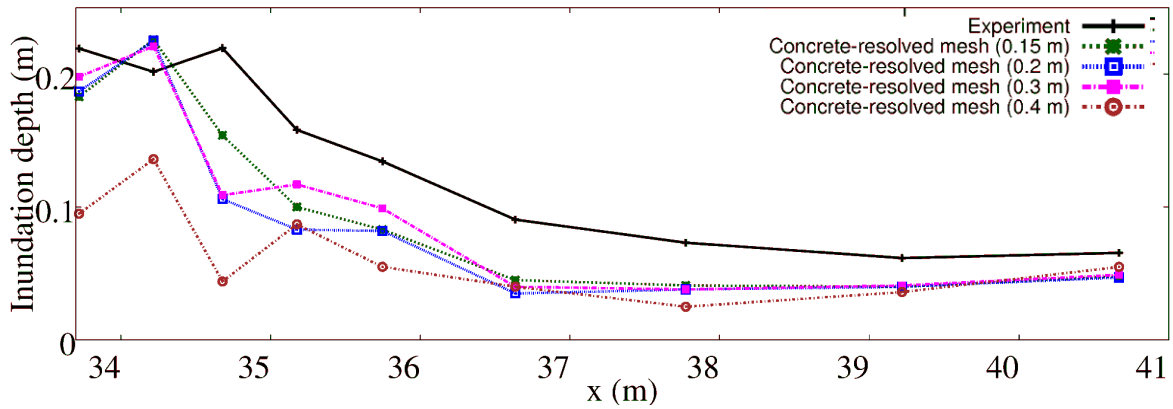

Figure 55 Maximum inundation depth at line B for concrete-resolved mesh simulation results.

Figure 55 shows maximum inundation depth at line B for concrete-resolved mesh simulation results. Each node shows maximum inundation depth at B1 until B9 depends on

the location from the wavemaker. Concrete-resolved mesh simulations results with 0.15 m, 0.2 m and 0.3 m grid size show relatively same trend of maximum inundation depth until 36 m, while simulation results with 0.4 m grid size show different trend from other cases.

Underestimation of simulation results compared to the experimental results are observed because the compared values are maximum inundation depth. In experimental results, maximum inundation depth are calculated from initial and reflection wave at the wave gauges while in concrete-resolved mesh cases, reflection wave could not be calculated at the area where buildings are not resolved. Thus, maximum inundation depth values are smaller than those of experimental results. Moreover, existence of resolved buildings in the front side of inundation area cause energy dissipation and hence inundation depths at wave gauges located at middle and rear side of inundation area become lower.

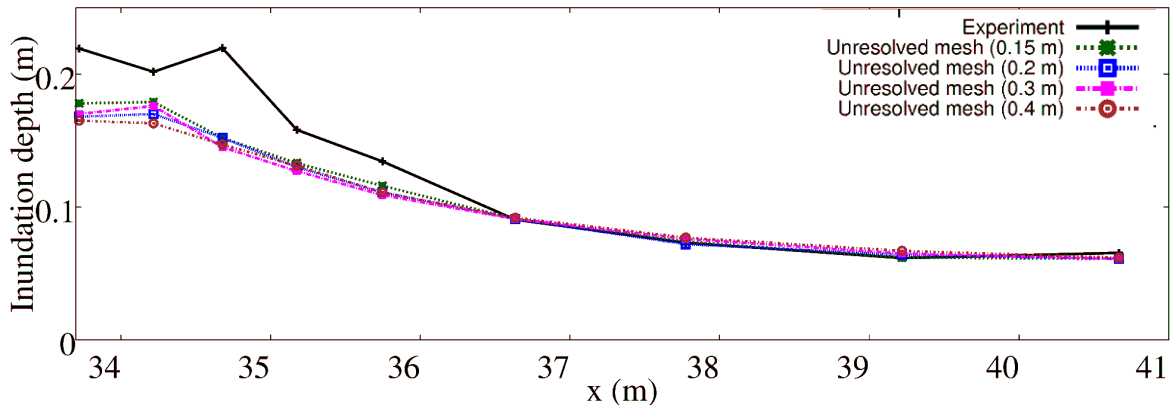

Figure 56 Maximum inundation depth at line B for unresolved mesh simulation results.

Figure 56 shows maximum inundation depth at line B for unresolved mesh simulation results. The experimental results of maximum inundation depth are reproduced well because no buildings are resolved in those cases. Thus, inundation depth remained high from the front side of inundation area until the rear side of inundation area. All simulations show similar trends. The possible cause is absence of resolved buildings in all simulations. This figure shows that grid size does not sensitive for unresolved mesh simulation results.

4.3.9. Numerical sensitivity test of minimum friction factors

Numerical sensitivity test of minimum friction factors are discussed in this sub chapter. Two minimum friction factors were tested: 0.001 and 0.005. The friction factors were given to the non-constructed area while in constructed area Imai et al. (2013) equation

was used.

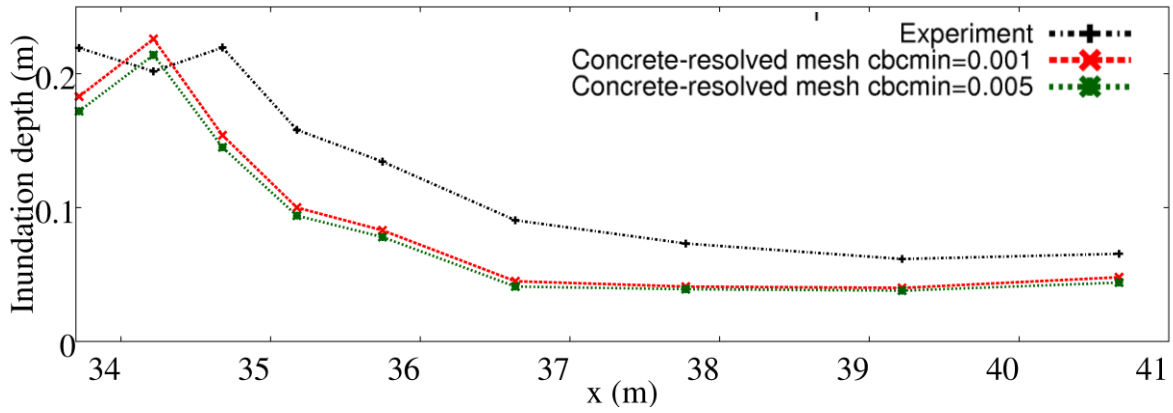

Figure 57 Maximum inundation depth at line B with minimum grid size=0.15 m.

Figure 57 shows comparison of maximum inundation depth at line B for simulation with minimum grid size 0.15 m. The figure shows that there are slight differences between simulation with minimum friction factor 0.001 and 0.005. As expected, simulations with lower friction factor shows higher inundation depth than simulations with higher friction factor. The deeper location to inundation depth, the smaller differences between both results. This behavior may be occurred due to the friction factor setting. Minimum friction factor was set to the non-constructed area. Thus the area close to shoreline are affected by this minimum friction factors more than other inundation area because constructed area are mainly located in those area.

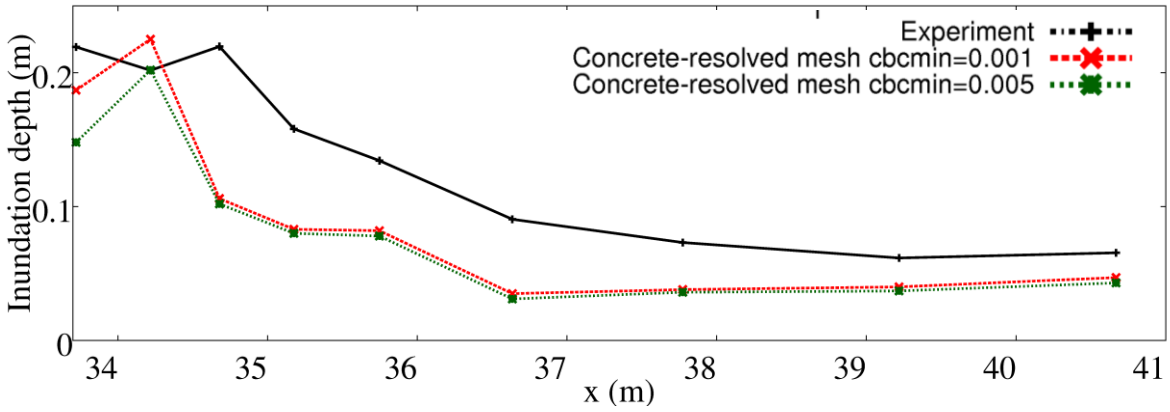

Figure 58 Maximum inundation depth at line B with minimum grid size=0.2 m.

Figure 58 shows comparison of maximum inundation depth at line B for simulations with minimum grid size 0.2 m. There is larger differences in inundation depth close to the shoreline (x less than 35 m) than other inundation area. The possible cause is energy dissipation. The deeper location of wave gauge from the shoreline, the higher energy is

dissipated. Thus, the differences between both simulations in rear side of inundation area are less than the front side of inundation area.

4.3.10. Statistical analysis of numerical simulations accuracy

In order to find the optimize grid size for numerical simulations, accuracy of numerical simulations are necessary to be calculated. In this sub chapter, normalized root mean square (NRMSE) values are calculated as follow

$$NRMSE = \frac{\sqrt{\frac{1}{n}\sum_{i=1}^{n}\left(\hat{\zeta}_i - \zeta_i\right)^2}}{\zeta_{\max} - \zeta_{\min}} \tag{46}$$

where $\hat{\zeta}_i$ is surface elevation of numerical model, ζ_i is surface elevations of physical experiment data, $\zeta_{\max}$ and $\zeta_{\min}$ are the maximum and minimum of physical experiment surface elevations, n is number of data.

After numerical simulations, it is found that simulation results at A1, C1, C2, and C6 could not be reproduced well by several simulations due to large grid sizes around wave gauges. The large grid size caused inappropriate setting of topography data. Thus, in this calculation, NRMSE are calculated from 27 wave gauge locations for 45 minutes (450 time steps) simulation time (n = 27 wave gauges x 450 time steps = 12150).

Calculated NRMSE values are presented in the following figure.

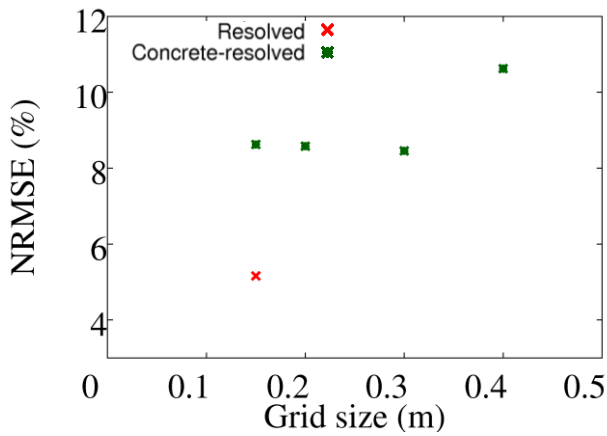

Figure 59 NRMSE of simulated surface elevations compared to physical experimental results.

Figure 59 shows NRMSE values for resolved mesh case and concrete-resolved simulations. Error value of resolved mesh case is the smallest among all values. Error values for concrete-resolved mesh case for grid size 0.15 m, 0.2 m, 0.3 m, and 0.4 m are 8.6%, 8.6%, 8.5%, and 10.6% respectively. Error values for concrete-resolved mesh case grid size 0.15 m, 0.2 m, and 0.3 m are less than 10% while error value for grid size 0.4 m is larger than 10%.

According to Synolakis et al. (2007), standard accuracy for inundation models with respect to laboratory data is 10%. Error value for grid size 0.4 m is larger than 10% and therefore it does not meet the standard accuracy. The largest grid size which meets the standard accuracy is 0.3 m.

In this study, optimum grid size is considered as 0.3 m which is two times of the typical house size in the experiment. The reasons are as follow:

1. NRMSE value of the proposed grid size is less than 10% (see Figure 59) which meets the standard accuracy for inundation models with respect to laboratory data.
2. The proposed grid size reproduced maximum inundation depth at line B (see Figure 55) better than those of reproduced by larger grid size.
3. Number of nodes and elements used in the proposed simulation is 3.3 times smaller than those necessary for the idealized case simulation (see Table 5 no.1 for idealized simulation and no.6 for the proposed simulation)
4. The proposed simulation system is 61.5% faster than the idealized simulation (see Table 5).

4.3.11. Comparison between two boundary conditions

In sub chapter 4.3.10, statistical analysis is performed for numerical simulation results compared to experimental results conducted by Park et al. (2013). In this sub chapter, statistical analysis is carried out for concrete-resolved mesh case simulation results compared to resolved mesh case simulation results which is considered as idealized case. Two boundary conditions are compared for simulations: maximum surface elevation 0.22 m (original case) and 0.6 m (modified case).

Four simulations are conducted: resolved mesh case (idealized case), concrete-

resolved mesh cases with smallest grid sizes ranges from 0.15 m, 0.2 m, 0.3 m and 0.4 m. Each simulation is executed for two maximum surface elevations: 0.22 m and 0.6 m. Because in modified cases no experimental results are available, NRMSE values of both cases are evaluated from concrete-resolved mesh case values and resolved mesh case values. Resolved mesh case values are taken as idealized values to calculate NRMSE.

Calculated NRMSE values are presented in below figures.

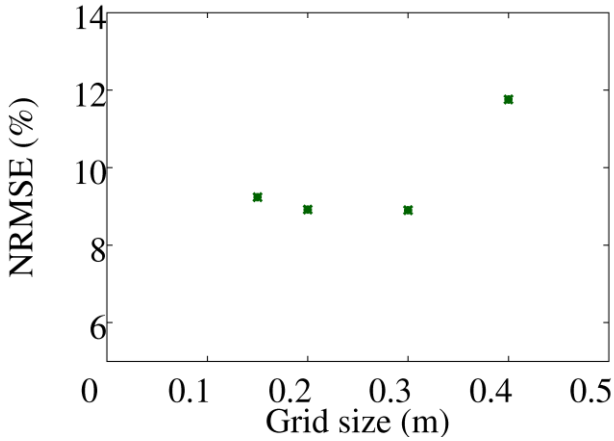

Figure 60 NRMSE of simulated surface elevation results from concrete-resolved mesh case compared to resolved mesh case results for initial surface elevation = 0.22 m.

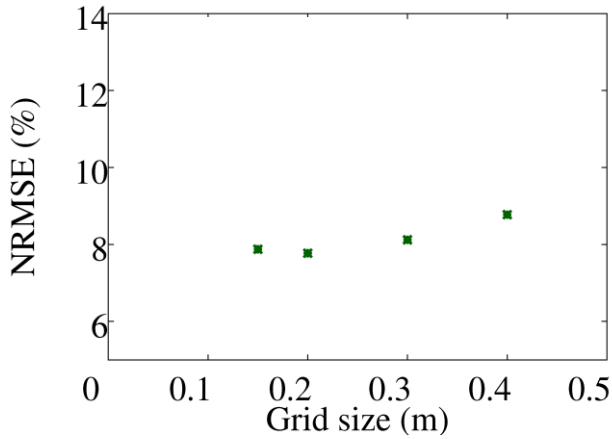

Figure 61 NRMSE of simulated surface elevation results from concrete-resolved mesh case compared to resolved mesh case results for initial surface elevation = 0.6.

Above figures show NRMSE values for two boundary conditions: maximum surface elevation 0.22 m and 0.6 m. Difference values are observed for simulation with grid size 0.4 m. When simulations are conducted utilizing smaller maximum surface elevation (0.22 m), NRMSE value of simulation using grid size 0.4 m is much higher than the same simulation

with higher initial surface elevation height (0.6 m). This comparison shows that optimum grid size proposed in this study which is two times of house size (0.3 m) is applicable when maximum surface elevation height is quite low (0.22 m). However, if maximum surface elevation is higher e.g. 0.6 m as shown in above figure, optimum grid size may be larger than the proposed size.

4.3.12. Numerical simulations of new arrangement

New arrangement of buildings are developed to see performance of proposed model to idealized model with different structures arrangement. Boundary conditions and simulation domains are the same as experimental cases in this sub chapter while the buildings arrangement is shown in Figure 62. In original arrangement, concrete buildings are located in the front side of inundation area while in the new arrangement concrete buildings (red blocks in Figure 62) are mainly located in the rear side of inundation area.

Six cases are simulated with three different mesh types and as shown in the following table.

Table 8 Simulation setup of new arrangement

No	Mesh Type	Min. grid size	Elements	Nodes	BF condition	Simulation time (HA8000)
1	Resolved	0.05 m	101,161	50,664	Original	> 62 min.
2	Concrete-resolved	0.15 m	15,073	7,623	Modified	9 min.
3	Unresolved	0.15 m	21,681	10,927	Modified	12 min.
4	Concrete-resolved	0.2 m	11,495	5,834	Modified	7 min.
5	Concrete-resolved	0.3 m	8,077	4,125	Modified	5 min.
6	Concrete-resolved	0.4 m	6,385	3,279	Modified	4 min.

Figure 62 Building arrangement of new arrangement.

Red blocks are considered as concrete structures while blue blocks are considered as wooden houses.

Maximum surface elevation of case 1 (resolved mesh case), case 2 (concrete resolved mesh case), and case 3 (unresolved mesh case) are shown below.

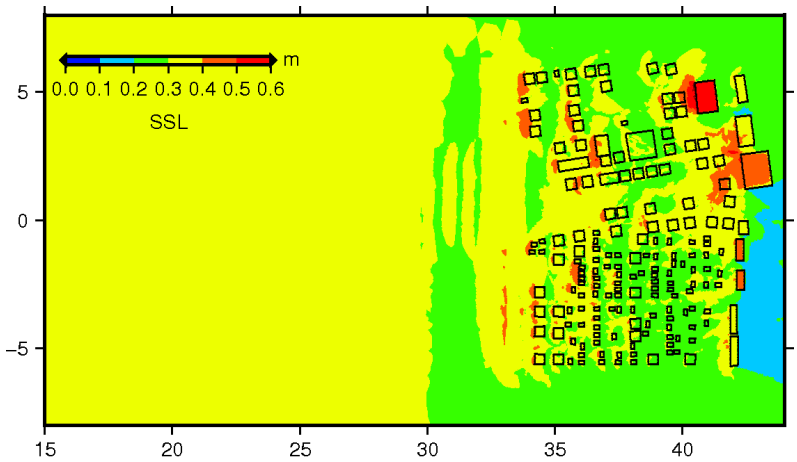

Figure 63 Maximum surface elevation for resolved mesh case (new arrangement).

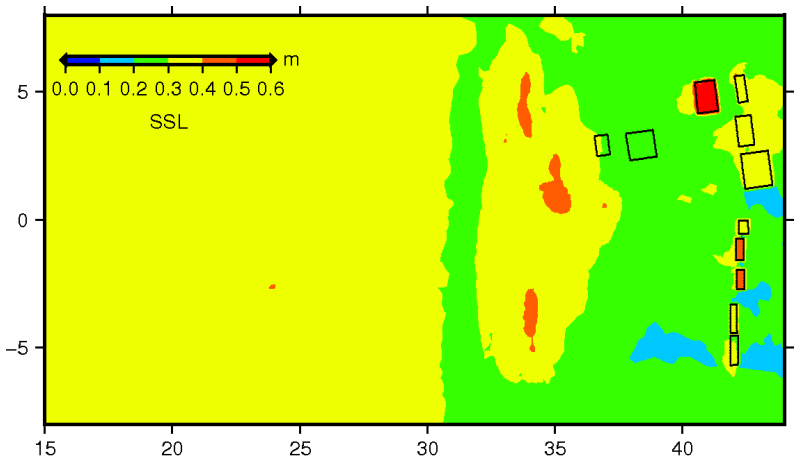

Figure 64 Maximum surface elevation for concrete-resolved mesh case (new arrangement).

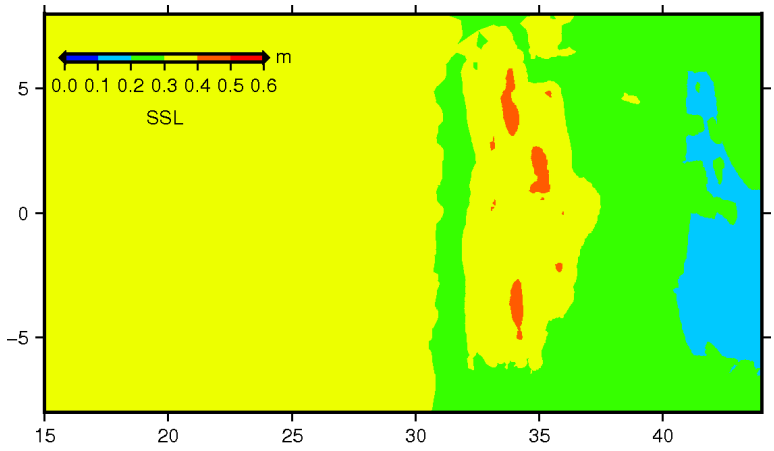

Figure 65 Maximum surface elevation for unresolved mesh case (new arrangement).

Above figures show that concrete-resolved mesh case (case 2) and unresolved mesh case (case 3) reproduced general trends of resolved mesh case (case 1) which is considered as idealized case. Differences are observed between case 2 and case 3 in reproducing high maximum surface elevation in concrete buildings area which is located in rear side of inundation area. Case 2 reproduced high maximum surface elevation while case 3 underestimated the maximum surface elevation in rear side of inundation area.

Spatial variation of maximum velocity of three cases are shown below.

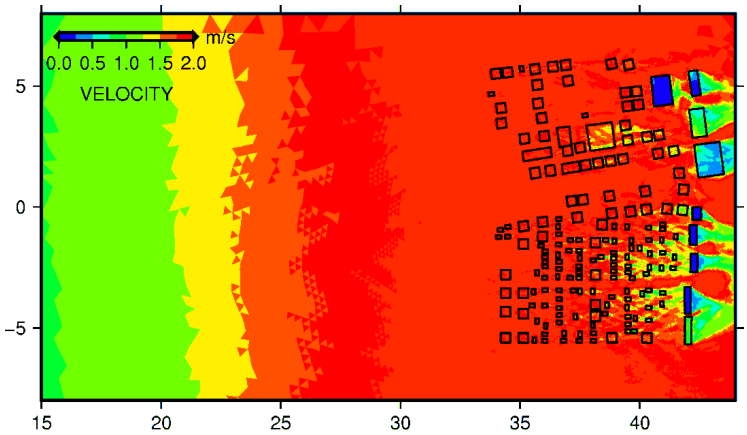

Figure 66 Maximum velocity for resolved mesh case (new arrangement).

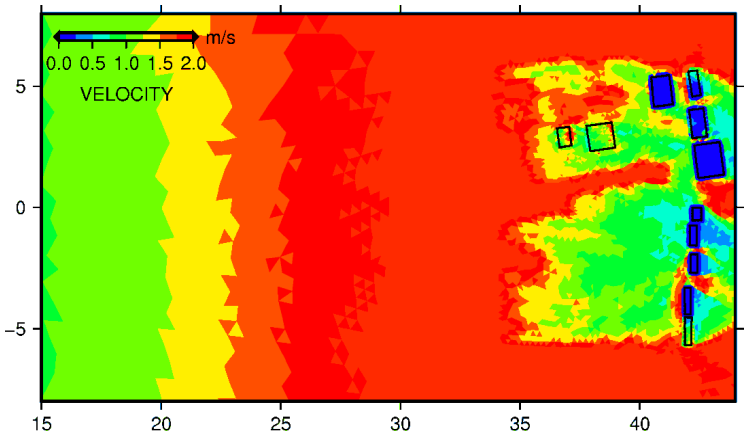

Figure 67 Maximum velocity for concrete-resolved mesh case (new arrangement).

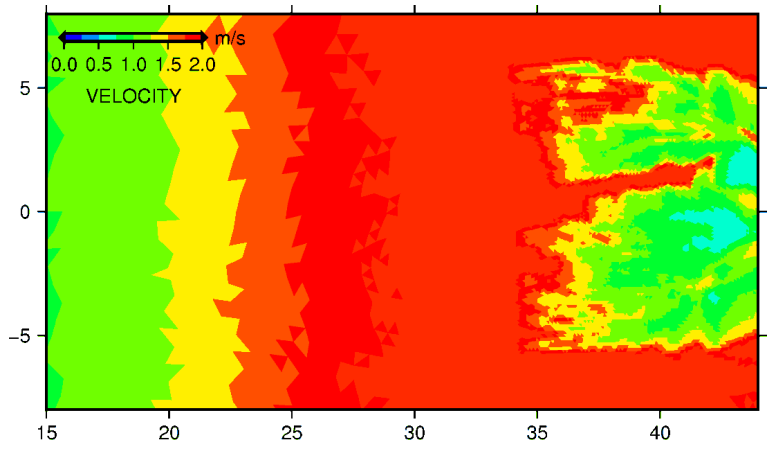

Figure 68 Maximum velocity for case 3 (new arrangement).

Above figures show that case 2 and 3 reproduced maximum velocity trends of idealized case although underestimated maximum velocity trends between buildings. These results show that maximum velocities remained high in inundation area of case 1 although buildings are resolved. However, when the buildings are replaced by bottom friction parameters on case 2 and 3 maximum velocities in inundation area reduced.

Differences between case 2 and 3 are shown around the concrete buildings location in the rear side of inundation area. Case 2 reproduced the high maximum velocities while case 3 underestimated them. The results show the advantage of using the proposed case by resolving concrete buildings.

Comparison of inundation depth at three representative points (A9, B2 and C7) are discussed below. Point locations are shown in Figure 62.

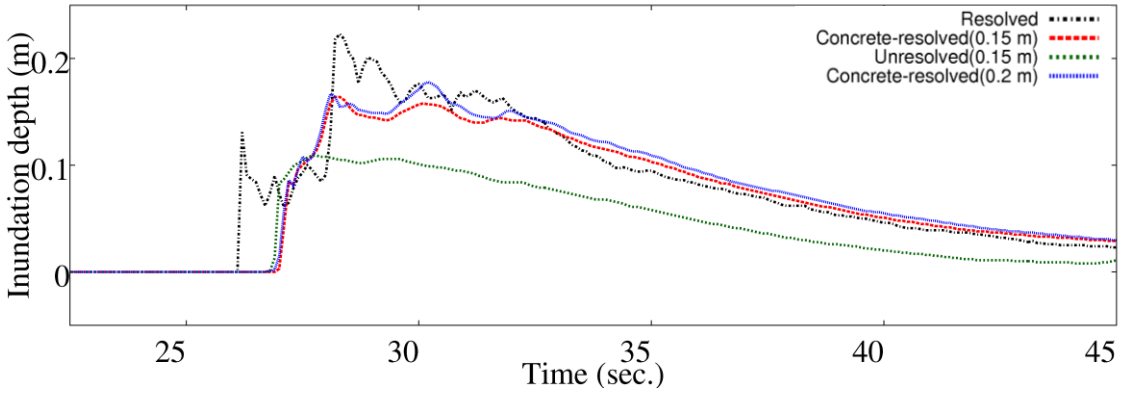

Figure 69 Inundation depth at A9 (new arrangement).

Figure 69 shows inundation depth at A9. As the point is located in the rear side of inundation area, the different phase is observed between results of resolved mesh case and other results. Unresolved mesh case results underestimated resolved mesh results while

concrete-resolved mesh case results reproduced resolved mesh results well. This results show the advantage of proposed case by resolving concrete buildings.

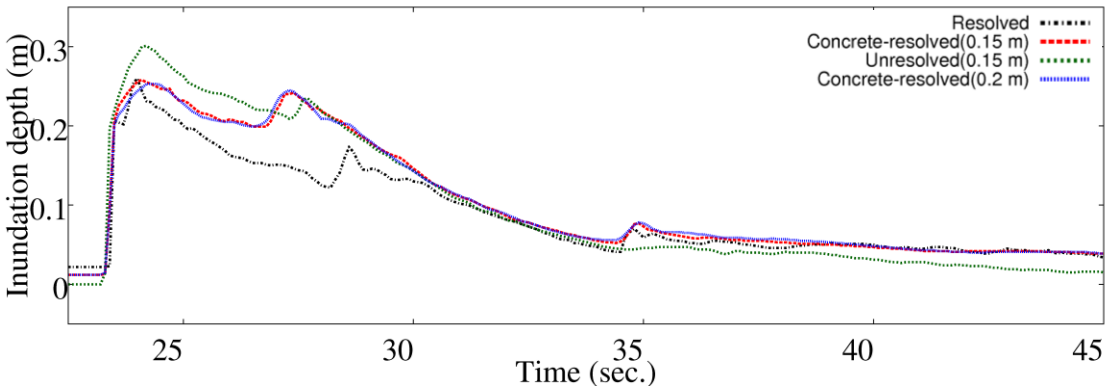

Figure 70 Inundation depth at B2 (new arrangement).

Figure 70 shows inundation depth at B2. Although location of B2 is in the front side of inundation area, concrete-resolved mesh case reproduced resolved mesh case results better than those of unresolved mesh case. Results at A9 and B2 show that concrete-resolved mesh case reproduced idealized case well both in the rear side and front side of inundation area.

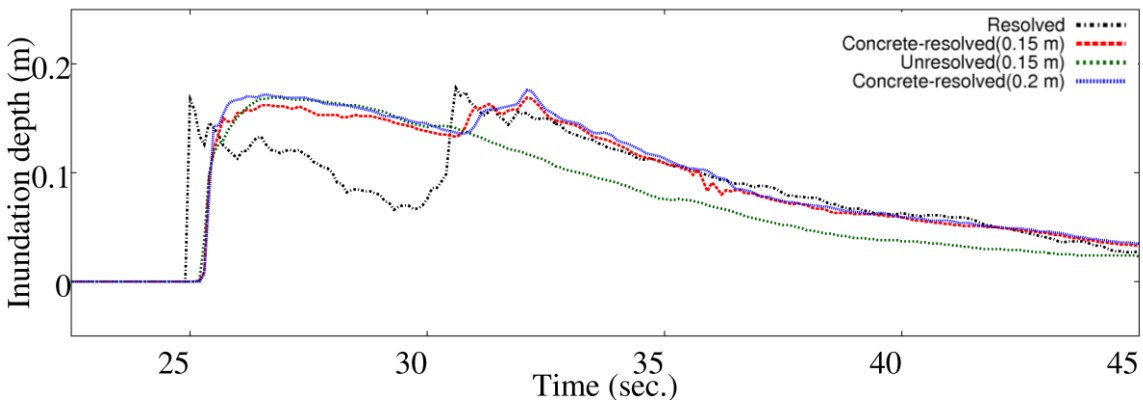

Figure 71 Inundation depth at C7 (new arrangement).

Figure 71 shows inundation depth at C7. Results of concrete-resolved mesh case and unresolved mesh case show nearly similar trend at 26-32 s. while after 31 s. concrete-resolved mesh case results reproduced resolved mesh case results closer than unresolved mesh case results which underestimated resolved mesh case results.

Simulation results with new arrangement show that although location of concrete buildings are not in the front side of inundation area, concrete-resolved mesh case results show better agreement with resolved mesh case as idealized case than unresolved mesh case.

4.3.13. Sub Chapter Conclusion

Three cases were completed for validation of the proposed study using the physical experimental results of tsunami inundation in constructed environments as follow:

1. Resolved mesh cases. These cases are idealized representation of the physical experiment in laboratory. All buildings are resolved and building heights are given. Simulations are carried out using minimum grid size 0.05 m and 0.15 m. Original bottom friction equation of FVCOM, the law of the wall, is used with minimum friction function is 0.001.

2. Concrete-resolved mesh cases. These cases are the representative of the proposed model in this study. Concrete buildings (large hotels on the water front) are resolved and concrete building heights are given. However other buildings including wooden houses are not resolved, and were replaced by bottom friction parameters. Minimum friction factor 0.001 was set to non-constructed area.

3. Unresolved mesh cases. These cases are the representative of typical method of bottom friction applications. All buildings are replaced with bottom friction equations of Imai et al. (2013). Minimum friction factor 0.001 was set to non-constructed area.

Several conclusions are drawn below:

a. Resolved mesh case results reproduced the experimental data well. Although there are underestimation in several wave gauges, general trends of experimental results are reproduced well by resolved mesh case results. The results show FVCOM was able to reproduce the experimental results well.
b. Spatial variation of surface elevation, maximum surface elevation and maximum velocity of concrete-resolved mesh case results are compared to resolved mesh case results. Although there are local discrepancies, general magnitudes of resolved mesh case results (which is considered as idealized case results) are reproduced well by concrete-resolved mesh case results. The proposed model reproduced maximum surface elevation well including high surface elevations caused by wave reflection because large hotels on the water front are resolved. Unresolved mesh case results could not reproduce the wave reflection because all buildings are not resolved.
c. Comparison of inundation depth at wave gauges are shown. Although discrepancies are observed, general tendencies of inundation depth of the proposed model followed the experimental results.
d. Comparison of cross shore velocity at wave gauges are also observed. Cross shore

velocity of the experimental results are underestimated by the proposed model. This behavior may be occurred due to absence of velocity as boundary condition and lack of resolved buildings around the wave gauges.

e. Numerical test of grid sizes are conducted. Among concrete-resolved mesh case results, grid size 0.4 m underestimated the experimental results more than simulation results with smaller grid sizes.

f. Numerical sensitivity test of friction factors show that there are slight differences between C=0.001 and C=0.005. Simulations with lower friction factor shows higher inundation depth than simulations with higher friction factor.

In this study, optimum grid size is considered as 0.3 m which is two times of the typical house size in the experiment. The reasons are as follow:

a. NRMSE value of the proposed grid size is less than 10% which meets the standard accuracy for inundation models with respect to laboratory data.

b. The proposed grid size reproduced maximum inundation depth at line B better than those of reproduced by larger grid size.

c. Number of nodes and elements used in the proposed simulation is 3.3 times smaller than those necessary for the idealized case simulation.

d. The proposed simulation system is 61.5% faster than the idealized simulation.

Considering that the proposed method aims to be applied to real case with larger number of nodes and elements, efficiency of computation time should be considered. Thus, application of the proposed method is a promising method to reduce computational cost and reproduced the acceptable tsunami inundation results.

Three types of simulations were also carried out with new arrangement using resolved mesh, concrete-resolved mesh and unresolved mesh simulations. Resolved mesh simulation results are considered as idealized case results considering that resolved mesh simulation results reproduced well experimental results of Park et al. (2013).

Several conclusions are drawn below:

a. Spatial variation of surface elevation, maximum surface elevation and maximum velocity of concrete-resolved mesh case results are compared to resolved mesh case results. General magnitudes of idealized case results are reproduced well by the proposed model. Although concrete buildings are located in the rear side of inundation

area, the proposed model reproduced maximum surface elevation and maximum velocity well while unresolved mesh simulation results could not reproduce high maximum surface elevation and high maximum velocity behind the concrete buildings.

b. Comparison of inundation depth at wave gauges are shown. Reproducibility of concrete-resolved mesh case results are closer to the resolved mesh case results as idealized case results than unresolved mesh case results.

5. MODEL APPLICATION

Application of FVCOM is discussed in this chapter. Application to the 2011 Tohoku Tsunami simulation in Tokyo Bay is discussed in sub chapter 5.1 and 5.2, while application to Kamakura is discussed in sub chapter 5.3, and application to Keicho Tsunami in Yokohama is discussed in sub chapter 5.4.

5.1. Numerical analysis of the 2011 Tohoku tsunami in Tokyo Bay focusing on high water marks in ports

5.1.1. Introduction

The 2011 Tohoku tsunami traveled along the Japanese Pacific Coast from Tohoku area to Tokyo Bay, approximately 350 km away from the epicenter. Tokyo Bay has the total area of 1,320 km^2. The governments have made substantial efforts to protect the area against natural disasters, including earthquakes, storm surges, and tsunamis as the catchment area of the bay is the most densely populated area in Japan,.

The local government had considered that the expected major water-related disaster in Tokyo Bay was storm surge. Disaster prevention structures have been designed against storm surges which are shorter in the southern part of the bay, e.g. Yokohama Port and taller in the bay head, e.g. Tokyo Port (Sasaki et al., 2012). Tsunamis had been generally considered less dangerous than storm surges in the bay before the occurrence of the 2011 tsunami because the worst case of tsunami model used by most of local governments was the 1923 Great Kanto Earthquake Tsunami, which did not cause major damage especially at the bay head (Sasaki et al., 2012).

Sasaki et al. (2012) have studied the behavior of 2011 Tohoku Tsunami in Tokyo Bay using field survey and numerical simulations. However, the amplification of tsunami wave in each port remains unclear. In order to clarify the mechanism of tsunami amplification in each port, numerical approach is required since analytical solution may not be always applicable because of the special feature in each port.

Since the spatial scale of the ports is much smaller than that of the major tsunami propagation area, application of an unstructured-mesh model is necessary to create an efficient numerical simulation. Thus, the objective of this model application is to elucidate

the mechanism of the 2011 Tohoku Tsunami in ports in Tokyo Bay by application of the unstructured-mesh model FVCOM (Chen et al., 2003).

5.1.2. Simulation setup

SMS 10.1 was utilized to create an unstructured-grid mesh system covering the tsunami propagation area from east longitude 120 to 177.2 degrees and north latitude of 1.4 to 59.7 degrees. In Tokyo Bay, coastline dataset from the National Land Numerical Information (MLIT) with higher resolution was utilized. While other area were developed using Coastline Extractor (NOAA) data.

GEBCO_08 bathymetric data with 30 second mesh resolution was utilized inside Japan, while for Tokyo Bay area, Japan Oceanographic Data Center (JODC) bathymetric data was utilized with 500 m mesh resolution. Other area outside Japan was constructed using bathymetric data provided by ETOPO with 10 minute mesh resolution.

Chiba Port, Funabashi Fishery Port, Kisarazu Port, Yokohama Port, Kurihama Port, and Yokosuka Port were finely resolved with 5 m local resolution mesh systems while 100 m grid size was used inside Tokyo Bay, 1 km in tsunami source area, and 50 km in the ocean. Whole domain mesh is shown in Figure 72a, location of ports and Tokyo Bay area mesh system is shown in Figure 72b, while the port mesh systems are shown in Figure 73. Mesh system details are shown in Table 9.

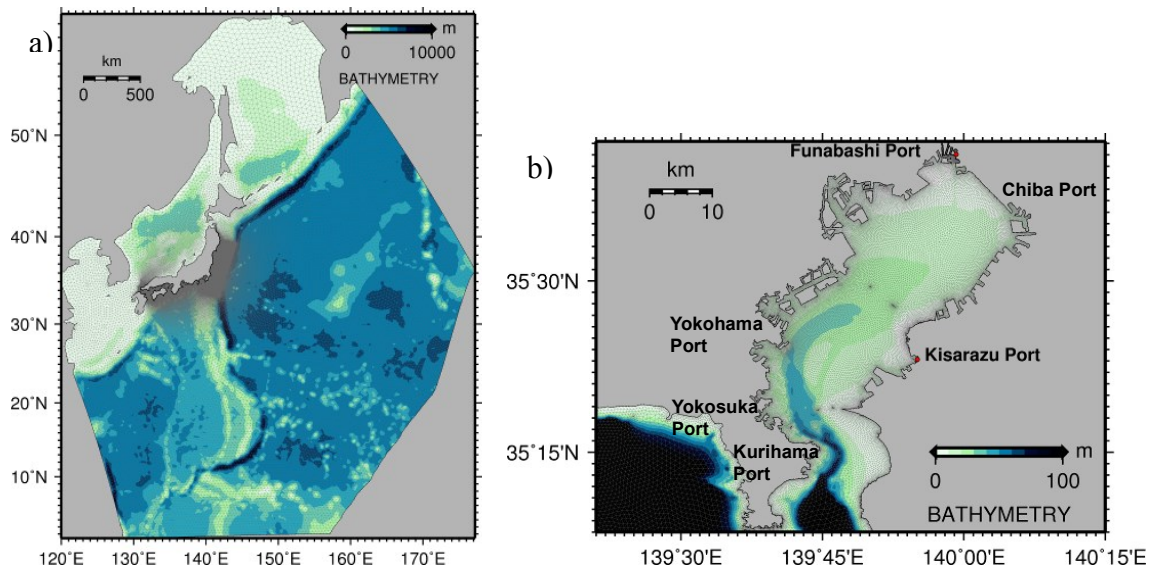

Figure 72 Mesh system of: a) Whole domain, b) Tokyo Bay area.

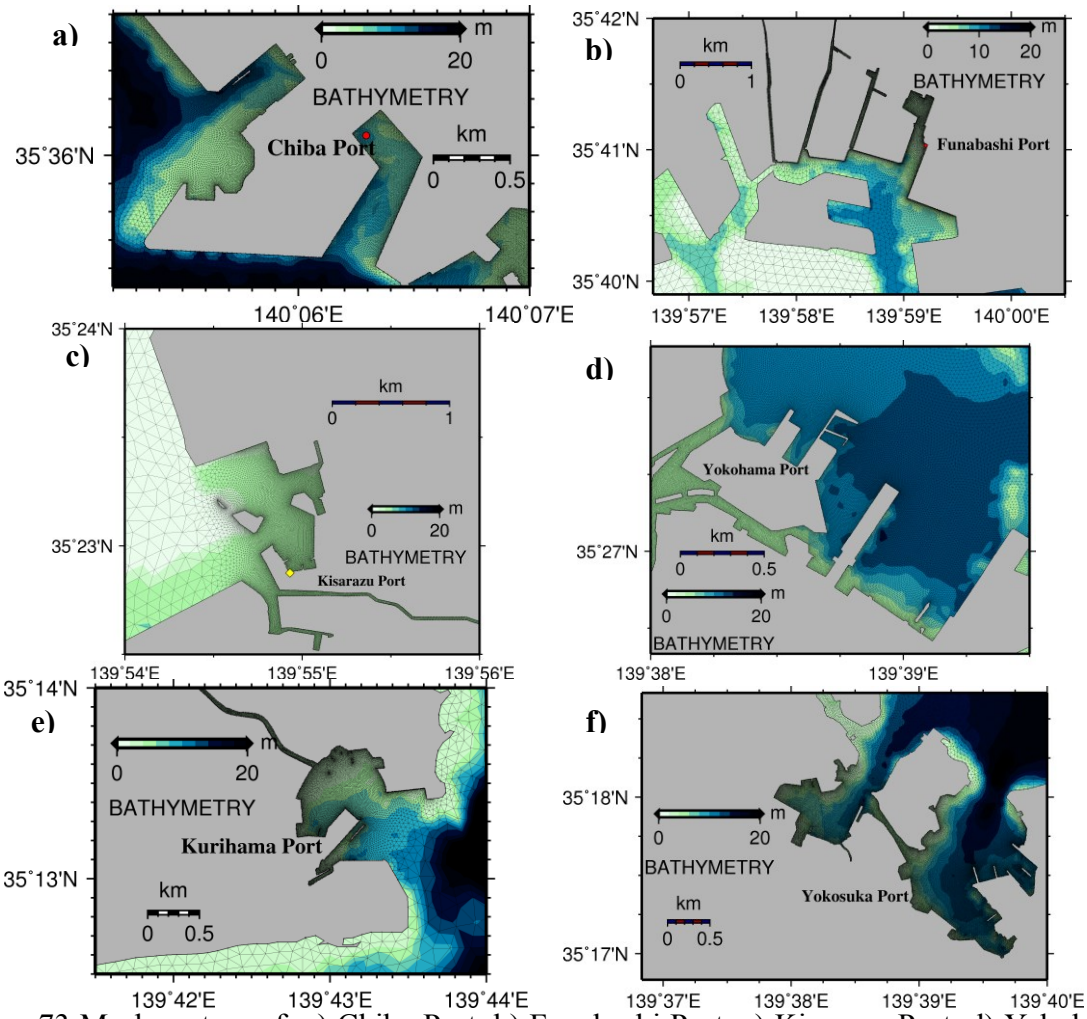

Figure 73 Mesh system of: a) Chiba Port, b) Funabashi Port, c) Kisarazu Port, d) Yokohama Port, e) Kurihama Port, f) Yokosuka Port.

Several fault models have been proposed for tsunami simulation. Parameters by Wei et al. (2011), Fujii et al. (2011), Gusman et al. (2011) and Tohoku University (2011) were selected as initial surface elevation. With modification of surface elevation, simulations S1, S2, S3, and S4 were carried out for each fault parameter respectively.

Table 9. Mesh System Details

No	Mesh System	Nodes	Elements
1	Chiba Port	475,187	906,910
2	Funabashi Port	450,200	857,154
3	Kisarazu Port	448,819	855,337
4	Yokohama Port	484,265	918,914
5	Kurihama Port	453,760	863,725
6	Yokosuka Port	487,583	932,172

A MPI-parallel supercomputer HA8000 (Hitachi Ltd.) at the University of Tokyo with 64-node and 16-node was utilized for executing the simulations. Time step for the external gravity mode was 0.05 s and bottom friction coefficient was 0.0025. The wall clock time for each computation took approximately 1~3 hours for 6 hours of model time.

5.1.3. Comparison between tidal data and simulation results

Figure 74 shows comparison between tidal data and simulation results at six wave gauges in Chiba Port, Funabashi Port, Kisarazu Port, Yokohama Port, Kurihama Port and Yokosuka Port. The horizontal axis shows JST time on March 11, 2011 while the vertical axis shows the sea surface displacement in meter.

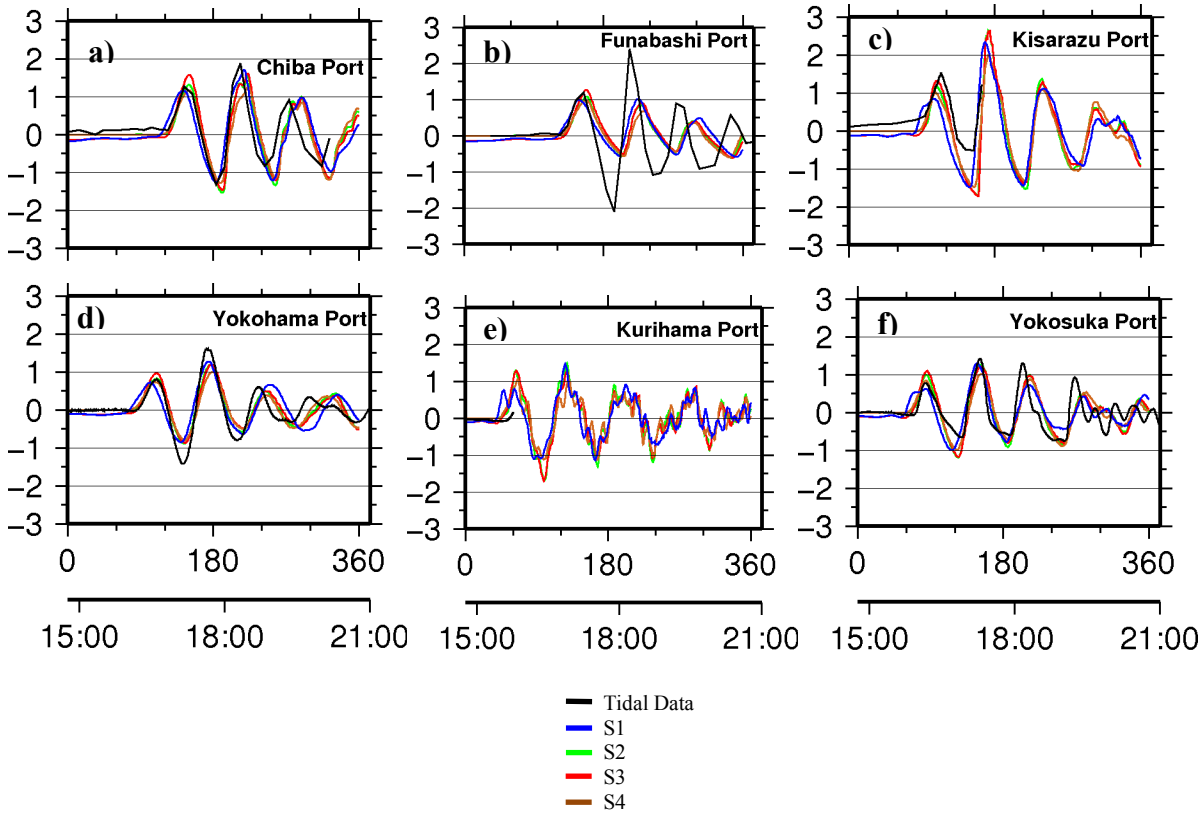

Figure 74 Comparison of tidal data and simulation results at Chiba Port, Funabashi Port, Kisarazu Port, Yokohama Port, Kurihama Port, and Yokosuka Port.

Simulations reproduced the tidal data quite well in Chiba Port (Figure 74a), Yokohama Port (Figure 74d), and Yokosuka Port (Figure 74f). However, phases lag are observed after the second wave. Grilli et al. (2007) reported the discrepancies after the first wave on the numerical simulation on the 2004 Indian Ocean Tsunami at Gan. This behavior

may be occurred due to the tidal gauge which is located within a protected area which is quite affected by local coastal topography. In this study, the bathymetry data inside Tokyo Bay has 500 m resolution. The phase lag between simulations and tidal data after the second wave may due to this lack of bathymetry data resolution.

Simulation results in Kurihama Port (Figure 74e) show high frequency wave. This behavior may be appeared because Kurihama Port is located in Tokyo Bay entrance. The wave reflection between eastern and western side of the bay entrance may affected the wave around Kurihama Port.

Discrepancies of simulation results are also observed in Funabashi Port (Figure 74b) and Kisarazu Port (Figure 74e). The possible cause of discrepancy is low resolution of bathymetry data.

Amplification of tsunami are also observed in Funabashi Port (Figure 74b). Wave reflection and occurrence of harbor resonance may be the cause of amplification. Harbor oscillations, a specific type of seiche motion that occurs in partially enclosed basins that are connected through one or more openings to the sea, may exist and cause the wave amplification. When the frequencies of arriving tsunami waves match the resonant frequencies of the bay, destruction may occur (Rabinovich, 2009).

The tsunami amplification in Funabashi Port however could not be reproduced by simulations. The lack of bathymetry data in Funabashi Port may be the reason of this issue. An approximately 12 m depth navigation channel was not included in the bathymetry data while the tidal gauge location in Funabashi Port is quite deep inside the narrow channel.

In Kisarazu Port (Figure 74e), tidal data shows wave trough is smaller compared to the wave crest. This behavior are also observed in tidal data at Visakhapatnam and Paradip (Fujii and Satake 2007), Male and Hanimadhoo (Fujii and Satake 2007, Grilli et al., 2007), during the 2004 Indian Ocean Tsunami. Grilli et al. (2007) inferred that usually the actual tide gage depth is smaller than the simulated one and therefore the simulated trough tsunami wave could not be reproduced well.

5.1.4. Effect of bathymetry change

Sensitivity tests of bathymetry change were conducted. The bathymetry inside each port was decreased by a factor of two (half-depth case) and was increased by a factor of two (twice-depth case). The details are shown in Table 10.

Source parameter S2 from Fujii et al. (2011) was utilized for sensitivity simulations. The results are shown in Figure 75. The horizontal axis shows JST time on March 11, 2011 while the vertical axis shows the sea surface displacement in meter.

Table 10. Bathymetry Depth around Tidal Gauge

No	Mesh System	Original Depth	Half Depth	Twice of Depth
1	Chiba Port	4 m	2 m	8 m
2	Funabashi Port	3 m	1.5 m	6 m
3	Kisarazu Port	3 m	1.5 m	6 m
4	Yokohama Port	8 m	4 m	16 m
5	Kurihama Port	18 m	9 m	35 m
6	Yokosuka Port	7 m	14 m	3.5 m

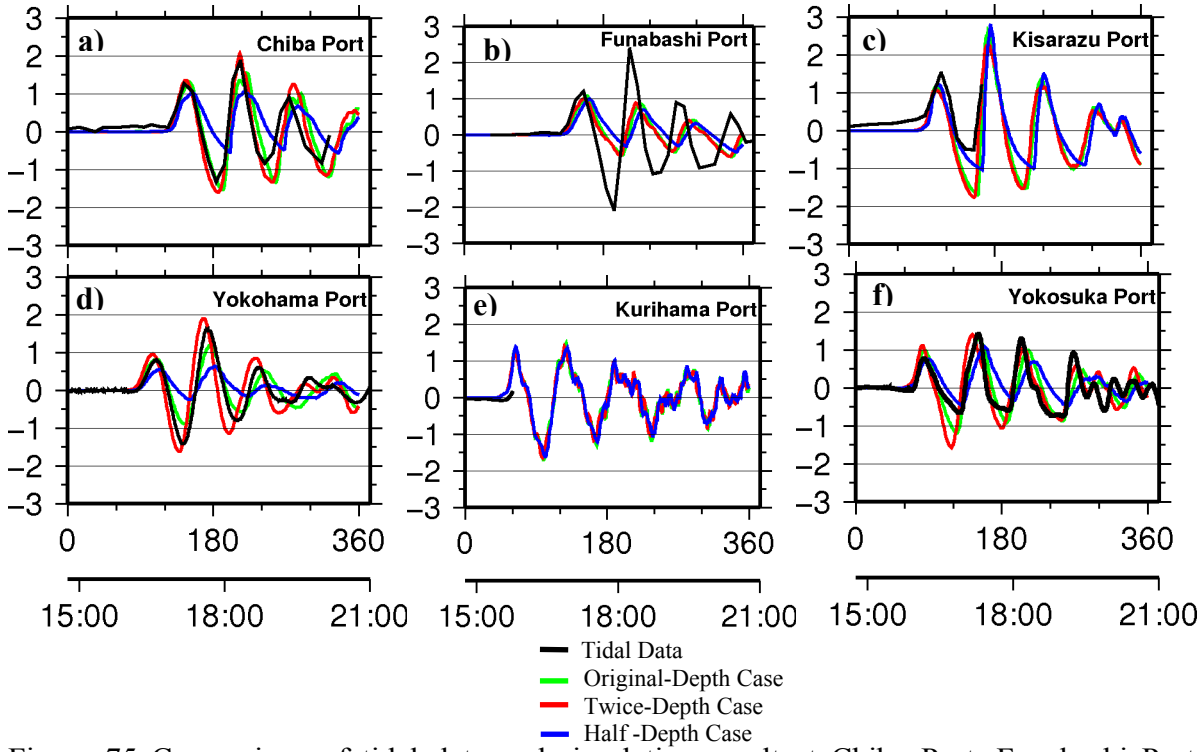

Figure 75 Comparison of tidal data and simulation result at Chiba Port, Funabashi Port, Kisarazu Port, Yokohama Port, Kurihama Port, and Yokosuka Port with difference of bathymetry data.

The same behavior between original-depth case, twice-depth case, and half-depth case are shown in Chiba Ports (Figure 75a), Funabashi Port (Figure 75b), Yokohama Port (Figure 75d) and Yokosuka Port (Figure 75f). Half-depth case shows the lowest amplitude, and then followed by original-depth case while the twice-depth case shows the highest amplitude. Half-depth case (blue line) shows different wave phase compared to other two simulations. The same behavior is also observed in Funabashi Port although tidal data is underestimated by three simulations.

General condition is observed from those simulations: the deeper the bathymetry inside the port, the higher wave amplitude inside the port is. In addition, lower bathymetry case (half-depth case) was able to make the wave phase change from the original wave phase.

Different conditions are observed in Kisarazu Port (Figure 75c) and Kurihama Port (Figure 75e). In Kisarazu Port, the highest amplitude is observed for half-depth case, followed by original-depth case then twice-depth case. However amplitudes of trough waves are smaller compared to the wave crest. In Kurihama Port, no significant differences are observed among three simulation results. This condition may be occurred due to the deep (18 m) and high variation (from approximately 6~20 m depth) of bathymetry around Kurihama Port while the water depth around other ports are less than 10 m and approximately 10 m variation in water depth.

Kisarazu Port and Kurihama Ports show different behavior from results in other ports. It indicates that bathymetry effect around the coastal area is not the only factor on which the amplitude as well as the phase of tsunami waves depends. It is consistent with Duong et al. (2008) who inferred that tsunami wave amplitude on the coastline will be higher not only by variations in bathymetry, but also because of their fault sources. Satake (1988) further explained that amplitude of tsunami is affected by three groups of factors: those related to source, the propagation path, and shore effects.

5.1.5. Sub Chapter Conclusions

FVCOM 2.6.1 is utilized to calculate the 2011 Tohoku Tsunami propagation in Tokyo Bay focusing on Chiba Port, Funabashi Port, Kisarazu Port, Yokohama Port, Kurihama Port and Yokosuka Port with 5 m mesh resolution. The relationship between coastal bathymetry and tsunami wave amplitude are observed. The deeper bathymetry inside the port, the higher wave amplitude is. The wave amplitude does not only depend on coastal bathymetry, but also on the source of the tsunami.

Simulation results well reproduced tidal data in Chiba Port, Yokohama Port, Kurihama Port and Yokosuka Port. In Yokohama Port and Yokosuka Port, wave heights are well simulated reaching 1.2 m height. In Chiba Port, computed wave height is consistent with the tidal data reaching maximum height of 1.7 m on the second wave. In Kurihama Port, 1 m height of first tsunami wave are reproduced by simulation.

Discrepancies between tidal data and simulations results in Funabashi Port and Kisarazu Port are observed. The probable cause of discrepancy is low resolution of bathymetry data especially in Funabashi Port and Kisarazu Port. An approximately 12 m depth navigation channel was not included in the bathymetry data while the tidal gauge location in Funabashi Port is quite deep inside the narrow channel. Thus, there is difference between simulated bathymetry and the real bathymetry. It is necessary to improve the bathymetry data inside the Tokyo Bay ports to obtain better results.

5.2. Numerical assessment of the 2011 Tohoku Earthquake Tsunami in Ports of Tokyo Bay with the Effectiveness of Floodgates

5.2.1. Introduction

On March 11, 2011 at 14:46 JST, the 2011 Tohoku Earthquake caused giant tsunami. The 2011 Tohoku Earthquake tsunami traveled into Tokyo Bay although the epicenter was located in the Tohoku area. Unexpectedly large inundation heights within ports occurred, such as 2.8 m in Funabashi Fishery Port and 2.9 m in Shin-Futtsu Fishery Port (Sasaki et al., 2012).

Floodgates in ports were reported to be quite effective at reducing water flow to surrounding areas when they closed while the failure of closing floodgates, observed in some ports, may have led to severe damage (Sasaki et al., 2012). Floodgates had some effect in preventing the inland penetration of the tsunami and that prevention occurs only when the walls around floodgates are high enough that the tsunami cannot overtop them (Ogasawara et al., 2012).

During the 2011 Tohoku Earthquake tsunami, the 8 m floodgate in Minami-Sanriku, a town in Miyagi Prefecture, was overtopped and completely destroyed (Suppasri et al., 2012). The effectiveness of a floodgates were also reported at Fudai, Iwate Prefecture (Carayyanis 2011, Ogasawara et al., 2012), at Noda and Iwaizumi (Ogasawara et al., 2011).

The objectives of the present application are:

1) to elucidate the mechanism responsible for the high tsunami amplification in some ports in Tokyo Bay using numerical simulation which were not well reproduced by Wiyono and Sasaki (2012).

2) to assess the effectiveness of floodgates in the bay, when they close, along with the potential damage that arises when floodgates do not close.

5.2.2. Simulation setup

SMS 10.1 was utilized to create an unstructured-grid mesh system covering the tsunami propagation area from east longitude 120 to 177.2 degrees and north latitude of 1.4 to 59.7 degrees. Coastline dataset from Coastline Extractor (NOAA) was utilized for whole domain except Tokyo Bay. In Tokyo Bay, coastline data from the National Land Numerical Information (MLIT) with higher resolution was utilized. While other area were developed using Coastline Extractor (NOAA) data.

Bathymetry data, having a 10-minute resolution and provided by ETOPO, was utilized for the whole domain except for the area around Japan. GEBCO_08 bathymetry data with 30-s resolution was used for the area around Japan, while 50-m resolution data provided by Chiba Port Bureau of MLIT was adopted for the area in Tokyo Bay.

The mesh size varied from 100 m inside Tokyo Bay to 1 km in the tsunami source area, and 50 km in the ocean. Two ports in Tokyo Bay, Funabashi Fishery Port and Kisarazu Port were finely resolved with a 5-m mesh. Mesh systems with 5-m resolution were also constructed for expected inundation areas around these ports. Two floodgate cases are simulated, closed and open. The sea-land mesh system is utilized to simulate the open-gate case, while the sea mesh system is utilized to simulate the close-gate case.

The whole domain and Tokyo Bay mesh system are shown in Figure 76a and Figure 76b, respectively, including the locations of the two ports.

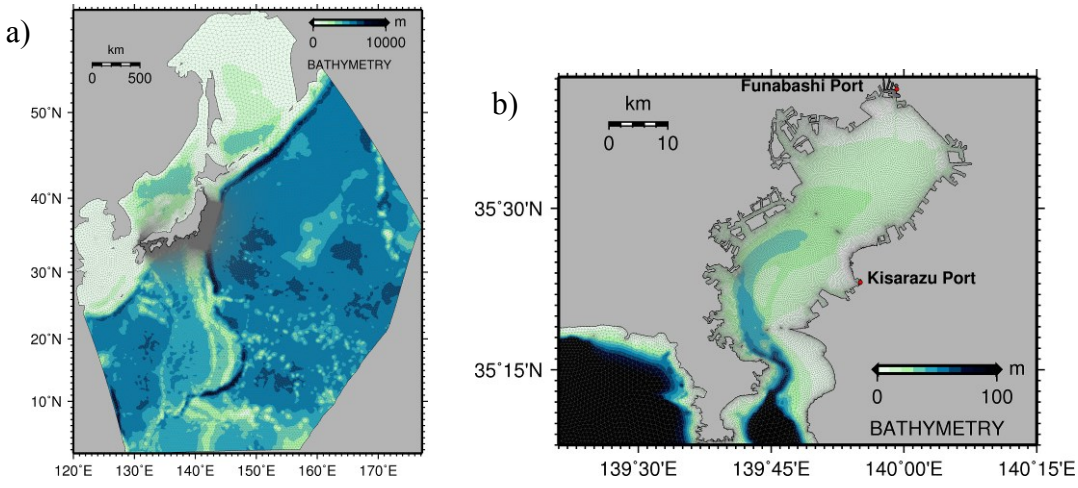

Figure 76 Mesh system of: a) Whole domain, b) Tokyo Bay area.

The sea mesh and sea-land mesh in Funabashi Port are shown by Figure 77a and Figure 77b, respectively. Letters A, B, C, and D in Figure 77a designate small rivers, and FFP stand for Funabashi Fishery Port. The sea mesh and sea-land mesh in Kisarazu Port are shown by Figure 77c and Figure 77d, respectively. In the closed-gate case, a floodgate is assummed to be higher than the wave height, so that the wave does not overtop it. In addition, the port is surrounded by dike. In the open-gate case, neither a floodgate nor a dike is modeled around the port. The open-gate case was created to understand tsunami behavior when the floodgate fails to be closed as the wave is coming. Table 11 shows the total numbers of unstructured mesh nodes and elements for each port mesh system.

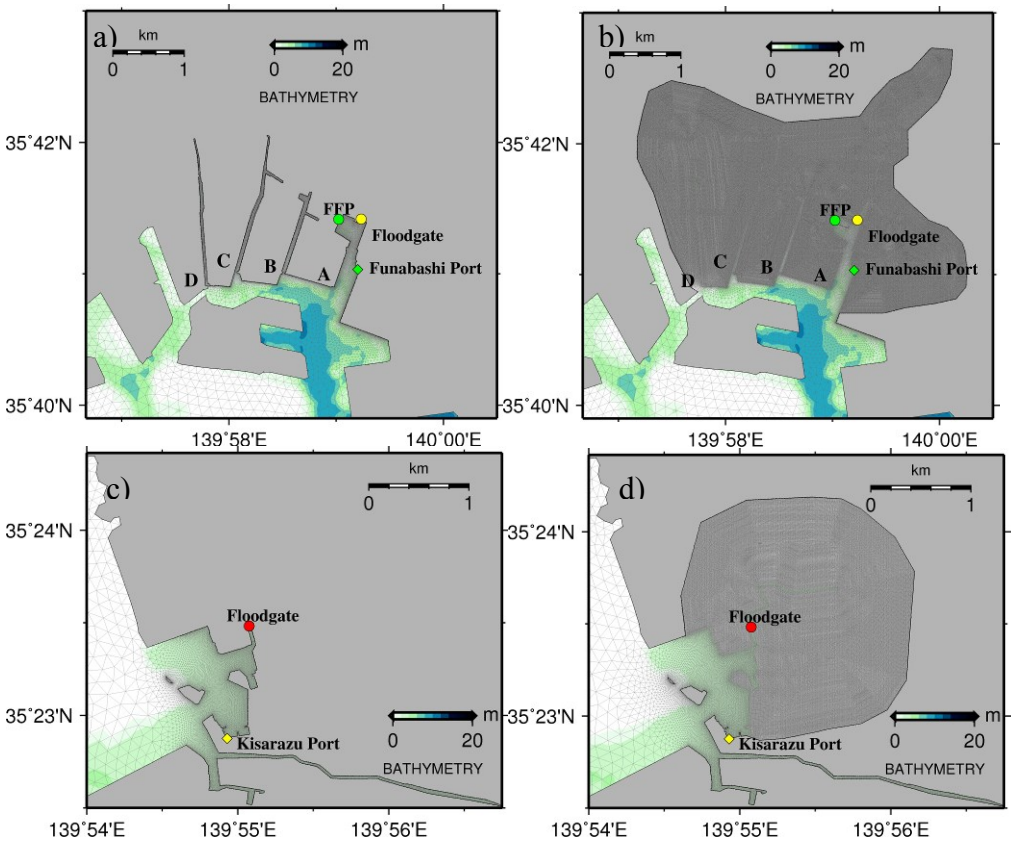

Figure 77 Mesh system of: a) Funabashi Port (without land mesh), b) Funabashi Port (with land mesh), c) Kisarazu Port (without land mesh), d) Kisarazu Port (with land mesh).

A fault model of Okada (1985) was used to calculate the spatial variation in initial surface elevation. Fault model parameters values proposed by Wei et al. (2011) was selected among several sets of values to calculate initial surface elevation.

The drag coefficient was determined from the logarithmic law of the wall taking the minimum value of 0.0025 and the time step for the external gravity mode was set to 0.05 s.

Computation time was 1-3 hour for 6 hour of each model time, using an MPI-parallel supercomputer HA8000 (Hitachi Ltd.) at the University of Tokyo with 64 nodes.

Table 11. Mesh system

No	Mesh System	Nodes	Elements
1	Funabashi Port (sea mesh)	450,200	857,154
2	Funabashi Port (sea-land mesh)	918,265	1,793,945
3	Kisarazu Port (sea mesh)	448,819	855,337
4	Kisarazu Port (sea-land mesh)	538,409	1,034,231

5.2.3. Comparison between tidal data and simulation result

Comparison between tidal data and simulation results at tidal gauge points in offshore stations and ports are shown in Figure 78. The horizontal axis shows simulation time in minutes while the vertical axis shows the sea surface displacement in meter.

Simulation results reproduced well tidal data in tidal gauge points in ports (Chiba Port and Yokohama Port) and offshore stations (Chiba Light House and Ashika Island). The maximum observed data of 0.94 m and 0.86 m at the Chiba Light House station and the Ashika Island station, respectively, are reproduced well by computed results. The wave phase are also reproduced well by the simulation results. At Yokohama Port and Chiba Port, the observed maximum tsunami heights of 1.61 m and 1.87, respectively, were also reproduced well along with phase by the simulation.

Comparison of tidal data and simulation results in Kisarazu Port is shown in Figure 78e. Both simulations underestimated the first crest wave by 0.5 m. The shallow wave trough (-0.5 m) was not reproduced by the simulations. However, the simulated waves agree in phase. As discussed in Wiyono and Sasaki (2012), the shallow wave trough may due to the used bathymetry data, which is deeper than the actual bathymetry. Wiyono and Sasaki (2012) overestimated the tsunami trough in by 1 m, while results in this study overestimate it by 0.5 m. This study obtained better estimation accuracy, compared to that in Wiyono and Sasaki (2012), because data resolution is improved in this study (50-m resolution data), while the data having 500-m resolution was utilized by Wiyono and Sasaki (2012). However discrepancy still exists. The probable reason may be the bathymetric details, which could not be modeled by the present data.

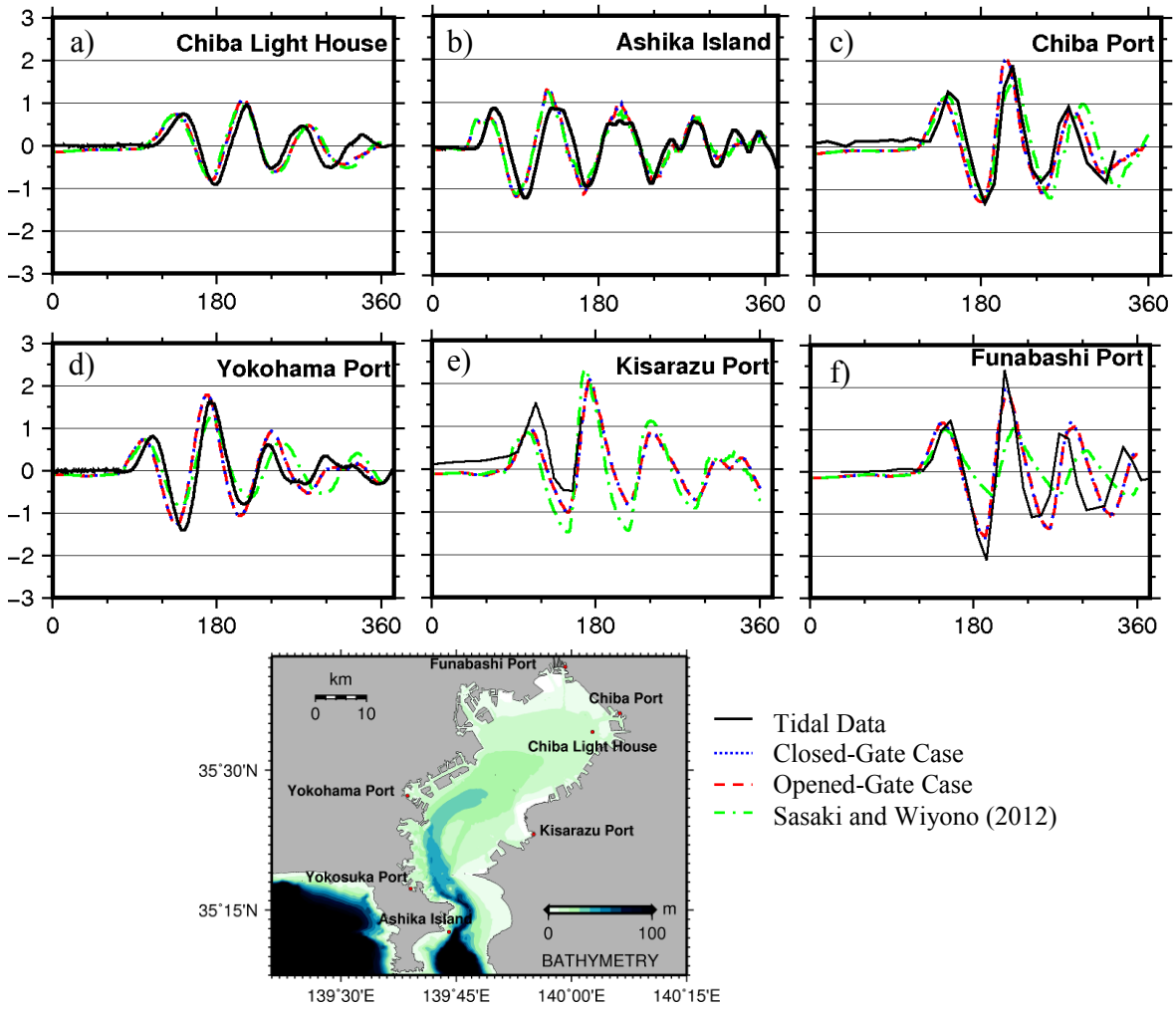

Figure 78. Comparison of tidal data and simulation results at: a) Chiba Light House, b) Ashika Island, c) Chiba Port, d) Yokohama Port, e) Kisarazu Port, and f) Funabashi Port.

In Funabashi, there are two ports. Funabashi Port (for commercial use) and Funabashi Fishery Port. Figure 78f shows a comparison of tidal data (black) and simulation results when the floodgate in Funabashi Port is closed (blue) and opened (red). In the both simulations, the first wave in Funabashi Port is underestimated by 0.1 m. The second wave is underestimated by 0.4 m in the closed-gate case and underestimated by 0.6 m in the opened-gate case. Different from the first and second waves, the third wave is overestimated by 0.3 m in the closed-gate case and overestimated by 0.1 m in the opened-gate case. For the third and forth waves, there is a phase lag between tidal data and both simulation results.

Although it was not shown in the figure, simulation results were also taken in Funabashi Fishery Port. The observed inundation height in Funabashi Fishery Port reached 2.84 m (Sasaki et al., 2011) while this study underestimated it by 0.54 m.

Figure 78f showed amplification of wave height in Funabashi Port. The amplification may due to the wave reflection. The second wave was observed 2.4 m in height, while the closed-gate case underestimated by 0.4 m and the open-gate case underestimated by 0.6 m. Because the bathymetry data utilized in this study has a 50-m resolution while Wiyono and Sasaki (2012) used data having a 500-m resolution, simulations in this study show better agreement than those simulated by Wiyono and Sasaki (2012). The navigation channel near the port, approximately, 12 m deep could not modeled by the 500-m resolution bathymetry while it is modeled well by the 50-m resolution bathymetry.

For the second and third tsunami waves, differences between results for the open-gate and closed-gate cases are observed. The open-gate case simulation results are lower than that for the closed-gate case. An occurence of wave reflection in the closed-gate case is probably a cause of this difference.

5.2.4. Spatial variation in computed surface level for open-gate and closed-gate cases

Figure 79 and Figure 80 show spatial variations in the computed surface level for Funabashi Port and Kisarazu Port.

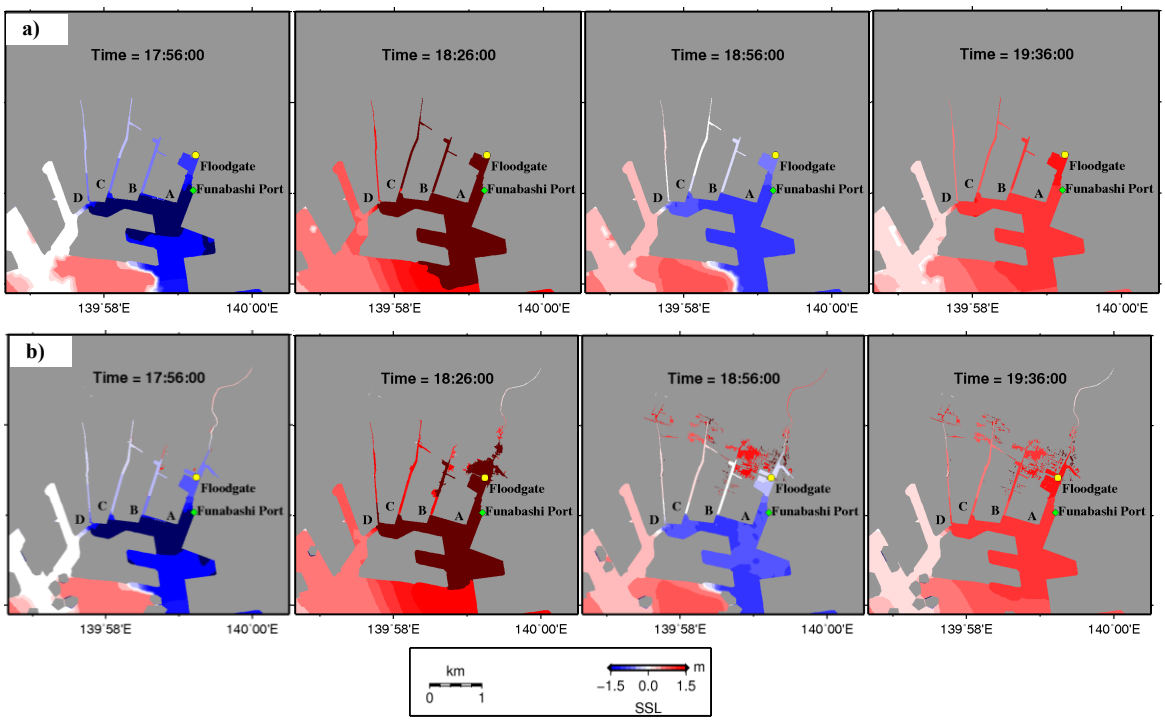

Figure 79. Time variation in spatial distribution of the computed surface level in Funabashi Port: a) when the floodgate is closed, b) when the floodgate is opened.

The range for the surface level is between -1.5 m (dark blue) and +1.5 m (dark red). Figure 79 shows time variation in spatial distribution of the computed surface level in Funabashi Port. The second wave started to enter Funabashi Port at 17:56 JST. The sea level in Funabashi Port reached a maximum at 18:26 JST. The second wave inundated larger area than that for the first wave.

Figure 80 shows time variation in spatial distribution of the computed surface level in Kisarazu Port. A shallow water area exists at the left hand side of Kisarazu port (see Figure 77e and Figure 77f). The wave started inundating at 17:36 JST when the floodgate was opened. A maximum wave height of 2 m is reached at 17:41 JST.

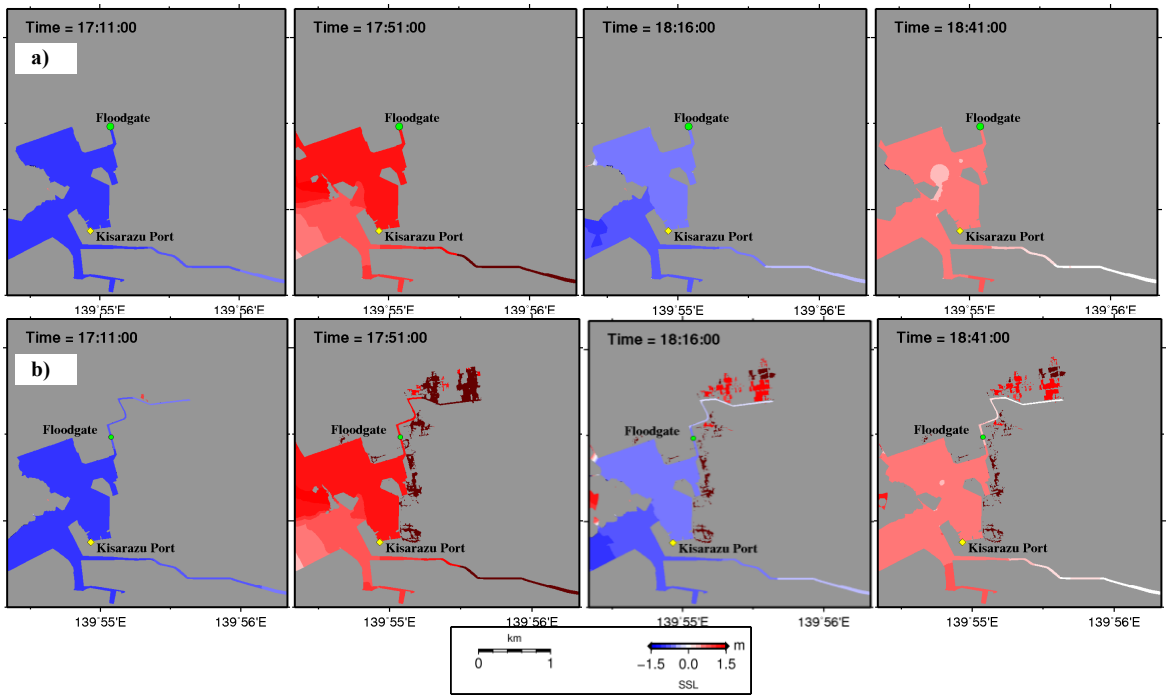

Figure 80. Time variation in spatial distribution of the computed surface level in Kisarazu Port: a) when the floodgate is closed, b) when the floodgate is opened.

The spatial variations in computed surface levels for both the open-gate and closed-gate cases of the tsunami show that the closed-gate case can prevent the surrounding area from inundation, while the failure of closing floodgates will cause inundation.

5.2.5. Inundation height for open-gate case

Figure 81a and Figure 81b show the maximum computed surface levels in Funabashi Port and Kisarazu Port for the open-gate case, respectively. The utilized range for the surface level is between 0 m (white) and +2.5 m (dark red).

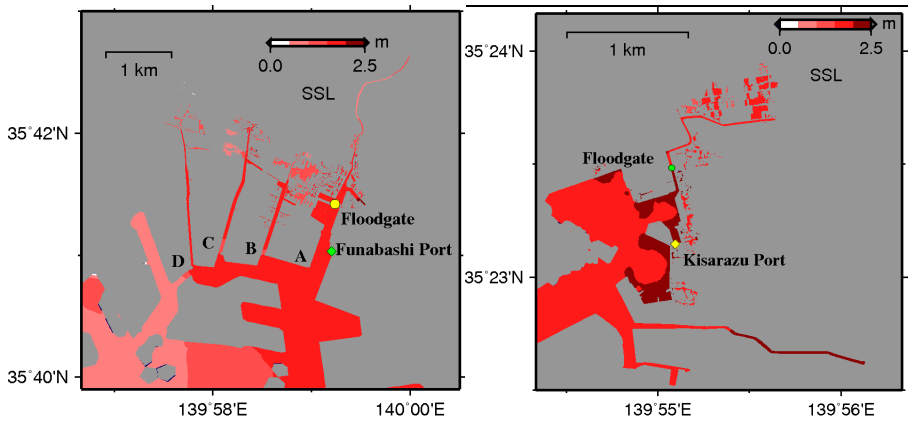

Figure 81. a) Maximum computed surface level for open-gate case in Funabashi Port, b) Maximum computed surface level for open-gate case in Kisarazu Port

For the open-gate case in Funabashi Port (Figure 81a), the second wave coming to the port caused the largest inundation. Instead of inundating the port's mouth which is adjacent to the sea, the second wave inundated the area around Funabashi Fishery Port, which is further away from the sea. The possible reason is that the area around the port's mouth is more than 2 m in land height, higher than the tsunami wave height, while the area around Funabashi Fishery Port is less than 2 m in land height, lower than the wave height. The wave inundated the area as far as 620 m from the corresponding nearest river.

At the east, west, and north sides of Kisarazu Port (Figure 81b), area with land height less than 1.5 m was inundated. Inundation in north area extended 450 m from the river in Kisarazu Port because the land height in that area less than 1 m. The effectiveness of a floodgate is clear by analyzing the inundation area of a tsunami when the floodgate fails to shut.

Figure 82 shows the time series of computed surface elevation in the open-gate case at three points in Funabashi Port (F1, F2, and F3) and Kisarazu Port (K1, K2, and K3). The vertical axis shows the sea surface displacement in meter while the horizontal axis shows simulation time in minutes. At the beginning of simulation, the area was dry so the initial surface elevation at each point was zero. When tsunami starts to inundate the location, the surface elevation increases at the corresponding location.

The points F1, F2, and F3 were located 449 m, 325 m, and 137 m, respectively, from the closest rivers in Funabashi. The land height at each point was 1.41 m, 1.31 m, and 1.42 m, respectively. The inundation height at each point reached 1.53 m, 1.79 m, and 1.97 m, respectively. The points K1, K2, and K3 were located 460 m, 200 m, and 26 m, respectively, from the closest rivers in Kisarazu. The land height in each point was 1.42 m, 1.28 m, and

0.98 m, respectively and the inundation height at each point reached 1.44 m, 1.7 m, and 1.72 m, respectively.

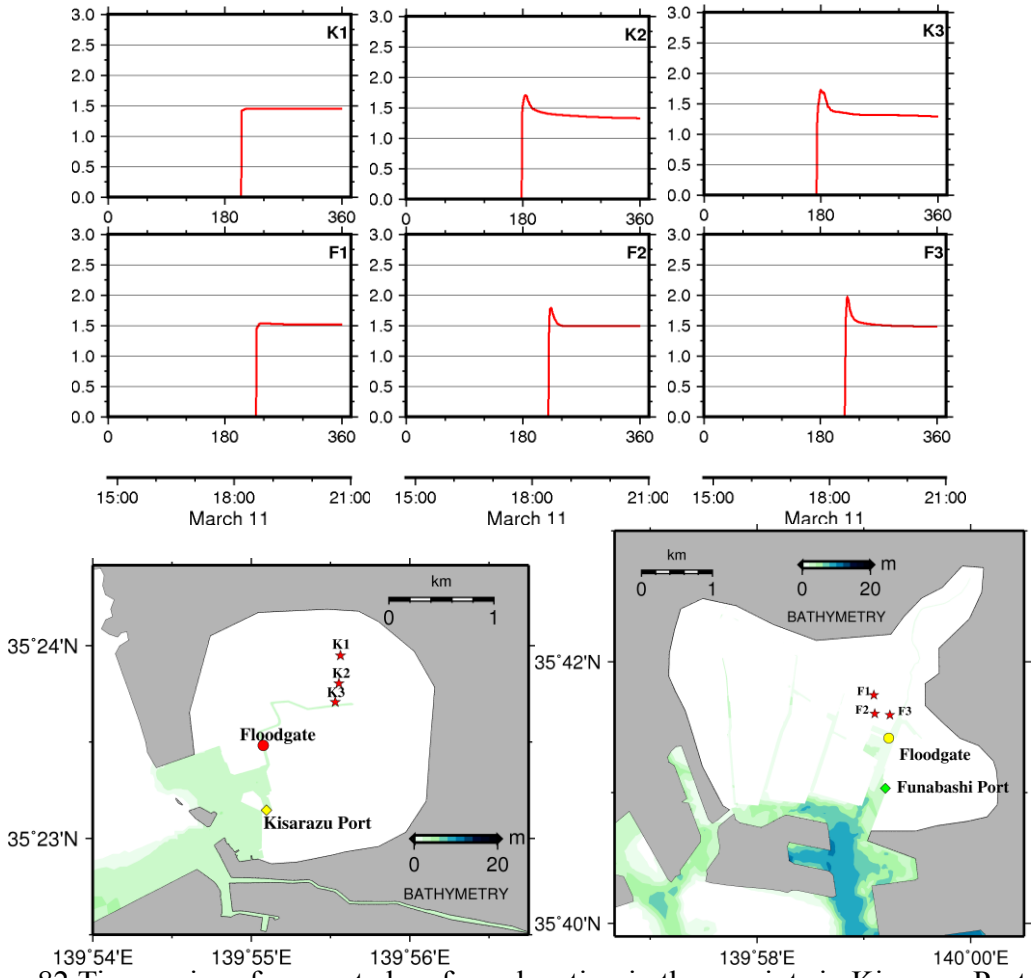

Figure 82 Time series of computed surface elevation in three points in Kisarazu Port (K1, K2, and K3) and Funabashi Port (F1, F2, and F3) when the floodgate is opened.

The inundation height varied with the distance from the nearest river . The further the distance, the lower the inundation height occurred. For the point located 137 m from the closest river, the inundation height in Funabashi Port reached 1.97 m while in Kisarazu Port for the point located 26 m from the closest river, the inundation height reached 1.72 m.

5.2.6. Sub Chapter Conclusions

FVCOM 2.6.1 was utilized to simulate the 2011 Tohoku Tsunami inundation to explain the effectiveness of floodgates in Funabashi Port and Kisarazu Port. The effectiveness of floodgates in preventing inundation was clear. The surrounding area was safe from inundation when the floodgates were closed while the surrounding area could be

inundated 620 m from the river in Funabashi Port and 450 m from the river in Kisarazu Port when floodgates failed to close. Based on the simulations, inundation height reached 1.97 m and 1.72 m above sea water level in Funabashi Port and Kisarazu Port, respectively.

Large inundation heights were observed in Funabashi Port and Kisarazu Port during the 2011 Tohoku Tsunami. Large inundation height was more accurately modeled in this study using 50-m resolution bathymetry data than the results of Wiyono and Sasaki (2012), who utilized 500-m resolution bathymetry data. In Kisarazu Port, although the tsunami trough was simulated quite well but discrepancies still exist. The discrepancies may due to missing detailed bathymetry data of ports.

5.3. Effect of tsunami countermeasures focusing on the tsunami arrival time in Kamakura

5.3.1. Introduction

As part of a tsunami warning system, tsunami hazard maps have essential roles in effective evacuation to show expected inundation areas and depth. Hazard maps are not only useful for residents to consider how to evacuate, but also for administrative bodies to consider countermeasures, including construction of disaster prevention facilities (Cabinet Office, 2004). However, most of the tsunami hazard maps do not show the minimum tsunami arrival time. Its potential misleading effect on the residents' decisions is one of probable reasons for excluding the information about the minimum arrival time (Cabinet Office, 2004).

Although it is necessary to be careful of a potential risk of misleading residents' decisions, once tsunami arrival is introduced, residents can estimate their limited evacuation time and their evacuation strategies can also be considered. Local governments can also decide which area should be prioritized during evacuation using this information. Imamura (2009) also stated that not only the data for time elapse for inundation can be obtained, but also the effectiveness of countermeasures can be evaluated by using tsunami arrival time map.

Yuigahama Coast, a concave bay located in Kamakura City, Kanagawa, Japan, has experienced damages caused by previous tsunamis. A main road connecting the coastal road and the downtown area and one of the major residential areas are located close to

Namerigawa River. A hazard map for tsunami arrival time seems to be highly important to estimate evacuation time in this area. However, Kamakura City government and Kanagawa Prefectural government do not show a map for arrival time in the expected inundation area except along the coastline. Thus, the objectives of the present study are to introduce a concept for an integrated tsunami minimum arrival time considering all the expected tsunamis and to study effective measures for increasing the least evacuation time.

5.3.2. Simulation setup

Application of an unstructured mesh model is an effective way to analyze the phenomena since the spatial scale of Kamakura area is much smaller than that of major tsunami propagation areas. In order to simulate tsunamis, an unstructured grid Finite Volume Coastal Ocean Model 2.6.1 is utilized. The mesh size varies from 5 m in inundation areas in Kamakura, 1 km in tsunami source areas, and 50 km in the ocean (Figure 83).

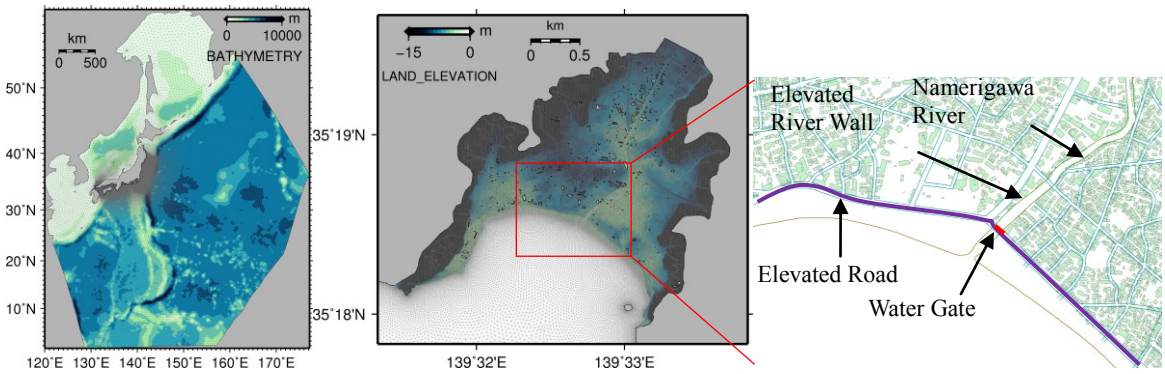

Figure 83 Mesh system of: a) Whole domain, b) Kamakura area, c) Countermeasures in Kamakura.

Propagation area mesh system consists of 667,834 nodes and 1,290,815 triangular elements while inundation area mesh system consists of 886,122 nodes and 1,720,490 elements. The mesh for tsunami propagation area was constructed using Surface-water Modeling System 10.1 (Aquaveo), covering from 120° to 177.2° E in longitude and from 1.4° to 59.7° N in latitude.

Ground heights in 5-m resolution, provided by Geospatial Information Authority of Japan (GSI), Ministry of Land, Infrastructure, Transport and Tourism, were interpolated over the expected inundation area in Kamakura. GEBCO_08 bathymetric data with 30 s

resolutions was adopted for area around Japan while the bathymetric data provided by ETOPO with 10 minute resolution was adopted for other area inside domain.

A fault model of Okada (1985) is utilized to construct spatial variations in the initial surface elevation. A critical value of inundation depth should be determined to develop a map for the minimum arrival time. Considering that people and cars are likely to be swept away when the inundation depth exceeds 0.5 m, the value was chosen as a critical value for this study.

All expected major tsunamis hitting Kamakura are simulated including Meiou, Keichou, Genroku Kanto, Kannawa-Kouzu Matsuda, Minami Kanto, Kanagawa-ken Seibu, and Bousou Peninsula. A contour map for the minimum arrival time were prepared by integrating simulation results from those tsunamis. Four types of countermeasures considered to be effective in terms of the magnitude of tsunami arrival time, inundation area and inundation depth were investigated for each earthquake and tsunami.

Figure 83c shows countermeasures details in Kamakura. Case 1, a control without countermeasures, is utilized to assess the effectiveness of the cases with countermeasures. In this case, the present coastal road and 5.5-m high river wall were considered. Case 2 is elevating the coastal road by 1 m by building a dike-like structure to reduce inundation. Case 3 is installing a 5.5-m high water gate at the mouth of Namerigawa River to reduce inundation along the river. Case 4 is elevating a 5.5-m high river wall by 1 m to reduce tsunami overflow along the river wall.

The time step for the external gravity mode is 0.05 s. A wet and dry treatment method was utilized to compute inundation. The drag coefficient was determined from the logarithmic law of the wall posing the minimum value of 0.0025. Horizontal two-dimensional computations were performed on a MPI-parallel supercomputer HA8000 (Hitachi Ltd.) at the University of Tokyo and Kyushu University.

5.3.3. Map for integrated minimum time

A set of simulations were performed for case 1 (no countermeasure) adopting seven types of tsunami. At each mesh, the minimum time when inundation depth reaches the critical value of 0.5 m was decided and compared among the results of the seven types of tsunamis. After comparison, the smallest time among all types of tsunamis was then extracted to create a contour map for the extracted minimum time (Figure 84**).**

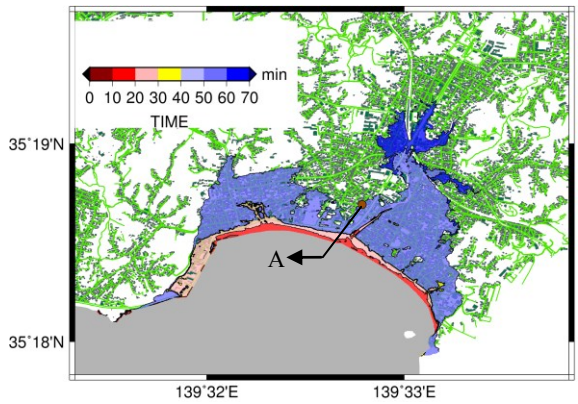

Figure 84 Map for the integrated minimum time for case 1 (control).

The minimum times between 50-60 minutes are due to Meiou and Keichou tsunamis while those less than 30 minutes are due to Genroku Kanto, Minami Kanto, and Kannawa-Kouzu Matsuda tsunamis. Tsunami flows generally reach the area in the bay sides later than the tip of the bay and the area along the river.

5.3.4. Map for the difference in the minimum time

Maps for the difference in the minimum time is shown by Figure 85**.** Area where the time difference is less than 0.5 min. is shown by yellow color.

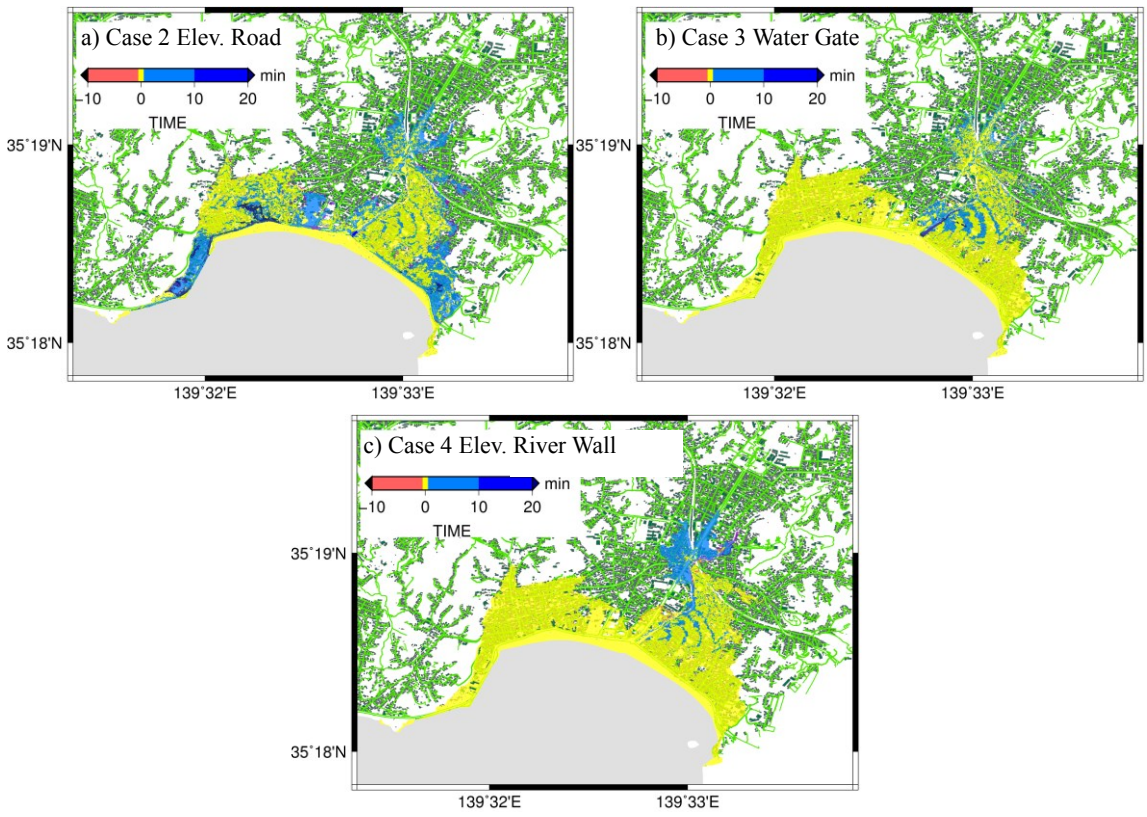

Figure 85 Maps for the difference in the minimum time: a) case 2, b) case 3, and c) case 4.

Pink or blue color shows the areas where the minimum time becomes shorter or longer after an application of a countermeasure, respectively. The difference in the minimum time t_{diff} between control case and one of the countermeasures' case is given by $t_{\mathrm{diff}} = t_{\mathrm{i}} - t_{\mathrm{1}}$ where t_{i} is the minimum time for one of the countermeasures' case and t_{1} is the minimum time for control case.

A map for the difference in the minimum time for the case 2 of the elevated road is shown by Figure 85a. Blue colored areas showing longer minimum time are observed around the elevated road. Blue colored areas are localized around the implemented places in case 3 (Figure 85b) and case 4 (Figure 85c). Almost no pink-colored areas showing shorter minimum time are seen except the places at the edges of the inundation area where wave reflection causes inundations in the neighboring areas.

The area with the minimum time being extended increases by 13.1%, 4.8%, and 4.3% for cases 2, 3 and 4, respectively, after applications of countermeasures. The lowest reduction in the inundation area is achieved by case 4 (elevated river wall), followed by case 3 (water gate) and then case 2 (elevated road). The elevated road can reduce the inundation area more than the other two countermeasures may be due to the ability of the elevated road to block more volume of water than the other two cases.

5.3.5. Map for integrated maximum velocity

A map for an integrated maximum velocity for case 1 (no countermeasure) extracting the maximum velocity at each mesh from the seven types of tsunamis is shown by Figure 86. Smaller velocities are shown in the northern inundation area while larger velocities are observed in coastline area and the downstream area of Namerigawa River. The area with higher ground elevation corresponds to the smaller velocity area.

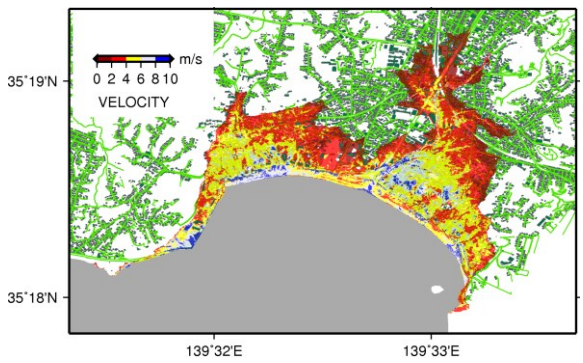

Figure 86 Map for integrated maximum velocity for case 1 (control).

5.3.6. Map for the difference in maximum velocity

Maps for the difference in the maximum velocity are shown by Figure 87**.** The difference in the maximum velocity v_{diff} between a case with one of the countermeasures and the control given by: $v_{\mathrm{diff}} = v_{\mathrm{i}} - v_{\mathrm{1}}$ where v_{i} is the maximum velocity for a case with one of the countermeasures and v_{1} is the maximum velocity for case 1 without countermeasures. Pink or blue color shows areas where the maximum velocity becomes smaller or larger after application of a countermeasure, respectively. Area where the difference in the maximum velocity is smaller than 0.5 m/s is represented by yellow color.

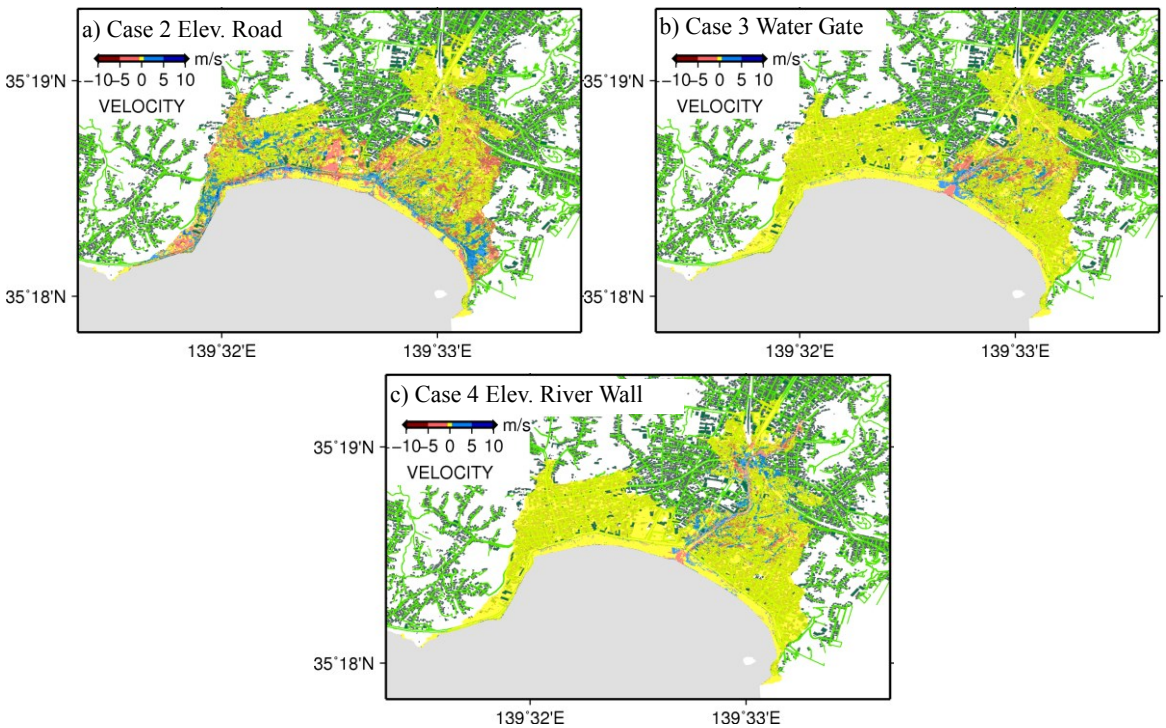

Figure 87 Maps for the difference in the maximum velocity: a) case 2, b) case 3,and c) case 4.

A map for the difference in the maximum velocity for case 2 with the elevated road is shown by Figure 87a. Maximum velocities are reduced along the elevated road. A map for the difference in the maximum velocity for case 3 with the water gate is shown by Figure 87b. Maximum velocities are found to decrease around the river mouth and up to approximately 650 m from the mouth. A map for the difference in the maximum velocity for case 4 with the elevated river wall is shown by Figure 87c. Maximum velocities reduced along the river. After applications of countermeasures, area with reduction in the maximum

velocities increase by 23.2%, 19%, and 18.6% of the inundation area for cases 2, 3 and 4, respectively.

Blue colored-area showing the areas where the maximum velocities become larger after applications of measures are shown around the location of countermeasures. In some areas the maximum velocities expand because of an increase in the ground level due to implementation of the countermeasures.

These results show that the difference in the maximum velocities are clearly observed around each of the measures. In particular, case 2 (elevated road) is recognized to be most effective in increasing the area with reduction in the maximum velocities.

5.3.7. Inundation depth and flow velocity at point A

The results in the previous sub chapter indicated that case 2 is the most effective countermeasure leading to the highest percentage of the area where the minimum time increases and the maximum velocity decreases. Time series of inundation depth and velocity at point A (see Figure 84) for case 1 (no countermeasures) and case 2 (elevated road) are shown in Figure 88. After elevating the road, the inundation depth and velocity decrease by 0.37 m in Meiou tsunami (Figure 88a) and by 0.65 m/s in Keichou tsunami (Figure 88b), respectively. The velocity, however, increases by 0.21 m/s in Meiou tsunami, probably because of the wave reflection around the south side of point A.

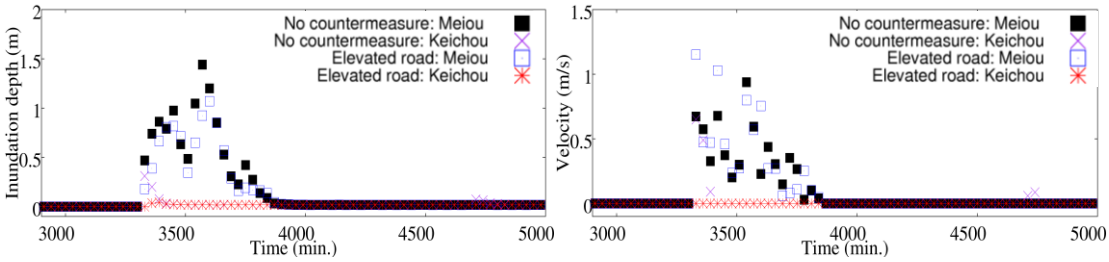

Figure 88 Time series of inundation depth and velocity at point A

5.3.8. Sub Chapter Conclusions

A concept of an integrated minimum time was introduced. The "minimum time" means the least time when the inundation depth firstly reaches some threshold value amongst all the expected tsunami simulation cases at each location. This concept was applied to the coastal area of Kamakura, Kanagawa, Japan, using FVCOM, and maps for the integrated minimum time were created supposing the threshold value of the inundation depth to be 0.5

m and considering seven expected earthquake and tsunamis (Meiou, Keichou, Genroku Kanto, Kannawa-Kouzu Matsuda, Minami Kanto, Kanagawa-ken Seibu, and Bousou Peninsula).

Using this concept, the effectiveness of countermeasures was considered in order to maximize expected minimum evacuation time, including the implementation of elevated road, water gate in a river mouth, and elevated river wall. Among these countermeasures, the elevated road case was the most effective for maximizing the expected minimum evacuation time and reducing the inundation area as well as lowering the maximum velocities. The effects of water gate and elevated river wall are localized to the area around the location of the implementations while the elevated road is more influential due to its large magnitude of the scale.

5.4. Tsunami inundation modeling in Yokohama

5.4.1. Introduction

Kanagawa Prefecture and Yokohama City government show tsunami hazard map in Yokohama without consideration of buildings. It is crucial to improve the hazard map, since existence of buildings on simulations may affect difference results in inundation area.

Tsunami inundation modeling with resolving buildings are necessary to be conducted. However, tsunami modeling with resolving building method may cause high computational cost while high computational cost may affect inability in performing simulations. In order to perform inundation modeling with acceptable results and efficient computational cost, new approach of spatial variation of bottom friction considering the fine structure of land use in unstructured grid model is proposed in this study.

This study aims to apply the proposed method to Keichou tsunami inundation simulation in Yokohama. In addition, difference results from different friction function calculation method are discussed.

5.4.2. Simulation set up

Unstructured-grid mesh system covering the tsunami propagation area from east longitude 120.5 to 161.73 degrees and north latitude of 12.72 to 39.94 degrees are constructed using SMS 10.1. Coastline dataset from NOAA was utilized for whole domain

except Tokyo Bay. In Tokyo Bay, coastline data from the National Land Numerical Information (MLIT) with higher resolution was utilized.

Bathymetry data, having a 10-minute resolution and provided by ETOPO, was utilized for the whole domain except for the area around Japan. GEBCO_08 bathymetry data with 30-s resolution was used for the area around Japan, while 50-m resolution data provided by Chiba Port Bureau of MLIT was adopted for Tokyo Bay area.

The mesh size varied from 100 m inside Tokyo Bay to 1 km in the tsunami source area, and 50 km in the ocean. Yokohama port was finely resolved with a 5-m mesh. Mesh system with 5-m resolution was also constructed for expected inundation area in Yokohama. Digital Elevation Model data with 5-m resolution was used for the inundation area.

Three numerical simulations are conducted for this study. Closed boundary condition is utilized for all simulations. Simulation setup of those simulations are shown in Table 12.

Table 12 Simulation setup of tsunami inundation modeling in Yokohama

No	Mesh Type	Elements	Nodes	BF condition	External time step
1	Resolved	1,569,132	817,181	Original	0.05 s
2	Unresolved	1,595,843	815,814	Original	0.05 s
3	Unresolved	1,595,843	815,814	Modified	0.05 s

For three mesh types, same propagation mesh system is utilized. The propagation mesh system is shown in Figure 89.

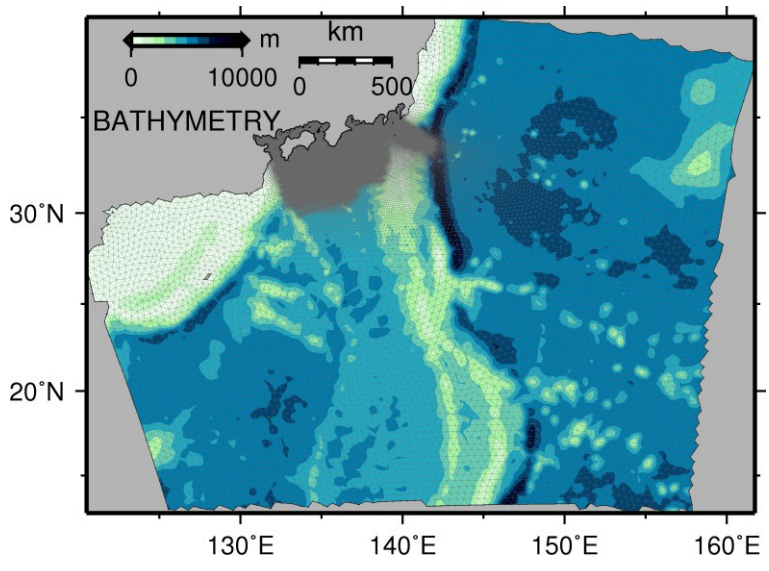

Figure 89 Propagation mesh system

While same propagation mesh system is utilized, different inundation mesh systems are utilized for each mesh type. Resolved and unresolved mesh system are shown in Figure 90a and Figure 90b, respectively.

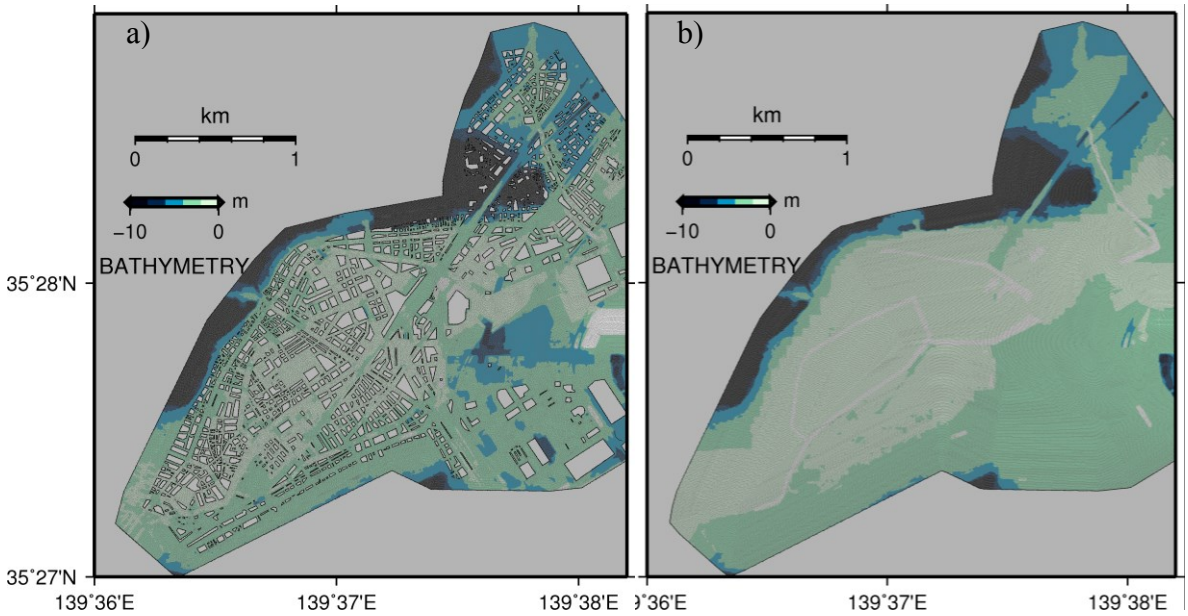

Figure 90 (a) Resolved mesh system and (b) Unresolved mesh system

In the following sub chapter, several results are shown in the right hand side of inundation area. The topography data and land use data of the focusing area are shown in Figure 91.

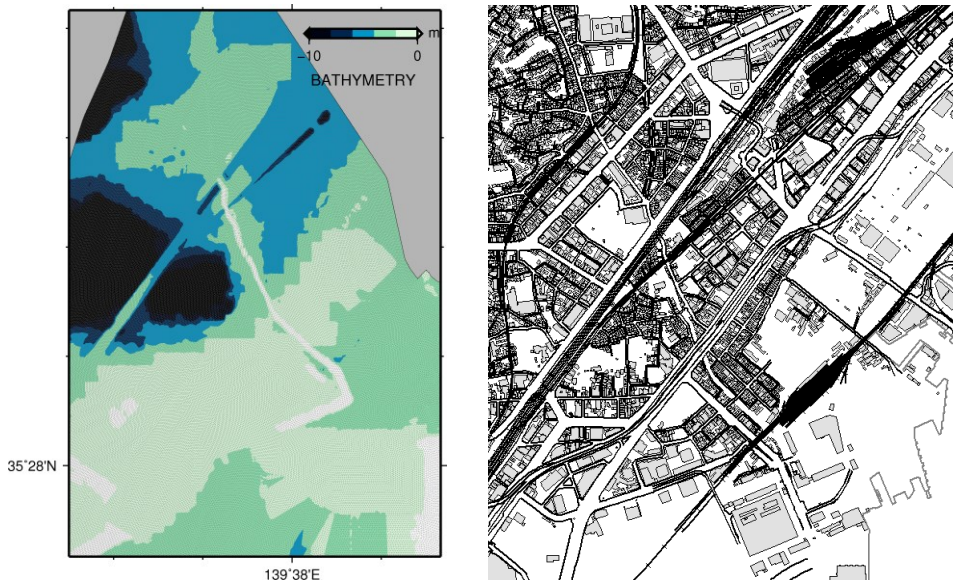

Figure 91 Topography (left) and land use (right) data of the focusing area

5.4.3. Spatial variation of surface elevations

In this sub chapter spatial variations of surface elevations for case 1 (resolved mesh with original bottom friction), case 2 (unresolved mesh with original bottom friction) and case 3 (unresolved mesh with modified bottom friction) are shown.

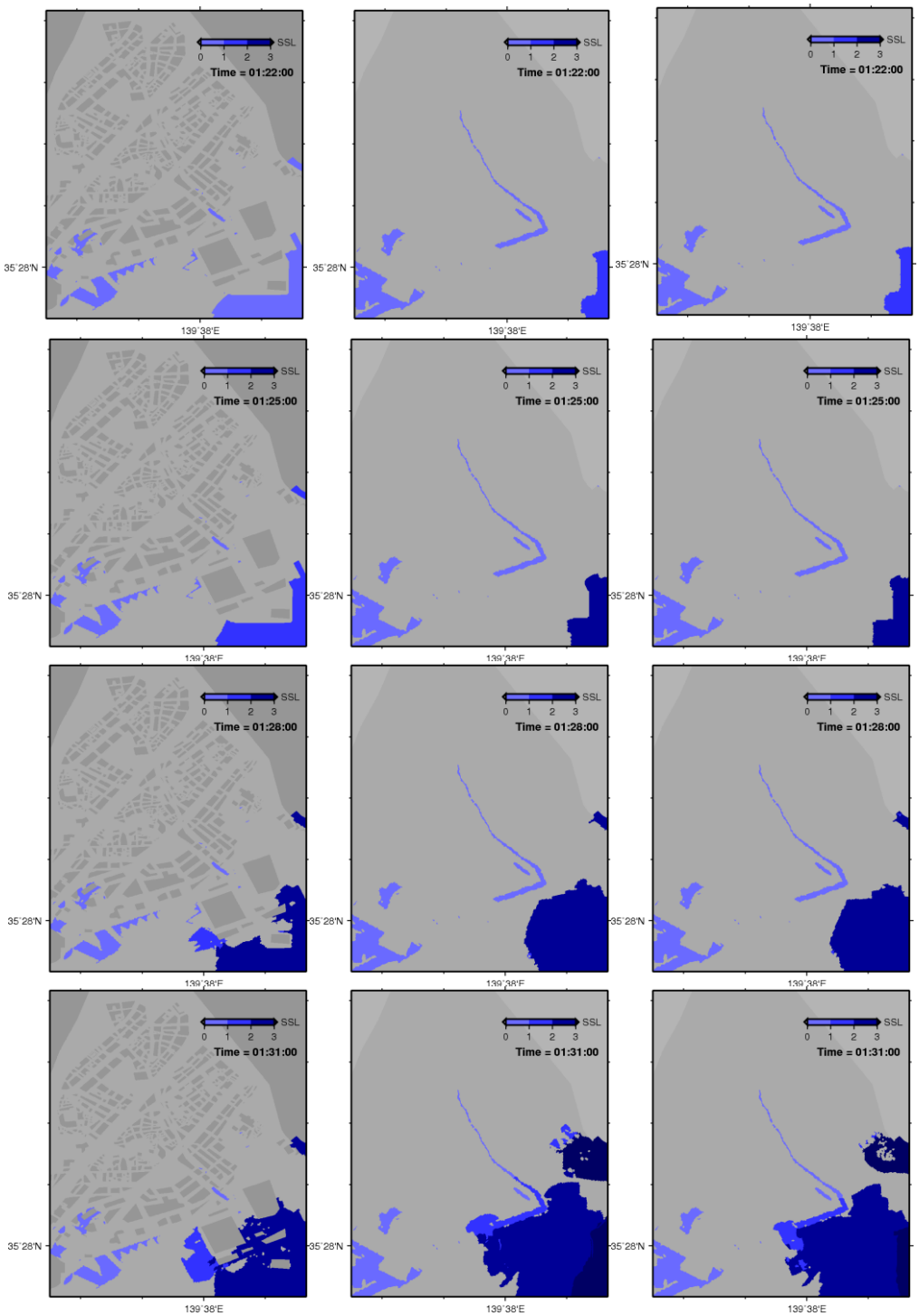

Figure 92 Spatial surface elevations for case 1 (left), case 2 (middle), and case 3 (right) at 01:22 until 01:31.

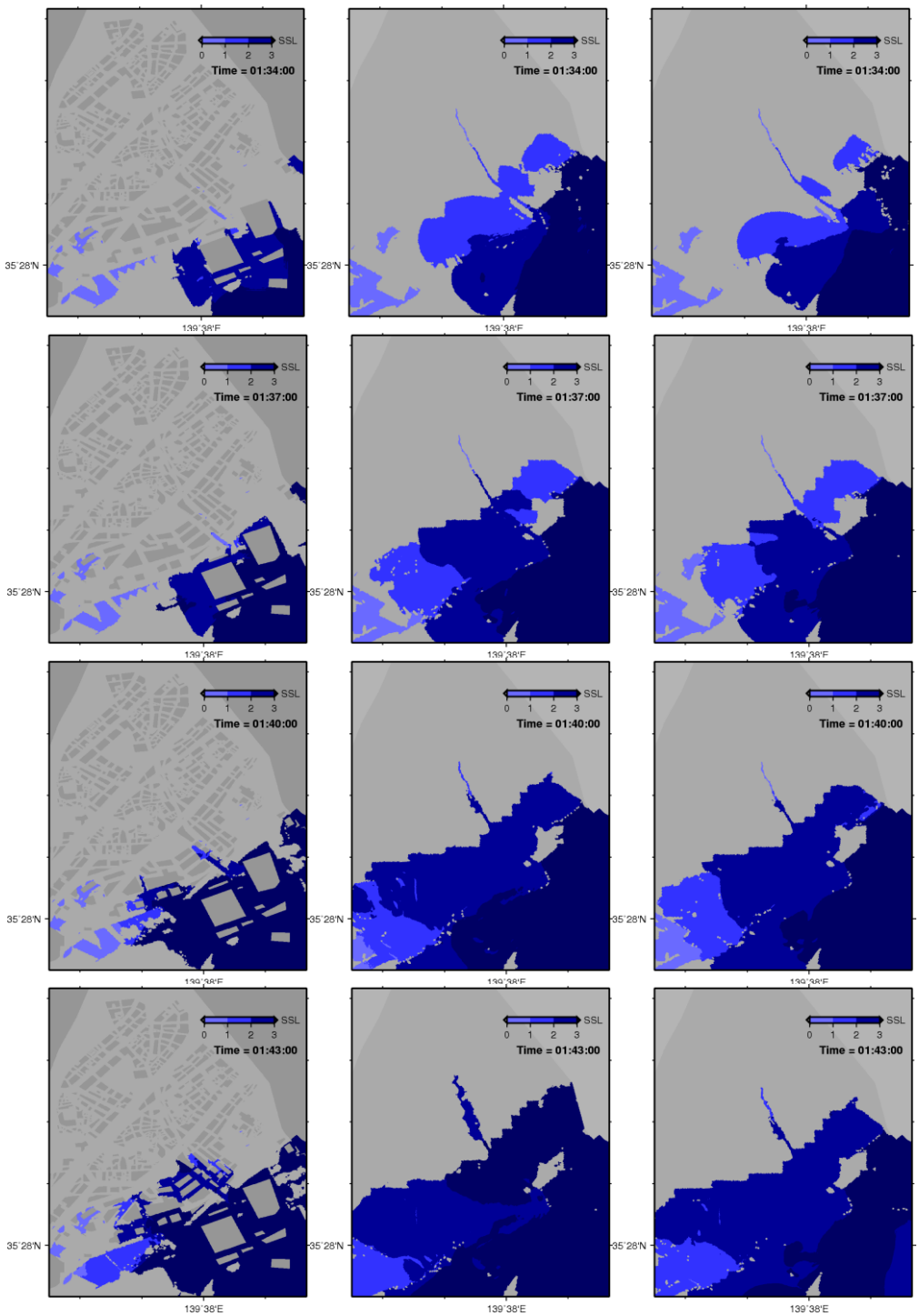

Figure 93 Spatial surface elevations for case 1 (left), case 2 (middle), and case 3 (right) at 01:34 until 01:43.

Buildings are resolved by case 1 while buildings are not resolved by case 2 and 3. Case 1 is considered as idealized case with all buildings are resolved and building heights are included. Case 2 is considered as the typical method to simulate tsunami in inundation area. Buildings are not resolved and building heights are not included because it is usually not available. Original bottom friction is utilized by case 2. Case 3 is considered as a method to

simulate tsunami in inundation area when the building heights data are not available. Buildings are not resolved and building heights are not included, however modified bottom friction is utilized to replace the existence of buildings.

Case 2 and case 3 show nearly similar speed of initial wave while case 1 shows slower wave speed (e.g. Figure 92 at 01:22 and 01:28). This behavior may be caused by the difference of mesh and topography. Figure 92 show the importance of utilizing the high resolution of topography data and mesh system in the focusing area.

Figure 93 also show the similar pattern with the previous figure. Case 1 show slower wave speed compared to those by case 2 and case 3. However, case 3 (modified bottom friction case) simulated slightly faster wave than case 2 e.g. Figure 93 at 01:34. The different speed of wave caused by the bottom friction difference among cases. Although both cases were utilizing the same initial surface elevation, mesh and topography; however, the bottom friction differences affected the difference in wave speed.

Case 2 used the original bottom friction from FVCOM with the law of the wall, posing 0.0025 as the minimum friction value while case 3 used the modified bottom friction with equation of Imai et al. (2013). Observing that the result of case 1 is considered as idealized case, the results of case 3 are closer to the results of case 1 because case 3 simulated slower wave than that of simulated by case 2. Wave speed by case 3 is low because the modified bottom friction succeeded to keep the speed of wave slower when the wave flows on the constructed area although the mesh is not resolved. The wave speed is higher by case 2 because the bottom friction is not modified and therefore the wave flow over building area without delayed by the effect of buildings.

5.4.4. Spatial variations of maximum inundation depth

Figure 94 shows maximum inundation depth of three cases. Case 1 is the idealized case where the buildings are resolved by cutting the triangular mesh and therefore the wave does not flow over the building area. In contrast, case 2 and case 3 utilized unresolved mesh system. Thus, wave flow over the constructed area in case 2 and case 3 while wave only flow in streets around buildings in case 1. A step-like maximum surface elevation are observed in the middle part of focusing area, simulated by case 2 and case 3. The step-like surface elevation occurred due to the topography data which was modified manually.

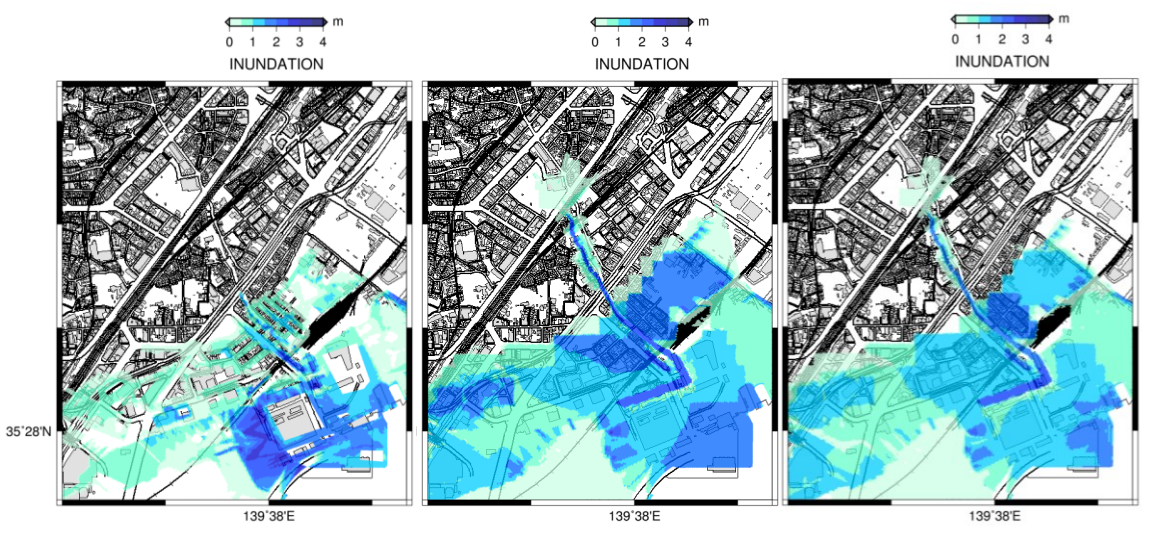

Figure 94 Spatial variation of maximum inundation depth for case 1 (left), case 2 (middle), and case 3 (right).

The topography data of case 2 and case 3 is developed from topography data of case 1 with removing the building data manually. Thus, the step-like surface elevations appeared. The process of topography data development has to be done smoothly and hence the step-like surface elevation will not arise.

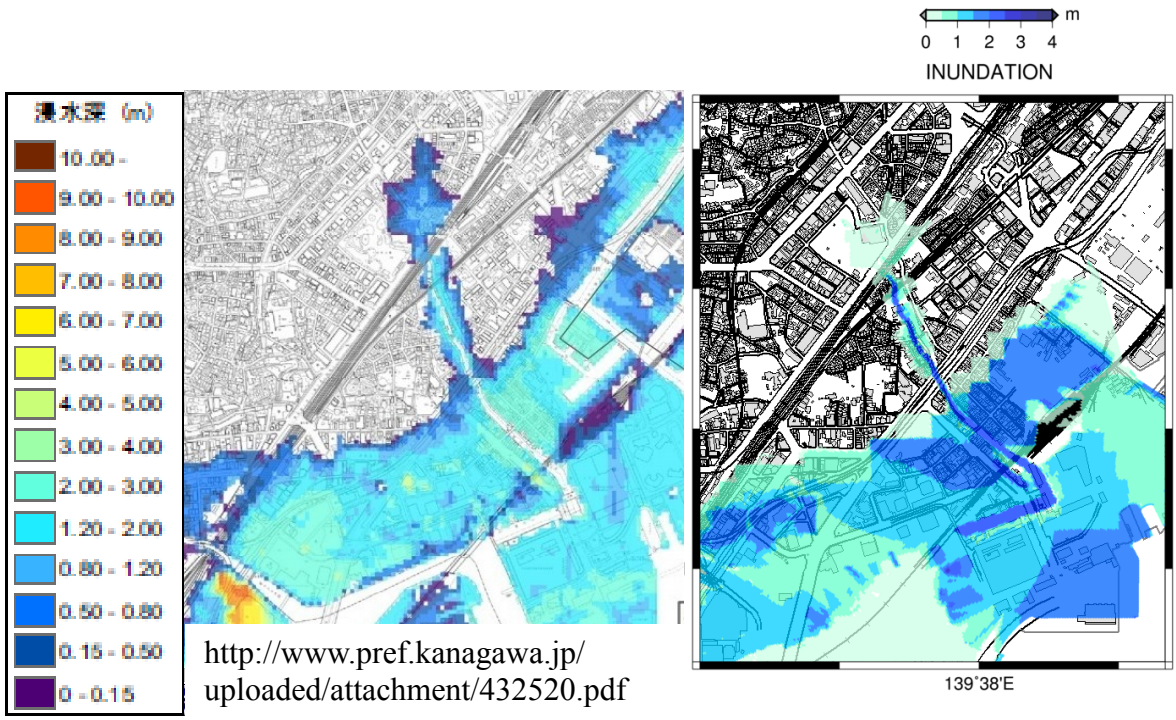

Figure 95 Comparison between hazard map from Kanagawa Prefecture (left) with maximum inundation depth for case 2 (right).

Mesh are not resolved by case 2 and case 3. The differences between both cases is that original bottom friction was utilized by case 2 but modified bottom friction was utilized by case 3. Because original bottom friction is used by case 2, the wave flow further than that of case 3. Modified bottom friction is simulated well by case 3 and hence the maximum inundation depth extent is less than the maximum inundation depth extent of case 2. Thus, the maximum inundation depth simulated by case 3 is closer to those simulated by the idealized case (case 1) than that of simulated by case 2.

Figure 95 shows comparison between hazard map from Kanagawa Prefecture and maximum inundation depth simulated by case 2 (unresolved mesh with original friction function). Inundation area shown in hazard map are generally similar to the maximum inundation depth simulated by case 2. There are slight differences between hazard map and simulated maximum inundation area. Case 2 slightly underestimated inundation area shown in hazard map in north and east-north side of the area. Underestimation may be caused by the difference in topography data used in this study.

5.4.5. Time series of inundation depth and velocity

In this sub chapter time series of inundation depth and velocity at two nodes are discussed. Location of two nodes at resolved mesh system is shown in Figure 96. Time series of inundation depth at point A and B are shown in Figure 97.

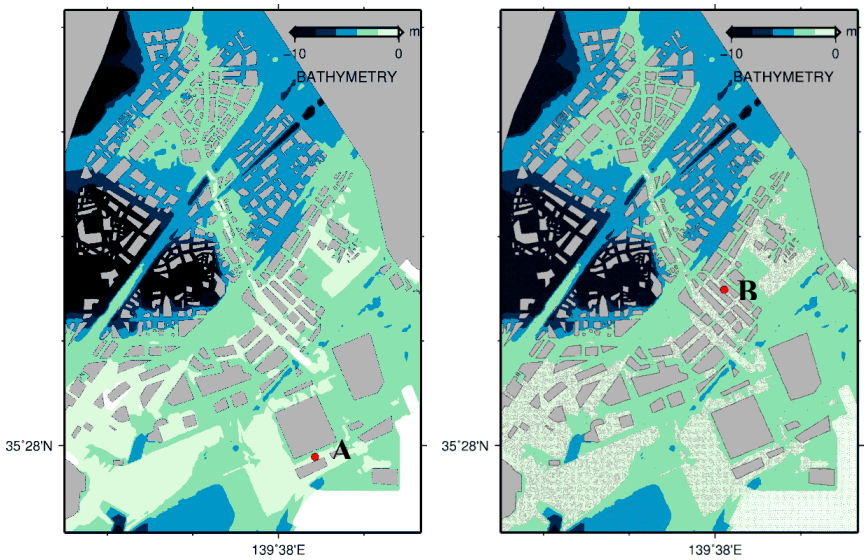

Figure 96 Location of point A and B at resolved mesh system.

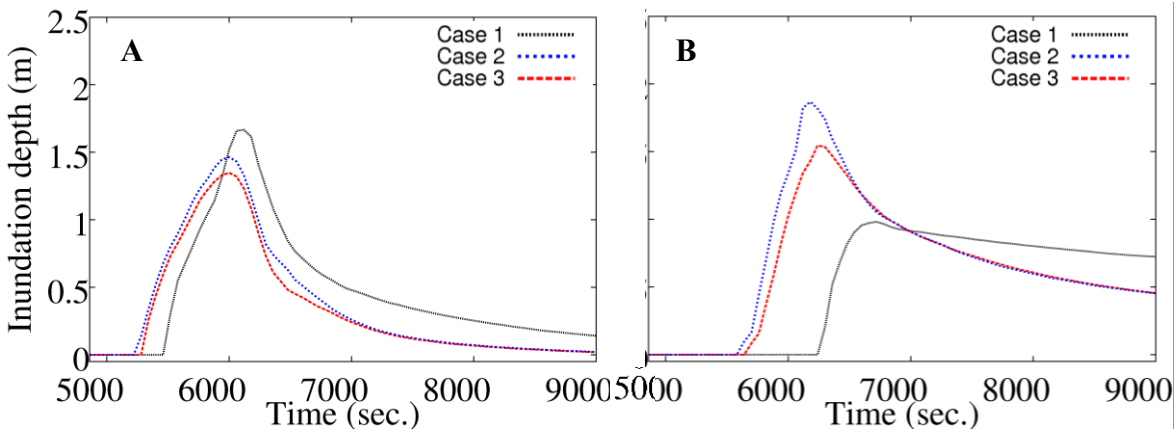

Figure 97 Time series of inundation depth at point A (left) and B (right).

Figure 97 shows general wave behavior simulated by case 2 (unresolved mesh with original friction function case) and case 3 (unresolved mesh with modified friction function case) at point A and B. Both cases utilized unresolved mesh system. No buildings are considered in the mesh system. The simulated results show how modification of friction function affects inundation depth on simulations. When original friction function is utilized, inundation depth values are high because no buildings are considered in that area. However, when modified friction function is utilized, inundation depth values are low because effects of buildings are simulated through friction function calculations. Hence, case 3 (modified friction function) simulated lower inundation depth than that of simulated by case 2 (original friction function).

Different behaviors are observed at point A and B when it is simulated by case 1 (resolved mesh case with original friction function). At point A, inundation depth simulated by case 1 is higher than those simulated by case 2 and case 3 while at point B, inundation depth simulated by case 1 is lower than those simulated by case 2 and case 3. Probable cause of this difference is that point A is located in coastline area while point B is located in the middle of inundation area. At point A, wave flows directly from offshore to point A without being stopped by buildings. However, wave has been stopped by existing buildings in surrounding area before reaching point B. Thus, inundation depth at point A is high while inundation depth at point B is low although they are simulated by the same case (case 1).

Figure 98 show time series of flow velocity at point A and B. Case 3 (unresolved mesh with modified friction function) simulated lower velocity than case 2 (unresolved mesh with original friction function) probably due to existence of friction function parameters in constructed area.

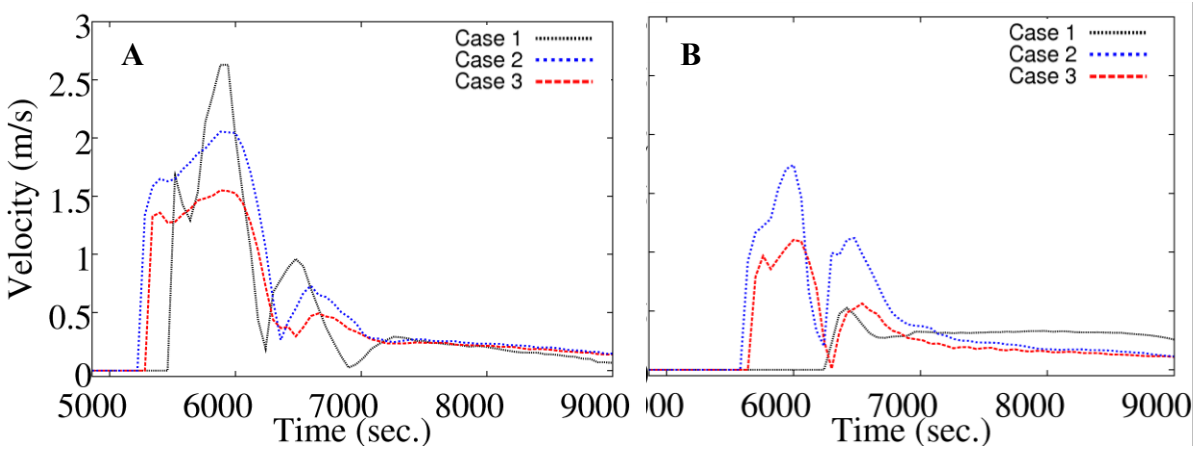

Figure 98 Time series of flow velocity at point A (left) and B (right).

Case 1 (resolved mesh case) show different velocity in the coastline area (point A) and middle of inundation area (point B). This behavior may due to existence of buildings in constructed area.

5.4.6. Comparison of maximum inundation area

In this sub chapter maximum inundation of whole inundation domain are compared. Firstly maximum inundation depth from Kanagawa Prefecture hazard map is shown in Figure 99.

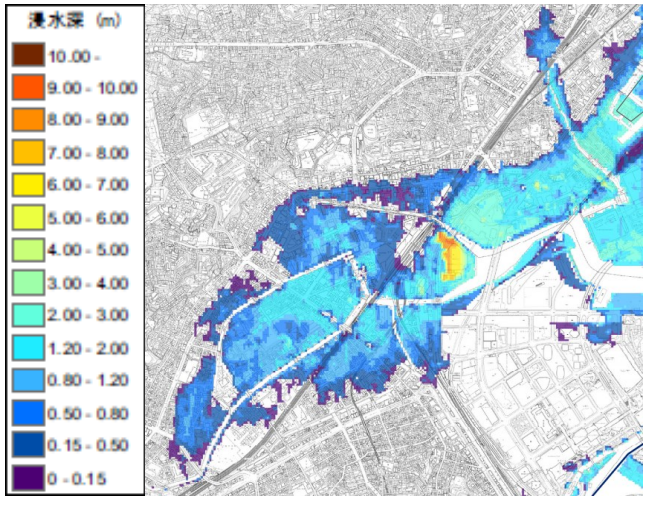

Figure 99 Maximum inundation depth from Kanagawa Prefecture hazard map (http://www.pref.kanagawa.jp/uploaded/attachment/432520.pdf).

Secondly, maximum inundation depth map simulated in this study are shown in Figure 100.

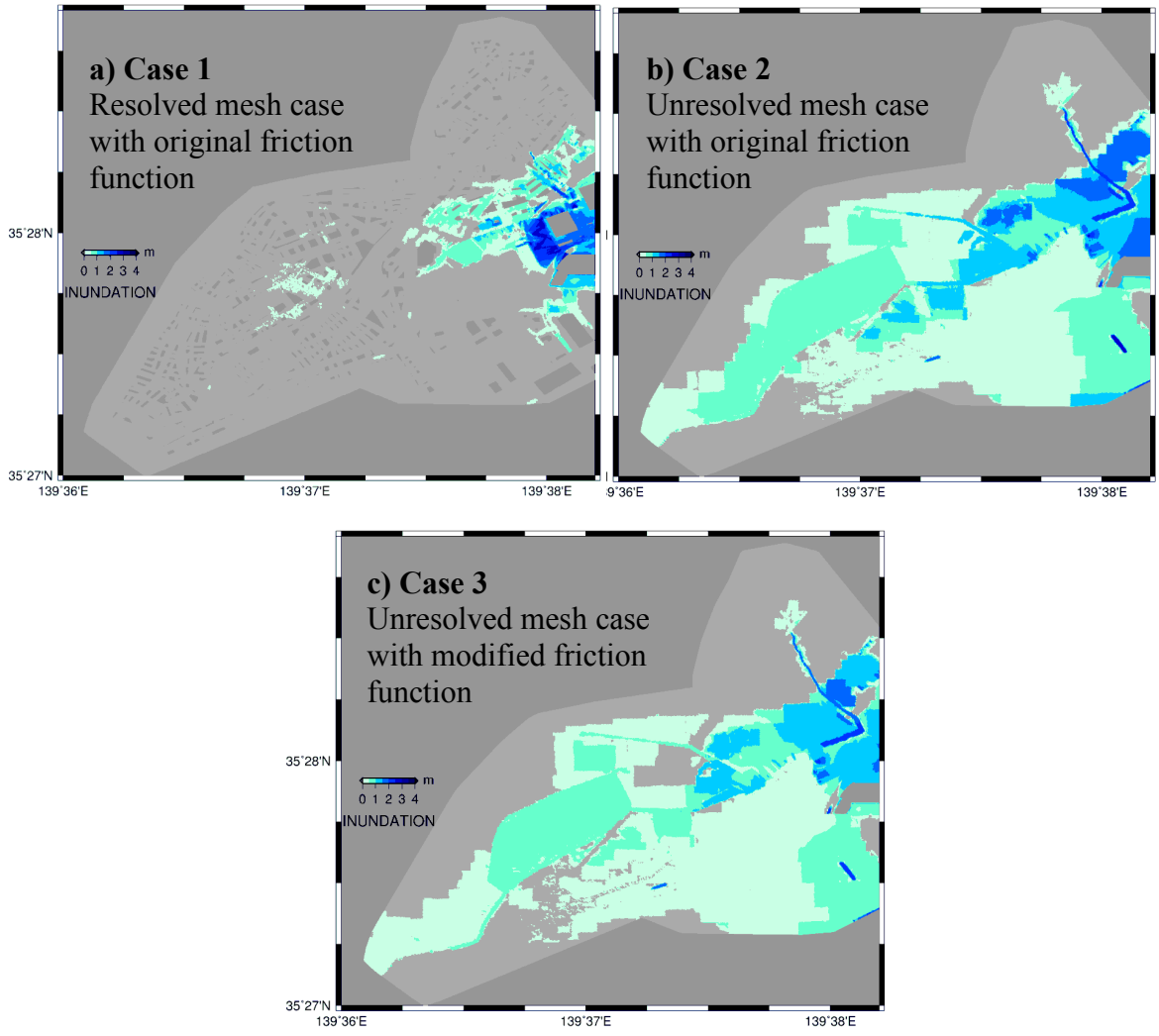

Figure 100 Maximum inundation depth of: a) case 1, b) case 2, and c) case 3.

Maximum inundation depth shown in Kanagawa Prefecture hazard map (Figure 99) shows quite similar pattern to maximum inundation depth simulated by case 2 (Figure 100b). Slight differences may be occurred due to differences in topography data utilized in this study. The results show the importance of topography data in determining simulated inundation depth.

Figure 100 shows maximum inundation area simulated by case 1 (resolved mesh with original friction function), case 2 (unresolved mesh with original friction function), and case 3 (unresolved mesh with modified friction function). It is shown that case 1 simulated the narrowest maximum inundation area while case 3 simulated wider inundation area and case 2 simulated the widest inundation area. Percentage values of maximum inundation area from total inundation area of each mesh system are tabulated in Table 13.

Table 13 Percentage of maximum inundation area from total inundation area of each mesh

Case	Mesh Type	BF condition	Inundation Area
1	Resolved	Original	14.8%
2	Unresolved	Original	64%
3	Unresolved	Modified	57.9%

Table 13 shows that maximum inundation area is simulated by case 2 (unresolved mesh with original friction function). Case 3 (unresolved mesh with modified friction function) shows smaller percentage of inundation area due to effect of modified friction function. The smallest percentage of inundation area is simulated by case 1 (resolved mesh case) due to existence of buildings in constructed area.

5.4.7. Sub Chapter Conclusions

Keicho Tsunami in Yokohama has been simulated using the proposed tsunami simulation system. Three simulations are conducted: resolved mesh case with original friction function, unresolved mesh case with original friction function, and unresolved mesh case with modified friction function.

Differences are observed between three simulations. Assuming case 1 as idealized case, the results of case 3 is closer to the results of case 1 because case 3 simulated slower wave than that of simulated by case 2. The wave speed simulated by case 3 is low because the modified bottom friction succeeded to keep the speed of wave lower when the wave flows on the constructed area although the mesh is not resolved. Using unresolved mesh system, case 2 simulated the faster wave because bottom friction is not modified, so the wave flow on constructed area with the same speed as the speed over non-constructed area.

Maximum inundation depth area are also different among simulations. Case 1 shows the smallest area of maximum inundation depth because buildings are resolved. Case 3 shows larger area of maximum inundation depth because buildings are not resolved and modified friction function is used while case 2 shows the largest area of maximum inundation depth because buildings are not resolved and original friction function is used. Considering case 1 as idealized case, the maximum inundation depth by case 3 is closer to the idealized case (case 1) than that of the maximum inundation depth by case 2.

6. CONCLUSIONS AND RECOMMENDATIONS

6.1. Conclusions

FVCOM has been validated with the analytical case: wave model under simplified beach model (Carrier and Greenspan 1958). The analytical solutions are reproduced by FVCOM simulation. Probable cause of the discrepancy is absence of velocity as boundary condition.

FVCOM has also been validated to experimental case: influence of macro-roughness on tsunami run up (Bridges 2011). FVCOM is able to reproduce the physical experiment results in offshore wave gauges and run up wave gauges well. Small wave reflections are detected due to reflections from the wave damping.

Validation to experimental case has also been conducted to tsunami inundation modeling in constructed environments (Park et al., 2013). Three types of simulation cases were carried out: resolved mesh case, concrete-resolved mesh case, and unresolved mesh case simulations.

Resolved mesh case results reproduced the experimental data well. Although there are underestimation in several wave gauges, general trends of experimental results are reproduced well by resolved mesh case results. The results show FVCOM was able to reproduce the experimental results well.

Spatial variation of surface elevation, maximum surface elevation and maximum velocity of concrete-resolved mesh case results are compared to resolved mesh case results. Although there are local discrepancies, general magnitudes of resolved mesh case results (which is considered as idealized case results) are reproduced well by concrete-resolved mesh case results. The proposed model reproduced maximum surface elevation well including high surface elevations caused by wave reflection because large hotels on the water front are resolved. Unresolved mesh case results could not reproduce the wave reflection because all buildings are not resolved.

Comparison of inundation depth at wave gauges are shown. Although discrepancies are observed, general tendencies of inundation depth of the proposed model followed the experimental results.

Comparison of cross shore velocity at wave gauges are also observed. Cross shore velocity of the experimental results are underestimated by the proposed model. This behavior

may be occurred due to absence of velocity as boundary condition and lack of resolved buildings around the wave gauges.

Numerical test of grid sizes are conducted. Among concrete-resolved mesh case results, grid size 0.4 m underestimated the experimental results more than simulation results with smaller grid sizes.

Numerical sensitivity test of friction factors show that there are slight differences between C=0.001 and C=0.005. Simulations with lower friction factor shows higher inundation depth than simulations with higher friction factor.

In this study, optimum grid size is considered as 0.3 m which is two times of the typical house size in the experiment. The reasons are as follow: (a) NRMSE value of the proposed grid size is less than 10% which meets the standard accuracy for inundation models with respect to laboratory data; (b) The proposed grid size reproduced maximum inundation depth at line B better than those of reproduced by larger grid size; (c) Number of nodes and elements used in the proposed simulation is 3.3 times smaller than those necessary for the idealized case simulation; (d) The proposed simulation system is 61.5% faster than the idealized simulation. Considering that the proposed method aims to be applied to real case with much larger number of nodes and elements, application of the proposed method is a promising method to reduce computational cost and reproduce the acceptable tsunami inundation results.

FVCOM has also been applied to the 2011 Tohoku Tsunami case to elucidate the mechanism of the 2011 Tohoku Tsunami properties in ports in Tokyo Bay including the mechanism responsible for the unexpectedly high amplification of the tsunami that was observed in some ports. The effectiveness of floodgates in preventing inundation was shown. The importance of bathymetry data resolution can be clarified from the simulations.

A concept of an integrated minimum time was introduced in this study. This concept was applied to the coastal area of Kamakura, Kanagawa, Japan, using FVCOM, and maps for the integrated minimum time were created supposing the threshold value of the inundation depth to be 0.5 m and considering seven expected earthquake and tsunamis (Meiou, Keichou, Genroku Kanto, Kannawa-Kouzu Matsuda, Minami Kanto, Kanagawa-ken Seibu, and Bousou Peninsula).

Using this concept, the effectiveness of countermeasures to maximize expected minimum evacuation time, including the implementation of elevated road, water gate in a river mouth, and elevated river wall were considered. Among these countermeasures, the

elevated road case was the most effective for maximizing the expected minimum evacuation time and reducing the inundation area as well as lowering the maximum velocities. The effects of water gate and elevated river wall are localized to the area around the location of the implementations while the elevated road is more influential due to its large magnitude of the scale.

Keicho Tsunami in Yokohama has been simulated using the proposed tsunami simulation system. Three simulations are conducted: resolved mesh case with original friction function, unresolved mesh case with original friction function, and unresolved mesh case with modified friction function. Maximum inundation depth area are compared among three simulations. Resolved mesh case shows the smallest area of maximum inundation depth because buildings are resolved. Unresolved mesh case with modified bottom friction shows larger area of maximum inundation depth because buildings are not resolved and modified friction function is used. Unresolved mesh case with original bottom friction shows the largest area of maximum inundation depth because buildings are not resolved and original friction function is used.

6.2. Recommendations

Below are recommendations for future study:

1. In the present study, boundary conditions that were used in numerical simulations are surface elevations. However, as it is shown in validations to analytical solutions and laboratory experimental results, it is necessary to include time series of velocity as boundary conditions in conducting numerical simulations because it may cause better reproducibility in term of wave phase.
2. In chapter 4.3.11, it is stated that different boundary conditions, in this case higher value of surface elevation may affect optimum grid size utilized in numerical simulations. Thus, it is necessary to conduct validations using higher surface elevations to check how optimum grid size is affected by difference in surface elevation values.
3. The proposed friction function method has been applied to Keicho Tsunami case in Yokohama. It is necessary to conduct further application to real cases including validations with existing tidal data and another observed data (e.g. inundation area).

REFERENCES

Aburaya, T. and Imamura, F. 2002. "The Proposal of a Tsunami Run-up Simulation using Combined Equivalent Roughness." Annual Journal of Coastal Engineering, JSCE 49: 276–280 (in Japanese).

Apotsos, A., Buckley, M., Gelfenbaum, G., Jaffe, B., and Vatvani, D. 2011. "Nearshore Tsunami Inundation Model Validation: Toward Sediment Transport Applications." Pure and Applied Geophysics 168 (11): 2097–2119.

Behrens, J., and LeVeque, R. 2011." Modeling and Simulating Tsunamis with an Eye to Hazard Mitigation. *SIAM News 44*(4): 1-8.

Behrens, Jörn. 2008. "Tsunawi Unstructured Mesh Finite Element Model for the Computation of Tsunami Scenarios with Inundation." NAFEMS Seminar: Simulation Komplexer Strömungsvorgänge (CFD): 1–10.

Bridges, KJ. 2011. "Influence of Macro-Roughness on Tsunami Runup & Forces." Master thesis, Ocean Engineering, School of Civil and Construction Engineering, Oregon State University.

Casulli, V. 1999. "A Semi-implicit Finite Difference Method for Non-hydrostatic, Free Surface Flows" International Journal for Numerical Methods in Fluids 30, 425-440.

Casulli, V, and Walters, R.A. 2000. "An Unstructured Grid , Three-Dimensional Model Based on the Shallow Water Equations", International Journal for Numerical Methods in Fluids 32. 331–48.

Chen, C., Beardsley, R.C., and Cowles, G. 2006. "An Unstructured Grid , Finite-Volume Coastal Ocean Model FVCOM User Manual Second Edition."

Chen, C., Beardsley, R.C., Cowles, G., Qi, J., Lai, Z., Gao, G., Stuebe, D., Liu, H., Xu, Q., Xue, P., Ge, J., Hu, S., Ji, R., Tian, R., Huang, H., Wu, L., Lin, H., Sun, Y., and Zhao, L. 2013. "An Unstructured Grid , Finite-Volume Community Ocean Model FVCOM User Manual Fourth Edition."

Chen, C., Lai, Z., Beardsley, R.C., Sasaki, J., Lin, J., Lin, H., Ji, R. and Sun, Y. 2014. "The March 11, 2011 Tohoku M9.0 Earthquake-induced tsunami and coastal inundation along the Japanese coast: A model assessment". Prog. Oceanogr., 123, 84-104,.

Cui, H. 2013." A New Numerical Model for Simulating the Propagation of and Inundation by Tsunami Waves." Ph.D thesis, Environmental Fluid Mechanics Section, Civil Engineering and Geoscience Faculty, Delft University of Technology.

Cui, H., Pietrzak, J.D., and Stelling, G.S. 2010. "A Finite Volume Analogue of the P1NC - P1 Finite Element: With Accurate Flooding and Drying." Ocean Modelling 35: 16-30.

De Brye, B., De Brauwere, A., Gourgue, O., Kärnä, T., Lambrechts, J., Comblen, R., and Deleersnijder, E. 2010. "A Finite-Element, Multi-Scale Model of the Scheldt Tributaries, River, Estuary and ROFI." Coastal Engineering 57: 850-863.

Deltares. 2014. "Delft3D-FLOW, Simulation of Multi-Dimensional Hydrodynamic Flows and Transport Phenomena, Including Sediments, User Manual.".

Dias, F., Dutykh, D., Brien, L. O', Renzi, E., and Stefanakis, T. 2014. "On the Modelling of Tsunami Generation and Tsunami Inundation." Procedia IUTAM 10: 338–355.

Dutykh, D., Poncet, R., and Dias, F. 2011. "The VOLNA Code for the Numerical Modeling of Tsunami Waves: Generation, Propagation and Inundation." European Journal of Mechanics - B/Fluids 30 (6): 598–615.

EDF-DRD. 2000. "Telemac Modelling System. Telemac-2D Validation Document."

Ford, R, Pain, C. C., Piggott, M. D., Goddard, A. J. H., De Olieveira, C. R. E., and Umpleby, A. P. 2004. "A Nonhydrostatic Finite-Element Model for Three-Dimensional Stratified Oceanic Flows. Part I: Model Formulation." Monthly Weather Review 132: 2816–2831.

Goto, C., and Shuto, N. 1983. "Effects of Large Obstacles on Tsunami Inundations." Tsunamis: Their Science and Engineering: 511-525.

Harig, S., Chaeroni, Pranowo, W. S., and Behrens, J. 2008. "Tsunami simulations on several scales." *Ocean Dynamics* 58: 429-440.

Ham, D. 2006. "On Techniques for Modelling Coastal and Ocean Flow with Unstructured Meshes." Ph.D thesis. Delft University of Technology.

Hervouet, JM. 2000. “TELEMAC Modelling System: An Overview.” Hydrological Processes 14: 2209–2210.

Kilinc, İ., Hayir, A., and Cigizoglu, H.K. 2009. “Wave Dispersion Study for Tsunami Propagation in the Sea of Marmara.” Coastal Engineering 56: 982–991.

Lehfeldt, R, Milbradt, P., Plüss, A., and Schüttrumpf. H. 2007. “Propagation of a Tsunami-Wave in the North Sea.” Die Kuste 72: 105-123.

MacInnes, B. T., Gusman, A. R., LeVeque, R. J., and Tanioka, Y. 2013. “Comparison of Earthquake Source Models for the 2011 Tohoku Event Using Tsunami Simulations and Near-Field Observations.” Bulletin of the Seismological Society of America 103 (2B): 1256–1274..

Macwilliams, M. L., Salcedo, F. G., and Gross, E. S. 2008. “San Francisco Bay-Delta UnTRIM Model Calibration Report.” California Department of Water Resources.

Mitchell, A. J., Uličný, D., Hampson, G. J., Allison, P. A., Gorman, G. J., Matthew, D. P., Wells, M. R., and Pain, C. C. 2010. “Modelling Tidal Current-Induced Bed Shear Stress and Palaeocirculation in an Epicontinental Seaway: The Bohemian Cretaceous Basin, Central Europe.” Sedimentology 57: 359–388.

Mori, N., Takahashi, T., and The 2011 Tohoku Earthquake Tsunami Joint Survey Group. 2012. “Nationwide Post Event Survey and Analysis of the 2011 Tohoku Earthquake Tsunami.” Coastal Engineering Journal 54 (01).

Muhari, A., Imamura, F., Koshimura, S., and Post, J. 2011. “Examination of Three Practical Run-up Models for Assessing Tsunami Impact on Highly Populated Areas.” Natural Hazards and Earth System Science 11: 3107–3123.

Myers, E. P, and Baptista, A. M. 2001. “Analysis of Factors Influencing Simulations of the 1993 Hokkaido Nansei-Oki and 1964 Alaska Tsunamis”, Natural Hazards 23: 1–28.

Okada, Y. 1985. “Surface Deformation due to Shear and Tensile Faults in a Half-Space” Bulletin of the Seismological Society of America 75 (4): 1135–1154.

Park, H., Cox, D. T., Lynett, P. J., Wiebe, D. M., and Shin, S. 2013. "Tsunami Inundation Modeling in Constructed Environments: A Physical and Numerical Comparison of Free-Surface Elevation, Velocity, and Momentum Flux." Coastal Engineering 79: 9-21.

Pedersen, N. H., Rasch, P. S., and Sato T. 2005. "Modelling of the Asian Tsunami off the Coast of Northern Sumatra" *Danish Hydraulic Institute Technical Paper*.

Priest, G. R., Goldfinger, C., Wang, K., Witter, R. C., Zhang, Y., & Baptista, A. M. 2010. "Confidence Levels for Tsunami-Inundation Limits in Northern Oregon Inferred from a 10,000-Year History of Great Earthquakes at the Cascadia Subduction Zone." Natural Hazards 54 (1): 27–73.

Rakowsky, N., Androsov, A. Fuchs, A., Harig, S., Immerz, A., Danilov, S., Hiller, W., and Schröter, J. 2013. "Operational Tsunami Modelling with TsunAWI – Recent Developments and Applications." Natural Hazards and Earth System Science 13 (6): 1629–42.

Rojali, A., Kusuma, S. B., and Harlan, D. 2012. "Finite Volume Numerical Modeling Application for Tsunami.", Master Thesis, Faculty of Civil and Environmental Engineering, Institut Teknologi Bandung (in Indonesian).

Sasaki, J., Komatsu, Y., Matsumaru, R., and Wiyono, R. U. A. 2011. "Unstructured Model Investigation of 2004 Indian Ocean Tsunami Inundation in Banda Aceh , Indonesia." *Journal of Coastal Research* SI64: 941–945.

Sasaki, J., Ito, K., Suzuki, T., Wiyono, R. U. A., Oda, Y., Takayama, Y., Yokota, K., Furuta, A., and Takagi, H. 2012. "Behavior of the 2011 Tohoku Earthquake Tsunami and Resultant Damage in Tokyo Bay." *Coastal Engineering Journal* 54 (01).

Sassi, M. G., Hoitink, A. J. F., de Brye, B., Vermeulen, B., and Deleersnijder, E. 2011. "Tidal Impact on the Division of River Discharge over Distributary Channels in the Mahakam Delta." *Ocean Dynamics* 61: 2211–2228.

Venturato, A. J., Arcas, D., and Kanoglu, U. 2007. "Modeling Tsunami Inundation from a Cascadia Subduction Zone Earthquake for Long Beach and Ocean Shores, Washington." NOAA Technical Memorandum OAR PMEL-137.

Wekerle, C, S Harig, W Pranowo, A Androsov, A Fuchs, N Rakowsky, S Danilov, and J Behrens. 2010. “Dependency of Tsunami Simulations on Advection Scheme , Grid Resolution , Bottom Friction and Topography”, in IMUM 2010, MIT, Boston.

Wiyono, R. U. A., Sasaki, J., and Suzuki, T. 2013. “Numerical Assessment of the 2011 Tohoku Earthquake Tsunami in Ports of Tokyo Bay with the Effectiveness of Floodgates”, *In: Proceedings 12th International Coastal Symposium* (Plymouth, England), *Journal of Coastal Research*, SI 65.

Zhang, Y. J., and Baptista, A. M. 2008. “An Efficient and Robust Tsunami Model on Unstructured Grids. Part I: Inundation Benchmarks.” *Pure and Applied Geophysics* 165: 2229–2248.

PUBLICATIONS

1. Wiyono, R.U.A. and Sasaki, Jun. Numerical Analysis of the 2011 Tohoku Tsunami in Tokyo Bay Focusing on High Water Marks in Ports. *The Twenty-second (2012) International Offshore and Polar Engineering Conference, Rhodes, Greece, June 17–22, 2012*
2. Wiyono, R.U.A., Sasaki, J. and Suzuki, T. Numerical Assessment of the 2011 Tohoku Earthquake Tsunami in Ports of Tokyo Bay with the Effectiveness of Floodgates. *In: Proceedings 12th International Coastal Symposium* (Plymouth, England), *Journal of Coastal Research*, Special Issue No. 65, 2013, pp. 844-849, ISSN 0749-0208.
3. Wiyono, R.U.A., Sasaki, J. and Suzuki, T. Effects of the tsunami countermeasures focusing on the tsunami arrival time in Kamakura. J. JSCE B2 (Coastal Eng.), 70(2), 5pp., 2014.
4. Sasaki, J., Komatsu, Y., Matsumaru, R., and Wiyono, R.U.A. Unstructured Model Investigation of 2004 Indian Ocean Tsunami Inundation in Banda Aceh, Indonesia. J. Coastal Res., SI64, 941-945, 2011.
5. Sasaki, J., Ito, K., Suzuki, T., Wiyono, R.U.A., Oda, Y., Takayama, Y., Yokota, K., Furuta, A., and Takagi, H. Behavior of the 2011 Tohoku Earthquake Tsunami and Resultant Damage in Tokyo Bay. Coastal Eng. J., 54(1), 1250012, 26pp., 2012.
6. 佐々木 淳・伊藤一教・鈴木崇之・Retno Utami Agung WIYONO・織田幸伸・高山百合子・羽角華奈子・古田敦史・高木泰士．2011 年東北津波の東京湾内での伝播特性と被害状況．土木学会論文集 B2，68(2)，I_261-I_265，2012
7. 佐々木 淳・椎野悟史・Retno Utami Agung Wiyono・鈴木崇之・田中陽二：鎌倉沿岸における津波到達時間に着目した減災方策の検討，日本沿岸域学会研究討論会講演概要集，26 巻，2pp., 2013.
8. 佐々木 淳・山本修司・Retno Utami Agung Wiyono・鈴木崇之・田中陽二：2011 年東北津波による東京湾のノリ養殖被害に関する考察，土木学会論文集 B2（海岸工学），69(2)，I_351-I_355，2013.
9. 山本修司・佐々木 淳・鈴木崇之・Retno Utami Agung Wiyono・田中陽二：東京湾における東日本大震災による水産業への影響，第 24 回海洋工学シンポジウム，6pp., 2014.